Lehrstuhl für Biomedizinische Physik
Technische Universität München

Quantitative phase-contrast computed tomography for biomedical applications

Marian S. Willner

Dissertation

January 2017

Supervisors:
Dr. med Alexander Fingerle
Prof. Dr. Franz Pfeiffer

Technische Universität München

Technische Universität München
Physik Department
Lehrstuhl für Biomedizinische Physik

Quantitative phase-contrast computed tomography for biomedical applications

Marian S. Willner

Vollständiger Abdruck der von der Fakultät für Physik der Technischen Universität München zur Erlangung des akademischen Grades eines

Doktors der Naturwissenschaften (Dr. rer. nat.)

genehmigten Dissertation.

Vorsitzender:	Univ.-Prof. Dr. M. Zacharias
Prüfer der Dissertation:	1. Univ.-Prof. Dr. F. Pfeiffer
	2. Univ.-Prof. Dr. J. J. Wilkens

Die Dissertation wurde am 08.11.2016 bei der Technischen Universität München eingereicht und durch die Fakultät für Physik am 30.11.2016 angenommen.

Abstract

X-ray phase-contrast computed tomography (CT) is an emerging imaging technique that provides enhanced soft-tissue contrast and complementary information compared to conventional attenuation-based X-ray imaging. In recent years, phase-contrast CT became increasingly popular for the three-dimensional (3D) investigation of biological samples at large-scale synchrotron radiation facilities. The impressing imaging results hold great promise that this novel approach opens up new opportunities in biomedical research and even clinical diagnostics. An important step towards a broad application of phase-contrast CT was the successful implementation of X-ray grating interferometry, which is one of the currently available phase-sensitive imaging methods, at standard polychromatic X-ray sources.

The ultimate goal of this thesis is to investigate and further develop the capabilities of phase-contrast CT utilizing a grating interferometer in commonplace research laboratories. The work includes the design and optimization of a lab-based phase-contrast imaging setup to achieve a soft-tissue contrast that is comparable to synchrotron radiation facilities. A framework is built for the extraction of quantitative tissue properties like linear attenuation coefficients, electron densities and Hounsfield units from the recorded 3D volume data in conventional attenuation contrast and phase contrast. Quantitative values are determined for various tissue types and the effect of formalin fixation on the results is examined. The gain of information due to the complementarity of both contrast modalities and the added value of a combined data analysis are explored. In this context, the possibility of an advanced tissue characterization in terms of protein, lipid, and water concentrations is demonstrated. Several biomedical studies are performed in close collaboration with clinical partners to evaluate phase-contrast CT as tool for the 3D examination of excised tissue samples and to identify potential diagnostic cases that might arise or benefit from an integration of the technique in medical devices.

Zusammenfassung

Die Phasenkontrast-Computertomographie (CT) mit Röntgenstrahlung ist eine neue bildgebende Technik, welche einen verbesserten Weichgewebekontrast im Vergleich zur rein schwächungsbasierten Röntgenbildgebung erzielt und zudem komplementäre Informationen liefert. In den vergangenen Jahren gewann die Phasenkontrast CT zunehmend an Bedeutung für die drei-dimensionale (3D) Untersuchung von biologischen Proben an Großforschungseinrichtungen mit Synchrotronstrahlung. Die beeindruckenden Bildergebnisse sind vielversprechend, dass diese neuartige Bildgebungsmodalität ungekannte Möglichkeiten im Bereich der biomedizinischen Forschung und sogar der klinischen Diagnostik ermöglichen könnte. Ein wichtiger Schritt hinsichtlich einer breiten Anwendung der Phasenkontrast CT war die erfolgreiche Implementierung der Gitterinterferometrie – eine der aktuell verfügbaren Phasen-sensitiven Bildgebungsmethoden – an herkömmlichen polychromatischen Röntgenröhren.
Ziel der vorliegenden Arbeit ist es, das Potential und die Chancen der Phasenkontrast CT mittels Gitterinterferometrie in gewöhnlicher Laborumgebung zu erforschen und weiterzuentwickeln. Dies beinhaltet die Konstruktion und Optimierung eines Laboraufbaus für die Phasenkontrastbildgebung, mit welchem ein zu Synchrotronanlagen vergleichbarer Weichgewebekontrast erreicht werden kann. Ein standardisiertes Verfahren wird erarbeitet, um aus den konventionellen, schwächungsbasierten sowie den mit Phasenkontrast aufgenommenen 3D Volumendaten unterschiedliche Gewebegrößen wie lineare Schwächungskoeffizienten, Elektronendichten oder Hounsfield-Einheiten zu extrahieren. Für verschiedenste Gewebearten werden quantitative Werte ermittelt. Zudem wird der Einfluss einer Formalinfixierung der Gewebeproben auf die Ergebnisse untersucht. Der zusätzliche Informationsgehalt aufgrund der Komplementarität beider Kontrastmechanismen und der Mehrwert einer kombinierten Datenanalyse werden erkundet. In diesem Zusammenhang wird demonstriert, dass eine erweiterte Charakterisierung hinsichtlich der Protein-, Lipid- und Wasserkonzentrationen von Gewebe möglich erscheint. Mehrere biomedizinische Studien werden in enger Zusammenarbeit mit klinischen Partnern durchgeführt, um die Phasenkontrast CT als Instrument für die 3D Untersuchung entnommener Gewebeproben zu evaluieren und potentielle diagnostische Fragestellungen zu identifizieren, welche von einer klinischen Umsetzung der Technik profitieren könnten.

Contents

Chapter 1

Introduction

In the year 1895, Wilhelm Röntgen discovered a novel electromagnetic radiation, which he simply called *X-Strahlung* for being of yet unknown type. Although the characteristics of this new kind of radiation and the interaction with matter have extensively been studied up to now, the name *X-rays* remained. The ability of X-rays to penetrate opaque matter gave rise to a broad range of applications. Besides their use in industry and research, X-rays are in particular utilized to depict inner structures of the human body in clinical diagnostics.
In conventional X-ray imaging, the object of interest is illuminated from one side and the transmitted intensity is recorded on the other side using photosensitive plates and later electronic detectors. Taking an X-ray radiograph, all the object's internal structures are projected onto one two-dimensional (2D) image and overlay with each other. Topological information of the object can be revealed by X-ray computed tomography (CT). Here, many images are taken from different directions and a three-dimensional (3D) representation of the object is reconstructed. The generation of contrast is related to the density and elemental composition of the materials within the specimen. High-density differences translate into pronounced changes of transmitted intensity. That is why bones, for example, can be very clearly distinguished from their surrounding tissue.
Despite the deposition of radiation dose, CT is the mostly used 3D imaging modality for medical diagnosis in daily routine. Advantages over magnetic resonance imaging (MRI) are its cost-effectiveness, fast acquisition times, and high spatial resolution. In addition, quantitative imaging can be performed in terms of Hounsfield units, which are numbers specially defined for CT imaging. Compared to MRI, the perceptibility of pathological changes within soft tissue is rather poor without the application of strongly absorbing contrast agents.
The low intrinsic soft-tissue contrast is the reason that conventional X-ray imaging is not a widely spread tool in biomedical research for the 3D investigation of tissue samples. However, phase-sensitive X-ray imaging techniques are increasingly utilized for this purpose at large-scale synchrotron radiation facilities. Phase contrast, as opposed to attenuation contrast (used in standard X-ray images),

exploits a complementary interaction process of X-rays with matter. Image formation is based on the phase shift that X-rays as electromagnetic waves undergo when passing through the object. The fundamentally different interaction mechanism measured by the phase shift yields high potential to enhance soft-tissue contrast and can provide complementary information to attenuation contrast.
Because only the intensity and not the phase of X-rays can be directly recorded by imaging detectors, phase-sensitive techniques need to transfer the shift in phase that occurs into a change of intensity. Existing methods, therefore, rely on the generation and measurement of interference effects like phase-shift induced refraction angles. In most cases, this requires X-ray beams of high spatial and temporal coherence, available only at synchrotrons. In general, there are crystal-interferometer-based, propagation-based, crystal-analyzer-based, and grating-based phase-contrast imaging techniques. Many efforts are made to adapt the methods, so that an efficient operation in commonplace research laboratories and a successful integration in clinical devices become possible. X-ray grating interferometry is currently the most promising approach due to its outstanding compatibility with conventional polychromatic X-ray sources. A typical grating-based phase-contrast imaging system in a laboratory environment combines a standard X-ray tube, a Talbot-Lau interferometer consisting of three gratings, and an X-ray detector. The first grating comprises attenuating gold structures and is placed behind the source to create an array of individually coherent but mutually incoherent sources. This allows for interference effects that are induced by the second grating. The resulting interference pattern can then be analyzed by another gold grating, which is mounted directly in front of the detector, to draw conclusions based on beam attenuation and refraction caused by the examined samples.
The technique enables the simultaneous acquisition of spatially fully co-registered conventional attenuation-contrast and phase-contrast 3D volumes, both providing quantitative information about the object. The enhanced visualization of soft tissues that can be achieved by phase contrast has been shown in numerous benchmarking experiments at synchrotron radiation facilities. Since grating interferometry has been demonstrated to properly function with laboratory X-ray tubes, a broad application of X-ray phase-contrast imaging in biomedical research or even in clinical diagnostics is within the realms of possibility. The motivation of the present work is to push the current process of implementation.
The scientific goals of the thesis can be grouped into three parts. First, a lab-based imaging setup is designed that is capable to detect very small refraction angles and, thus, is highly sensitive to measure phase shifts. The system performance is continuously enhanced by optimization to achieve stable CT scans with a soft-tissue contrast that is comparable to synchrotron radiation facilities. Second, a framework is built for the conversion of the 3D attenuation-contrast and phase-contrast volume data into quantitative material properties like linear atten-

uation coefficients, refractive index decrements, electron densities and Hounsfield units. The complementarity of both contrast modalities is investigated to explore the gain of information and the added value of a combined data analysis. Third, biomedical studies are performed in close collaboration with clinical partners to evaluate grating-based X-ray phase-contrast imaging as tool for the 3D examination of excised tissue specimens.
The activities further aim to contribute to the identification of potential clinical cases that might arise or benefit from a realization of medical phase-contrast imaging. In addition, electron densities of various types of soft tissue are quantified. These numbers are relevant for the execution of realistic simulations, the design of adequate phantoms, and the definition of the demands on a clinical phase-contrast device to fulfill certain tasks.
After this introduction, the thesis is structured in the following chapters:
Chapter 2 gives an overview on the interaction between X-rays and matter. Conventional attenuation contrast and different phase-sensitive imaging techniques are introduced.
Chapter 3 explains the principles of X-ray grating interferometry. This includes the theoretical concept, the signal extraction, and the requirements for the operation at standard polychromatic X-ray tubes.
Chapter 4 describes the phase-contrast imaging system that has been installed. The employed components, their configuration, and the influencing factors to reach a high phase sensitivity are discussed. The optimization steps that have been carried out over the time and the resulting setup performance are reported.
Chapter 5 is dedicated to quantitative phase-contrast CT. The basics of tomographic imaging and the general scan procedure applied for tissue examinations are presented. The framework for the retrieval of quantitative information, the electron-density resolution of the system, and the complementarity of both imaging signals (attenuation contrast and phase contrast) are addressed.
Chapter 6 comprises quantitative phase-contrast imaging results that have been evaluated for various non-fixated human soft tissues ranging from adipose, muscle, and connective tissues to liver, kidney, and pancreas tissues. The effect of formalin fixation on quantitative values is investigated on samples of porcine fat and rind.
Chapter 7 focuses on quantitative breast-tissue characterization. Breast specimens containing different tumor types are imaged and correlated to histopathology. Results are compared to both high-quality, high-resolution data obtained with monochromatic synchrotron radiation and calculated values based on tabulated tissue properties.
Chapter 8 illustrates the potential for advanced tissue analysis when exploiting the complementary information content provided by both contrast modalities. Vector decomposition of the experimental data delivers water, protein, and lipid concentrations as exemplified on dairy products, porcine fat and rind, and human

soft tissues.
Chapter 9 is a collection of further research activities and their scientific output. Biomedical studies include, among others, the classification of atherosclerotic plaque and the differentiation of cystic renal lesions. Several methodical developments like stitched gratings to increase the field of view (FOV), grating-based phase-contrast imaging at higher energies, and data acquisition in helical scanning mode are shown.
Chapter 10 summarizes and concludes the work in this thesis. Current shortcomings, challenges, potential next steps, and future perspectives associated with a broad application of (bio-)medical grating-based phase-contrast imaging are outlined.

Chapter 2

Principles of X-ray imaging

2.1 Interaction with matter

X-rays are part of the electromagnetic spectrum covering wavelengths from 5 pm to 10 nm. This corresponds to photon energies in the range of 100 eV to 200 keV. Hard X-rays (above 5–10 keV) can penetrate relatively thick objects and are widely used to reveal the inside of visually opaque objects. The underlying principle of all X-ray imaging methods is the interaction of X-rays with matter (i.e., its atoms). Changes to the electromagnetic wavefront that occur when traversing the object are detected and conclusions on the inner structure can be drawn. The main interaction mechanisms that play a role in the image formation process are photoelectric absorption and scattering.

In atoms, electrons are bound to the nucleus. Depending on the quantum state of an electron, a certain amount of energy, the binding energy, needs to be provided in order to liberate it from the atom. Photoelectric absorption occurs if the incoming photon ejects an electron from the inner shells (K or L) by transferring all of its energy to the electron. Only photons with energies above the binding energies of the electrons contribute to photoelectric absorption. For the explanation of this effect, Albert Einstein was honored with the Nobel Prize in Physics in 1921.

In the case of scattering, elastic processes are distinguished from inelastic interactions. In an elastic (or coherent) scattering process, there is no energy transfer between photon and electron. Elastic scattering at free electrons is called Thomson scattering, while the sum of coherent scattering at electrons in a bound state is referred to as Rayleigh scattering. The process can be best described by using the wave formalism. As charged particles are accelerated when placed in an electric field, an incoming electromagnetic wave forces the electrons of an atom to vibrate according to the temporal oscillation of its electric field. An oscillating charged particle in turn acts as a source and radiates like a small dipole antenna. Inelastic (or incoherent) scattering, also known as Compton scattering, can be il-

lustrated by making use of the particle formalism. The underlying mechanism can be understood as a collision of a photon with an electron, whereby the electron is expelled from the atom. If the photon does not transfer its energy completely to the electron, it is not absorbed but scattered into a different direction. In comparison to elastic scattering, the wavelength of the photon changes due to its loss of energy. Only few photons are scattered inelastically at X-ray energies around 10 keV, but Compton scattering increases with energy and at about 100 keV it becomes the dominating interaction process of X-rays with matter.
In wave optics, a quantitative description of X-ray absorption and scattering effects within a medium becomes possible by introducing the complex refractive index

$$n = 1 - \delta + i\beta. \tag{2.1}$$

The refractive index decrement δ is related to elastic interactions, while the imaginary part of the refractive index, the absorption index β, is associated to the respective inelastic processes. The refractive index is material- and frequency-dependent and contains information on how electromagnetic waves change when penetrating matter. If only the electric field of the wave is considered, a linearly polarized monochromatic plane wave traveling through a medium can be written as

$$\mathbf{\Psi}\left(\mathbf{r}, t\right) = \mathbf{E_0} e^{in\mathbf{kr}} e^{-i\omega t}. \tag{2.2}$$

The first exponential term $\exp\left(in\mathbf{kr}\right)$ describes the spatial oscillation at a given moment in time t and the second term $\exp\left(-i\omega t\right)$ describes the temporal oscillation at a given point in space $\mathbf{r}$. The vector $\mathbf{E_0}$ defines the direction of the electric field, with $|\mathbf{E_0}| = E_0$ being the initial amplitude. It is perpendicular to the wave vector $\mathbf{k}$, which gives the propagation direction of the wave. The wavelength λ is connected to the wave vector via the wave number $k = |\mathbf{k}|$ as follows

$$\lambda = \frac{2\pi}{k}. \tag{2.3}$$

When using the quantum-mechanical particle formalism, the corresponding photon energy is linked to the angular frequency ω of the electromagnetic wave by

$$E = \hbar\omega, \tag{2.4}$$

with $\hbar = 6.58211899 \cdot 10^{-16}$ eVs being the reduced Planck constant.
In vacuum, the refractive index n is unity and a wave propagating in z-direction can be expressed by

$$\Psi_{\text{vacuum}}\left(z, t\right) = E_0 e^{i(kz - \omega t)}. \tag{2.5}$$

A wave traveling through a certain medium, on the other hand, is altered according to

$$\Psi_{\text{medium}}\left(z, t\right) = E_0 e^{i(nkz - \omega t)} = E_0 e^{i(kz - \omega t)} e^{-\beta kz} e^{-i\delta kz}. \tag{2.6}$$

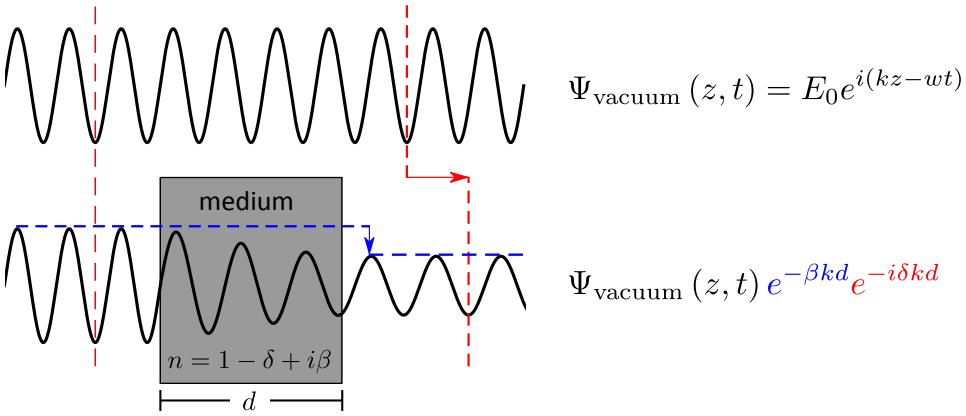

Figure 2.1: An electromagnetic wave propagating in free space compared to one passing a medium with refractive index n and thickness d. Due to the interaction with matter, the second one has a reduced amplitude and is shifted in phase.

The two additional terms cause a decrease of the wave's amplitude $E_0 e^{-\beta kz}$ and a shift in phase $\Delta\Phi = \delta kz$ compared to the reference wave in vacuum. Both effects are illustrated in Figure 2.1.

2.2 Attenuation contrast

The contrast modality that most people associate with X-ray imaging is based on the attenuation of X-rays, which is due to absorption or scattering. More or less photons are lost during penetration resulting in a shadow image, which can be detected behind the object. The famous picture unveiling the bones inside the hand of Wilhelm Conrad Röntgen's wife in 1895 was generated that way and nearly all medical X-ray systems on the market exploit this phenomenon to obtain images for diagnosis.
The quantity of an electromagnetic wave that can be directly measured with X-ray detectors is its intensity

$$I(\mathbf{r}, t) = |\mathbf{\Psi}(\mathbf{r}, t)|^2 . \tag{2.7}$$

The transmission T through an object is then simply defined as the intensity ratio $I_{\text{out}}/I_{\text{in}}$ of the outgoing and the incoming wave, respectively. The higher the attenuation of the X-rays in between, the lower is the transmission and the number of photons that traverse the object. In the example of a wave propagating in z-direction and passing a medium of thickness d, the transmission is given by

$$T = \frac{I_{\text{out}}}{I_{\text{in}}} = \frac{|E_0|^2 e^{-2\beta kd}}{|E_0|^2} = e^{-2\beta kd}. \tag{2.8}$$

In X-ray imaging, the material- and energy-dependent linear attenuation coefficient $\mu = 2\beta k$ is often used to describe the attenuation within an object resulting in the Beer-Lambert law:

$$I_{\text{out}} = I_{\text{in}} e^{-\mu d}. \tag{2.9}$$

The linear attenuation coefficient μ comprises all three types of photon interactions (i.e., photoelectric absorption [ph], incoherent Compton scattering [incoh], and coherent Raleigh scattering [coh]) and can be expressed by

$$\mu = \sum_i \rho_{\text{a},i} \left(\sigma_{\text{a},i}^{\text{ph}} + \sigma_{\text{a},i}^{\text{incoh}} + \sigma_{\text{a},i}^{\text{coh}} \right), \tag{2.10}$$

with $\rho_{\text{a},i}$ being the atomic density of the i-th element in the object. The atomic cross sections $\sigma_{\text{a},i}$ represent the probabilities of a photon to interact with an atom of a certain element i and, thus, to be either absorbed or scattered out of the original path. All three atomic cross sections $\sigma_{\text{a},i}$ exhibit a different dependency on both the energy E of the X-rays and the atomic number Z of the respective element i. The atomic cross sections for carbon ($Z = 6$) and calcium ($Z = 20$) in the energy range of 1 keV to 100 keV are displayed in Figure 2.2.
The dominating interaction process in these examples is photoelectric absorption. A rapid increase in the atomic cross section for photoelectric absorption of calcium can be observed at about 4 keV. This is due to the K-shell electrons of the calcium atoms, which only contribute to the absorption process if the energy of the incoming X-ray photons exceeds the respective binding energy of the electrons. These element-specific *jumps* in the cross-section are called absorption edges. Above the K-edge of an element, the photoelectric cross-section can be approximated by

$$\sigma_{\text{a}}^{\text{ph}}(Z, E) \approx C \frac{Z^k}{E^3}, \tag{2.11}$$

where C only depends on natural constants and the exponent $k \approx 4$ varies slightly depending on the photon energy and element. The proportionality to the fourth power of the atomic number indicates a strong absorption within materials containing higher Z-elements such as calcium in the bones.
Whereas the probability for photoelectric absorption declines with higher X-ray energies, the occurrence of incoherent scattering increases and the Compton effect becomes the main reason for X-ray attenuation at some point. The incoherent scattering cross-section of a photon on a single free electron is given by the relativistic Klein-Nishina cross-section σ_{kn}. The corresponding atomic cross-section is obtained by multiplying σ_{kn} with the number of electrons per atom that interact with the given X-ray photon:

$$\sigma_{\text{a}}^{\text{incoh}}(Z, E) = Z \sigma_{\text{kn}}(E). \tag{2.12}$$

Compared to photoelectric absorption or Compton scattering, only a very small amount of the intensity loss (i.e., the X-ray attenuation) arises from elastic scattering in the hard X-ray regime, waiving the need for a more detailed discussion

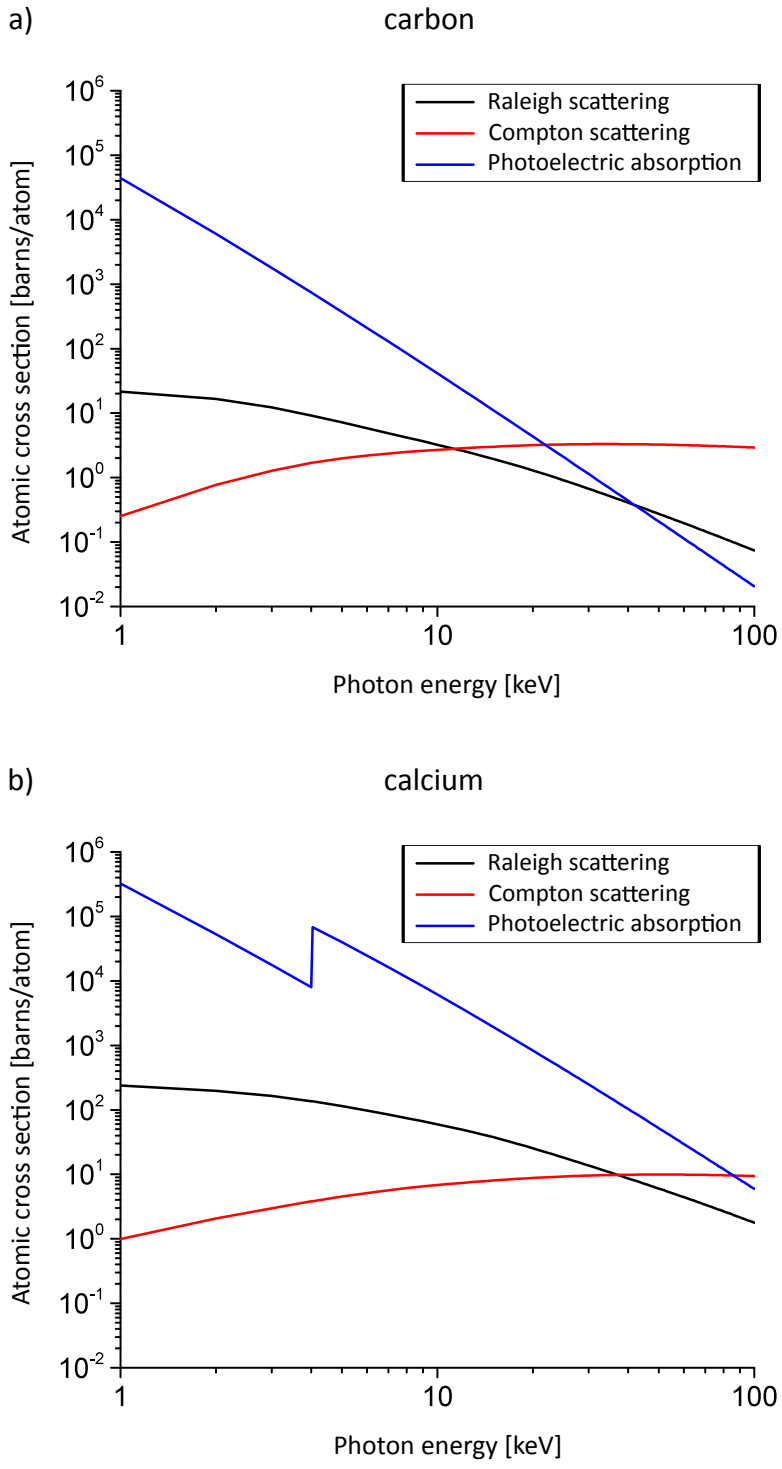

Figure 2.2: Atomic cross sections of photoelectric absorption, Compton scattering, and Raleigh scattering for the elements carbon (a) and calcium (b) in the energy range of 1 keV to 100 keV.

in this context. Coherent scattering, however, is the interaction process being responsible for the aforementioned phase shift of electromagnetic waves, which can be utilized for X-ray imaging as well.

2.3 Phase contrast

The phase shift $\Delta\Phi$ that is introduced when X-rays penetrate a homogeneous object of thickness d

$$\Delta\Phi = \delta k d \tag{2.13}$$

is closely connected to the refractive index decrement

$$\delta = \frac{r_0 h^2 c^2}{2\pi E^2} \sum_i \rho_{\mathrm{a},i} f_i^1, \tag{2.14}$$

where r_0 is the classical electron radius, h is the Planck constant, c is the speed of light and f_i^1 is the real part of an element's atomic scattering factor in the forward direction. Far away from any absorption edges, f_i^1 can be replaced by the element's atomic number Z_i. Then, the sum $\sum_i \rho_{\mathrm{a},i} f_i^1$ reflects the electron density ρ_e of the material. Above 5 keV, this applies to all materials that are composed of elements with atomic numbers $Z < 20$ as it is the case for biological soft tissues. The refractive index decrement δ can then be expressed by

$$\delta = \frac{r_0 h^2 c^2 \rho_\mathrm{e}}{2\pi E^2}. \tag{2.15}$$

The following example shall demonstrate the high potential of exploiting the phase shift for X-ray imaging, especially of low absorbing objects. At an X-ray energy of 25 keV, the linear attenuation coefficient μ and the refractive index decrement δ of muscle tissue are $\mu = 0.561$ 1/cm and $\delta = 3.84 \cdot 10^{-7}$, respectively. Assuming that X-rays of this energy pass a 100 µm-thin layer of muscle tissue, the induced phase shift is $\Delta\Phi \approx 1.55\pi$ according to Equation 2.13. The attenuation by the tissue layer following the Beer-Lambert law, on the other hand, is only about 0.56 %. Unfortunately, the phase of electromagnetic waves cannot be measured directly and, thus, the phase information is not yet widely used as contrast modality in X-ray imaging.
Several approaches that aim at transferring the small phase shifts into measurable intensity changes evolved over the last decades and are illustrated in Figure 2.3. The first X-ray phase-contrast imaging technique was developed by Bonse & Hart (1965) and is known as crystal interferometry. The method is typically based on three crystals to split one X-ray beam in two and let one beam pass through the sample before the two beams are recombined. The phase shift that is induced by the sample can then be extracted from the interference pattern of the recombined

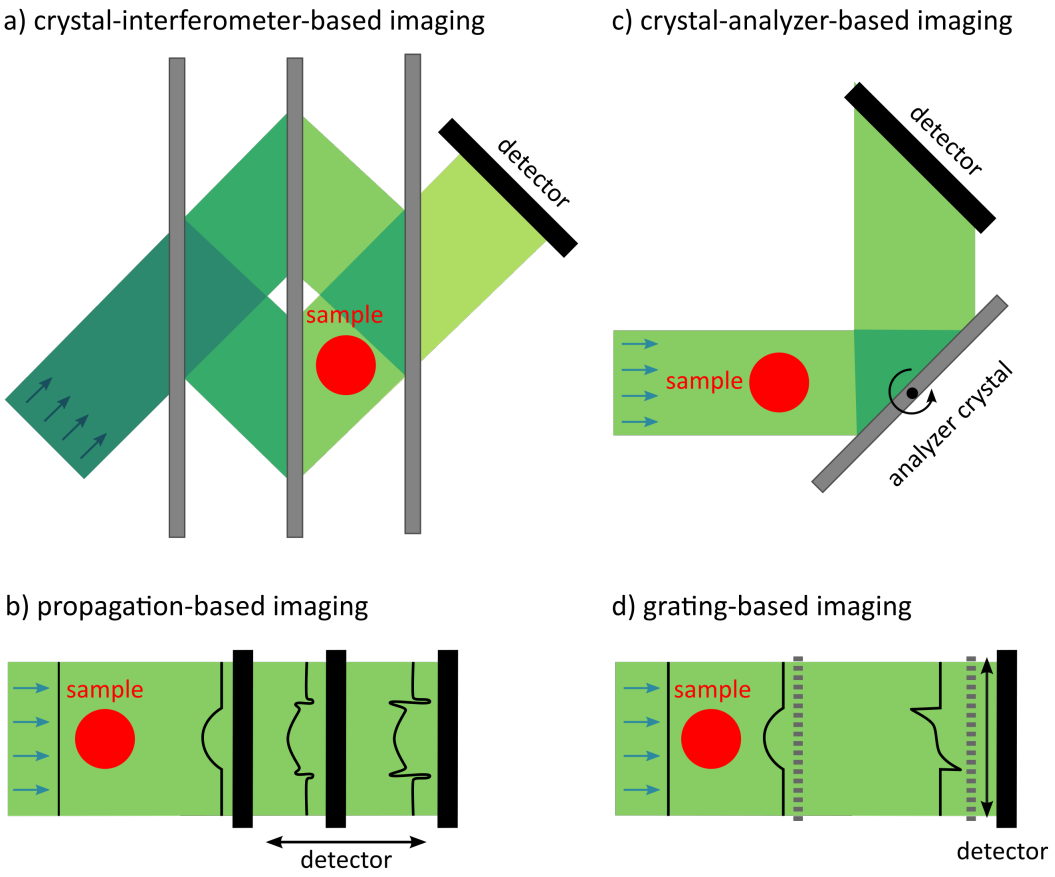

Figure 2.3: Schematics of different phase-contrast imaging techniques. [Figure adapted from Schleede (2013).]

beams. Crystal interferometry is very phase-sensitive and a quantitative reconstruction of the full complex refractive index is possible (Momose 1995, Beckmann et al. 1997). A crystal interferometer as sketched in Figure 2.3a demands a very high mechanical stability, because the crystals have to be aligned with a precision on the order of the X-ray wavelength (Momose 2003). As the silicon crystals act as monochromator, a large part of the incoming radiation is filtered out and very long exposure times are needed to take images. In addition, the sample size is limited by the separation of the beam paths.

In propagation-based phase-contrast imaging (shown in Figure 2.3b), no optical elements are required at all (Snigirev et al. 1995). By increasing the distance between sample and detector, interference fringes arise due to Fresnel diffraction. The so-called edge-enhanced images that can then be recorded contain information about the second derivative of the phase of the wavefront (Cloetens et al. 1997). The approach can also be utilized at polychromatic laboratory X-ray sources (Wilkins et al. 1996). However, the source size has to be rather small to

ensure interference effects and a high-resolution detector is needed to observe the fringes. This leads to longer exposure times and limits the FOV. Quantitative imaging is possible, if the object fulfills certain restrictions like low absorption or a single material constraint (Paganin et al. 2002). Otherwise, several images have to be taken at different detector positions to successfully retrieve the complex refractive index (Cloetens et al. 1999).
Refraction is directly connected to the phase shift of X-rays and, thus, can be exploited for phase-contrast imaging as well. Refraction takes place, when X-rays pass through the boundary between two different homogeneous media with refractive indices n_1 and n_2. According to Snell's law, the angle of incidence α_1 and the exit angle α_2 are related by

$$n_1 \sin(\alpha_1) = n_2 \sin(\alpha_2). \tag{2.16}$$

The refraction of X-rays caused by a wedge in the beam path is demonstrated in Figure 2.4a. There is no refraction, when the X-rays strike the interface of the wedge at normal incidence. But when they are leaving the wedge through the second boundary, the X-rays are refracted by the angle $\alpha_\mathrm{r} = \alpha_1 - \alpha_2$.
A different way to look at the refraction caused by the wedge is to consider the incoming wave as a superposition of monochromatic plane waves (Figure 2.4b). Assuming the waves to be in phase and to propagate parallel to each other in z-direction, their collective wavefront is perpendicular to the propagation direction and parallel to the surface of the wedge. The phase shift $\Delta\Phi(x)$ that is induced by the wedge varies for the single waves depending on its thickness at the respective position (in x-direction). As a consequence of this local variation in phase shift, the outgoing wavefront is tilted by the angle

$$\alpha_\mathrm{r}(x) = \frac{\lambda}{2\pi} \frac{\partial\Phi(x)}{\partial x} \tag{2.17}$$

compared to the incident wavefront. Here, the small angle approximation was applied. The angular refraction α_r of the X-rays is therefore proportional to their wavelength (energy) and the differential phase shift introduced by the object.
Although typical refraction angles are in the regime of nano-radians, they can be detected, for example, by mounting a crystal analyzer between the sample and the detector (Ingal & Beliaevskaya 1995, Davis et al. 1995). Only X-rays in a small angular range are reflected by the crystal, so that the refraction angle can be determined by tilting the crystal and monitoring the corresponding intensity. The technique is called analyzer-based imaging and is illustrated in Figure 2.3c. While a good sensitivity towards minor phase variations can be achieved, a monochromatic and highly collimated beam is required. For this reason, attempts to transfer the method from synchrotron radiation to standard X-ray sources suffer from very long exposure times and are hardly feasible (Parham et al. 2009, Nesch et al. 2009).

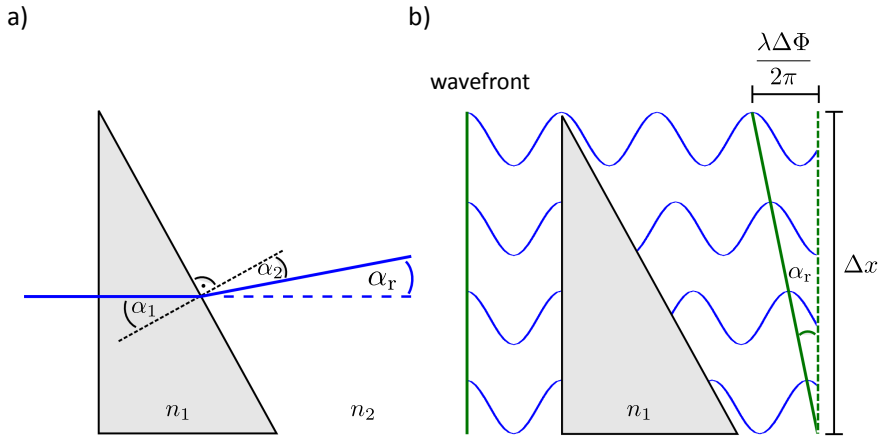

Figure 2.4: Refraction caused by a wedge. The angular deviation α_r can be determined by applying Snell's law (a) or by considering a plane wavefront that is differently shifted in phase when penetrating the wedge (b).

Another approach, which is capable of resolving tiny refraction angles, is grating interferometry (Momose et al. 2003, Weitkamp et al. 2005). The schematics of a grating interferometer is shown in Figure 2.3d and the working principle is described in detail in the following chapter. Since the successful translation of the method to be operated at conventional sources by Pfeiffer et al. (2006), it is the most promising candidate for lab-based or clinical X-ray phase-contrast imaging. For further information on the different phase-contrast imaging techniques, the reader is referred to Momose (2005) or Bravin et al. (2013). A detailed introduction to the principles of X-ray imaging is given by Als-Nielsen & McMorrow (2008).

Chapter 3

X-ray grating interferometry

3.1 Working principle

When Henry Fox Talbot (1836) placed a grating in visible light, he observed that an image of the grating appeared at regular distances behind it. This self-imaging phenomenon of periodic structures applies to X-rays as well. If a modulation of the wavefront is induced by a grating of period p, it is reproduced at certain propagation distances, called Talbot distances

$$d_{\mathrm{T}} = \frac{2p^2}{\lambda}. \tag{3.1}$$

Additionally, various intensity patterns can arise at distances between the grating and the Talbot distance d_{T} as described by Suleski (1997) or Lohmann et al. (2005). Besides the grating period p and the wavelength λ of the X-rays, these distances further depend on the phase shift $\Delta\Phi$ introduced by the grating bars and on the duty cycle κ of the grating, which is defined as the ratio of bar width and period. The propagation of a wavefront all the way to its Talbot distance d_{T} for two different gratings with duty cycles of 0.5 is shown in Figure 3.1. Both gratings are pure phase gratings implying that no attenuation, but only a phase modulation of the wavefront, takes place. In the first case, the phase of the wavefront is shifted by π (Figure 3.1a) and in the other case, it is shifted by $\pi/2$ (Figure 3.1b). The displayed figures are called *Talbot carpets* and illustrate the intensity modulations with periods of

$$p_{\mathrm{e}}(\pi) = p/2 \tag{3.2}$$

and

$$p_{\mathrm{e}}(\pi/2) = p \tag{3.3}$$

that occur at fractional Talbot distances of

$$d_n(\pi) = \frac{n}{16} d_{\mathrm{T}} = n\frac{p^2}{8\lambda} \tag{3.4}$$

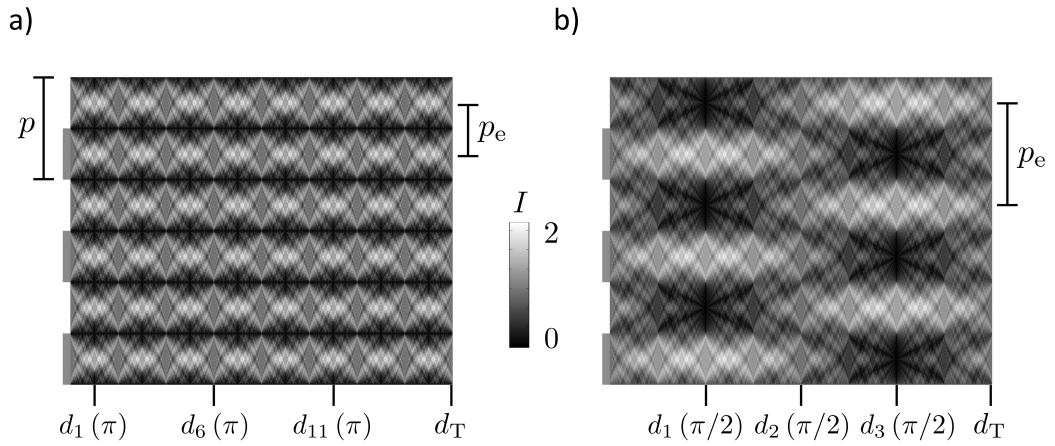

Figure 3.1: Interference patterns produced by a π-shifting (a) and a $\pi/2$-shifting phase grating (b) with period p and duty cycles of 0.5. A periodic wavefront repeats itself at the Talbot distance d_T. In addition, intensity patterns with period p_e arise at odd fractional Talbot distances.

and

$$d_n(\pi/2) = \frac{n}{4} d_T = n\frac{p^2}{2\lambda}, \tag{3.5}$$

where $n = 1, 3, 5, ...$ is an odd integer.
As described in the previous chapter, a sample in the beam causes slight angular deviations $\alpha_r(x, y)$ (Equation 2.17) in the propagation direction of a wavefront due to refraction. By placing a phase grating (often denoted by G1) behind the object, this results in a lateral shift $S(x, y)$ of the interference pattern downstream

$$S(x, y) = \alpha_r(x, y)\, d = \frac{\lambda}{2\pi} \frac{\partial \Phi(x, y)}{\partial x} d, \tag{3.6}$$

where d is the distance from the phase grating. Thus, the measurement of the exact lateral position of the intensity modulation, with and without sample, allows to arrive at conclusions on the differential phase shift $\partial\Phi(x, y)/\partial x$ entailed by the object.
In order to capture refraction angles below one micro-radian, the period of the employed grating should be on the order of a few microns. At the same time, the spatial resolution of the X-ray detector (i.e., its pixel size) has to be less than one third of the resulting intensity pattern period p_e. Otherwise, the lateral shift and the corresponding refraction angle cannot be reliably determined. While high-resolution (below 10 µm) detectors are often used for X-ray imaging at synchrotron radiation facilities, the pixel sizes of standard X-ray detectors for biomedical applications range from $100\times100\,\mu m^2$ to $1\times1\,mm^2$.
The limitation by the detector resolution can be eluded with the application of a second grating made of a highly absorbing material like for example gold. This

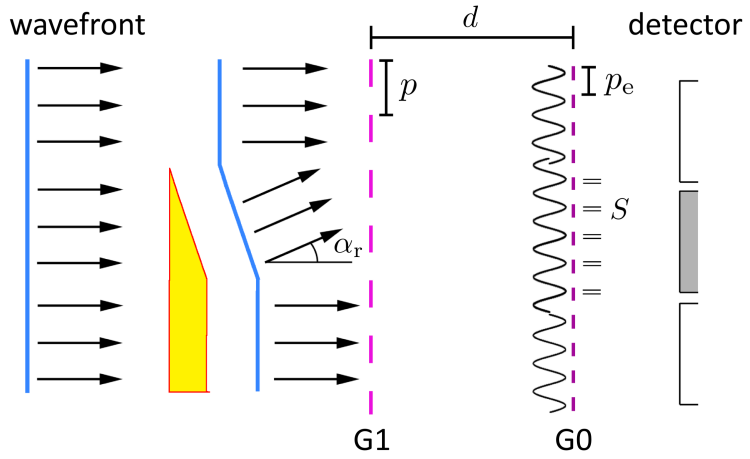

Figure 3.2: The refraction of X-rays caused by a sample in the beam results in a lateral shift of the interference pattern behind the phase grating G1. The shift can be detected by placing an analyzer grating G2 with period p_e at an odd fractional Talbot distance d_n. The intensity recorded by a detector pixel then depends on the relative position of the intensity pattern to the grating.

so-called analyzer grating (often denoted by G2) is usually set up at an odd fractional Talbot distance d_n behind the phase grating G1 and its period p_2 is chosen to match the one of the intensity pattern p_e. Then, the intensity that is recorded at a given detector pixel depends on the lateral position of the analyzer grating G2 relative to the intensity pattern (Momose et al. 2003, Weitkamp et al. 2005). A local shift $S(x, y)$ of the pattern due to refraction by the sample is then noticeable as an intensity change within the respective detector pixel located at the coordinates (x, y). A graphical representation of the working principle of a grating interferometer is shown in Figure 3.2.

3.2 Signal extraction

For a quantitative evaluation of refraction angles $\alpha_r(x, y)$, the exact position of the intensity pattern has to be determined, once with and once without a sample in the beam. This can be accomplished by recording and analyzing so-called stepping curves. In this process, one of the gratings, for example G2, is laterally moved along the intensity pattern over at least one period, while several images are acquired. Different positions of the analyzer grating x_g result in low and high intensities behind the grating, depending on whether the interference pattern is covered by grating bars or not. The intensity oscillation $I(x_g, x, y)$ in each detector pixel with coordinates (x, y) contains information on the shape and position of the respective pattern. Mathematically, the curve represents a

convolution of the box-shaped interference pattern with the profile of the X-ray source and the box-shaped function defined by the absorbing bars of the analyzer grating. It can be expressed using a Fourier-series

$$I\left(x_{\mathrm{g}}, x, y\right) = \sum_{m=0}^{\infty} a_m\left(x, y\right) \cos\left(m \frac{2\pi}{p_2} x_{\mathrm{g}} + \phi_m\left(x, y\right)\right), \tag{3.7}$$

where a_m and ϕ_m are the amplitude and phase coefficients, respectively. In case of limited beam coherence due to an extended source size or a polychromatic spectrum, higher-order harmonics can be neglected and the function is well approximated with a cosine curve

$$I\left(x_{\mathrm{g}}, x, y\right) = a_0\left(x, y\right) + a_1\left(x, y\right) \cos\left(\frac{2\pi}{p_2} x_{\mathrm{g}} + \phi_1\left(x, y\right)\right), \tag{3.8}$$

which is sufficiently described by the offset a_0 (average value), the amplitude a_1, and the relative phase ϕ_1 (Bech 2009). At least three data points per period have to be recorded by each detector pixel during the aforementioned stepping scan in order to extract these parameters from the measured intensity values by applying a cosine fit or a Fourier analysis. The whole procedure is performed twice to finally obtain the refraction angles $\alpha_{\mathrm{r}}\left(x, y\right)$: once without a sample in the beam, which is called flat-field or reference scan and subsequently denoted by the superscript 'r', and once with the sample in the beam, which is denoted by the superscript 's'. The difference in the relative phase $\Delta\phi_1\left(x, y\right) = \phi_1^s\left(x, y\right) - \phi_1^r\left(x, y\right)$ of both stepping curves is then directly proportional to the shift of the intensity pattern by

$$S\left(x, y\right) = \frac{p_2}{2\pi} \Delta\phi_1\left(x, y\right) \tag{3.9}$$

and to the corresponding refraction angle by

$$\alpha_{\mathrm{r}}\left(x, y\right) = \frac{p_2}{2\pi d} \Delta\phi_1\left(x, y\right). \tag{3.10}$$

Figure 3.3 shows exemplary stepping curves from a reference scan (blue) and a scan with sample (red). In addition to the shift of the curve due to refraction, a decrease of the average value a_0 can be observed. This change can be traced back to the Beer-Lambert law (Equation 2.9)

$$a_0^{\mathrm{s}}\left(x, y\right) = a_0^{\mathrm{r}}\left(x, y\right) e^{-\mu(x,y)z} \tag{3.11}$$

and reflects the transmission through the sample

$$T\left(x, y\right) = \frac{a_0^{\mathrm{s}}\left(x, y\right)}{a_0^{\mathrm{r}}\left(x, y\right)}. \tag{3.12}$$

Hence, information on the attenuation by the object can be obtained simultaneously, but clearly separated from any refraction effects, when using a grating

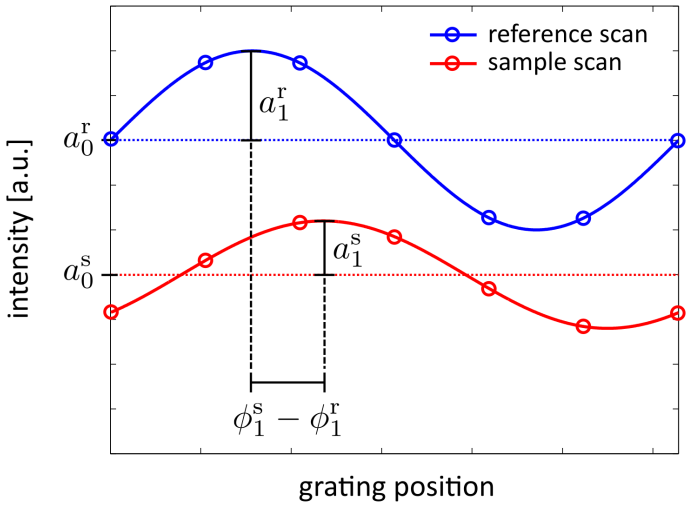

Figure 3.3: Recorded stepping curves of a measurement with sample (red, superscript s) and a reference scan without sample (blue, superscript r) in the beam. The curves illustrate the change in intensity that occurs within one detector pixel while stepping the analyzer grating along the intensity pattern. Conclusions on the attenuation and refraction caused by the object can be drawn by comparing both curves through Fourier analysis.

interferometer. Another parameter that can be gained by recording a stepping curve is the visibility

$$V = \frac{a_1}{a_0}. \tag{3.13}$$

A high ratio of the curve's amplitude a_1 and its offset a_0 is important for a good performance of the interferometer. The visibility comprises both the quality of the interference pattern that is created by the phase grating and the capability of the analyzer grating to translate the pattern into measurable intensity alterations. If the visibility is too low, the relative phase ϕ_1 of the stepping curve cannot be determined properly and it is not possible to recover any refraction angle.
The visibility can be further exploited as a third imaging modality known as dark-field contrast (Pfeiffer et al. 2008). Coherent small angle scattering caused by high-density fluctuations on the (sub-)microscale degrades the interference pattern and thereby reduces the visibility. Thus, the dark-field signal

$$D\left(x,y\right) = \frac{V^{\mathrm{s}}\left(x,y\right)}{V^{\mathrm{r}}\left(x,y\right)} = \frac{a_1^{\mathrm{s}}\left(x,y\right) a_0^{\mathrm{r}}\left(x,y\right)}{a_0^{\mathrm{s}}\left(x,y\right) a_1^{\mathrm{r}}\left(x,y\right)} \tag{3.14}$$

is sensitive to microstructures within the sample.
In summary, X-ray grating interferometry and the stepping procedure provide three different fully co-registered types of images: the conventional attenuation

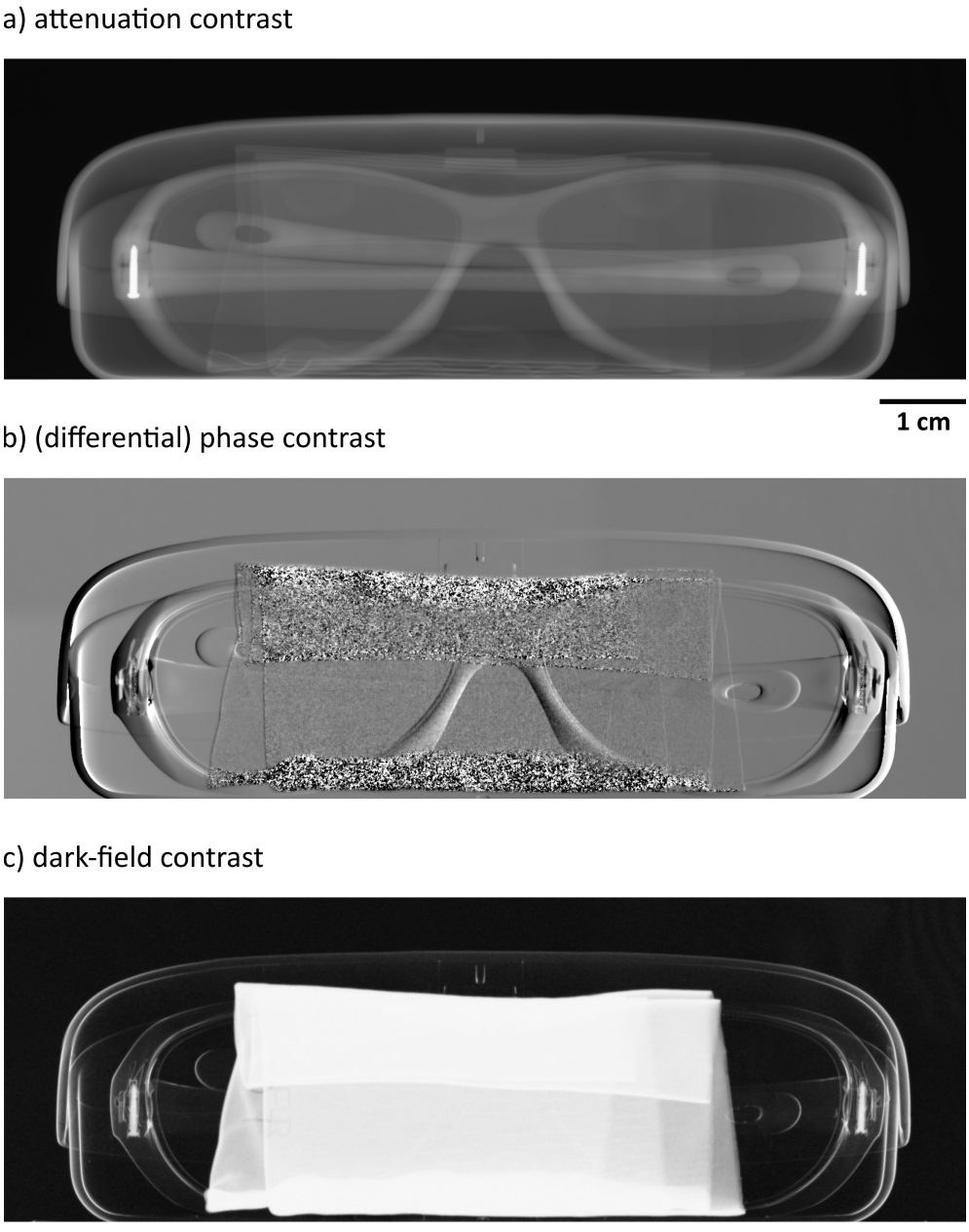

Figure 3.4: Imaging results of sunglasses and a cleaning cloth placed within a case obtained by X-ray grating interferometry. Three different but fully co-registered images can be extracted from the recorded stepping curves: the conventional attenuation contrast (a), the differential phase contrast (b), and the dark-field contrast (c).

contrast, the differential phase contrast based on refraction, and the dark-field contrast. In order to visualize the complementarity and novelty of the three contrast modalities, imaging results of sunglasses and a cleaning cloth placed within a case are presented as an example in Figure 3.4. While the attenuation image indeed depicts highly absorbing structures, in this case the screws, very well, other superimposing features of low optical density remain hidden. The differential nature of the phase-contrast image becomes apparent in the opposite signal on both sides of the case. The signal at the upper side of the case is comparably low, because the refraction occurs parallel to the grating bars and cannot be detected by the interferometer. The thin cleaning cloth is clearly visible in the dark-field image due to small angle scattering arising from the threads. The visibility behind the cloth is reduced to nearly zero, so that the phase signal cannot be retrieved anymore as described above. In this case, statistical noise appears as sprinkled white and black dots in the differential phase-contrast image.

3.3 Laboratory setting

All considerations so far were based on the assumption that the gratings are illuminated by a parallel beam (i.e., a plane wavefront). This can be realized at synchrotron radiation facilities, where the source size is very small and the distance to the sample is long. In a laboratory environment, the divergence of the beam and the extended size of the source have to be additionally taken into account when designing a grating interferometer. Both effects are illustrated in Figure 3.5.
The beam divergence causes a magnification M of the interference pattern given by

$$M = \frac{L + d}{L}, \tag{3.15}$$

where L is the distance from the source to phase grating G1 and d is the distance from G1 to analyzer grating G2, respectively. As a consequence, the period of the analyzer grating has to be adjusted according to

$$p_2 = p_{\mathrm{e}}^{\mathrm{mag}} = M p_{\mathrm{e}} \tag{3.16}$$

and the Talbot distance is rescaled by

$$d_{\mathrm{T}}^{\mathrm{mag}} = M d_{\mathrm{T}}. \tag{3.17}$$

The impact of an extended source size s can be best described by considering the source as a sequence of individual point sources located side by side. Two point sources that are separated by a distance ϵ from each other generate two laterally shifted interference patterns behind the phase grating. This displacement of the

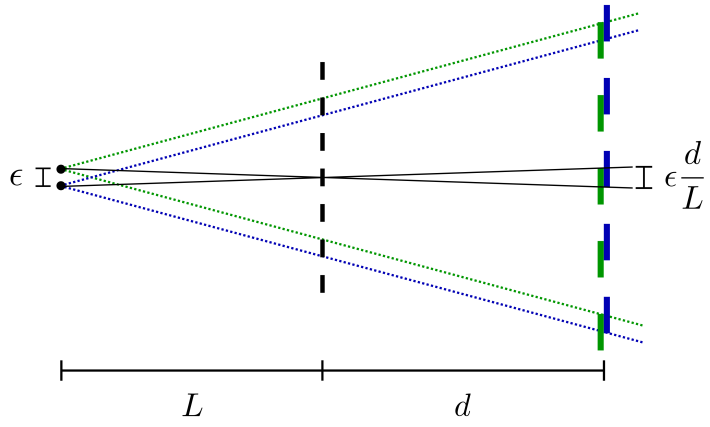

Figure 3.5: Beam divergence leads to a magnification of the interference pattern behind the phase grating. The period of the analyzer grating has to be adjusted accordingly. The effect of an extended source size can be demonstrated by two separated point sources. The resulting interference patterns are shifted relative to each other and the superimposed intensity pattern smears out.

distance $\epsilon d/L$ relative to each other results in a blurring of the superimposed intensity pattern (Figure 3.5) and a decrease in visibility. A minimum visibility is reached for $\epsilon d/L = p_{\mathrm{e}}^{\mathrm{mag}}/2$, when the maxima and minima of both point sources superimpose and no intensity modulation can be observed anymore. Therefore, the width of the source should not exceed

$$s = \frac{p_{\mathrm{e}}^{\mathrm{mag}} L}{2d}, \tag{3.18}$$

because the contributions from, colloquially speaking, the upper and lower end of the source would overlap in an unfavorable manner and result in a flatting of the intensity profile. If the source size s is too large and the X-ray tube cannot be placed sufficiently far away from the interferometer to guarantee a satisfactory quality of the interference pattern, a thin slit can be placed behind the source at the cost of a significant loss of beam intensity. Alternatively, a whole array of slits by means of an additional highly absorbing grating can be installed close to the source. Thereby, each slit acts as individual point source and generates its own interference pattern. The patterns overlay constructively if the period of this source grating (often denoted by G0) is chosen to be

$$p_0 = p_{\mathrm{e}}^{\mathrm{mag}} \frac{L}{d} = p_2 \frac{L}{d}, \tag{3.19}$$

where L is now the distance between the source grating, acting as *new source*, and the phase grating. This three-grating approach was introduced by Pfeiffer

et al. (2006) and is called Talbot-Lau interferometer.
A grating interferometer is rather insensitive to a broader spectral bandwidth and can be routinely operated at polychromatic X-ray tubes, which are predominantly used in a laboratory setting (Weitkamp et al. 2005, Engelhardt et al. 2008). However, because the phase shift $\Delta\Phi$ depends on the wavelength (Equation 2.13), the phase grating G1 introduces a phase shift of π or $\pi/2$ to only one certain energy, which is the selected design energy of the interferometer. The same applies to the fractional Talbot distance d_n (Equations 3.4 and 3.5), where the analyzer grating G2 is positioned. All other energies within the X-ray spectrum of the source are differently shifted in phase and the corresponding interference patterns are additionally analyzed at positions that vary from their respective fractional Talbot order. The superimposed intensity pattern is blurred in consequence and the achievable visibility of the interferometer is distinctively lower than compared to the monochromatic case. Figure 3.6 shows monoenergetic visibilities simulated for a Talbot-Lau interferometer with the period of the analyzer grating p_2 being chosen to match $p_\mathrm{e}^\mathrm{mag}(\pi/2) = Mp_1$. The introduced phase shift was varied between 0 and 2π for the simulation. In addition, the position of the analyzer grating was gradually changed from 0 up to a distance of $1.5d_\mathrm{T}$ away from the phase grating. Referencing to the previously discussed *Talbot carpets* (Figure 3.1), this kind of graph is named *visibility carpet* (Willner 2011, Hipp et al. 2014). A perfect attenuation within the grating bars of G0 and G2 was assumed in the simulation and the duty cycles of all three gratings were 0.5. As expected, the best visibility values are obtained for a phase shift of $\pi/2$ or $3\pi/2$ at the odd fractional Talbot distances d_1, d_3, and d_5. However, good visibility values can be further observed for slightly deviating phase shifts and positions that differ from the odd fractional Talbot distances. At the Talbot distance and the even fractional Talbot distances no intensity patterns arise and the visibility is zero. No visibility is attained for a phase shift of π. In this case, the resulting interference pattern is half the period of the utilized analyzer grating. The intensity pattern for a phase shift of $\pi/2$ at the first fractional Talbot order d_1 and the corresponding one at the third fractional Talbot order d_3 are shifted by half a period with respect to each other (see Figure 3.1). This is indicated by the labeling $V(\phi_1 = 0)$ and $V(\phi_1 = \pi/2)$. A polychromatic source can be represented by a line within the *visibility carpet*. Its slope depends on the material and height of the phase grating and on the position of the analyzer grating. The overall visibility of the interferometer is then the sum of all monoenergetic visibility values weighted by their contribution to the source spectrum. When designing a laboratory Talbot-Lau interferometer, all these aspects have to be taken into account to maximize the visibility and, thus, the performance of the imaging system.

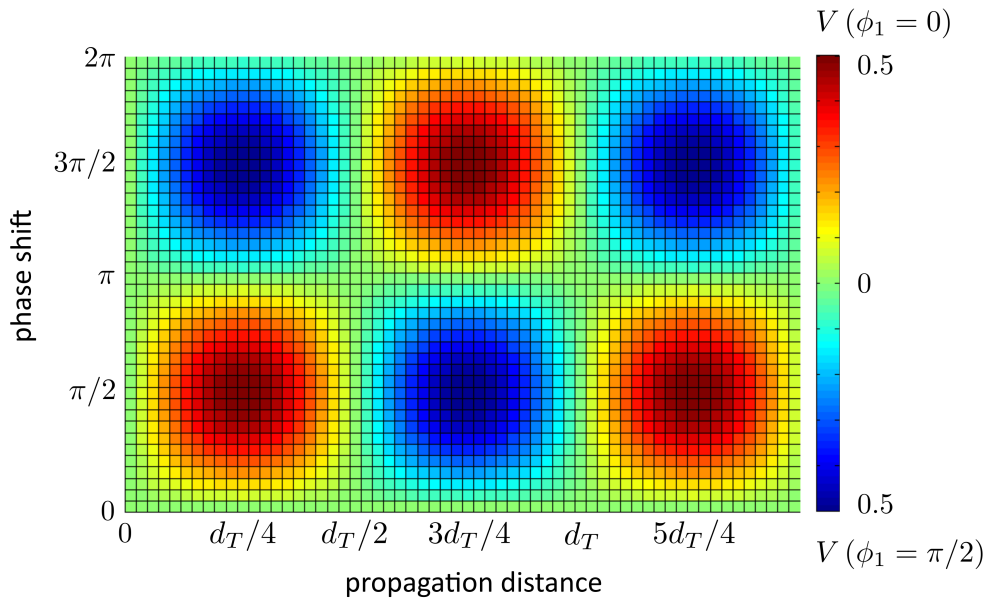

Figure 3.6: Monoenergetic visibility values that were simulated for varying phase shifts induced by the phase grating and for different positions of the analyzer grating. The period of the analyzer grating p_2 is chosen to match the period of the intensity pattern $p_\mathrm{e}\,(\pi/2)$ arising from a $\pi/2$ phase shift. For this reason, the best visibility values are obtained for $\Delta\Phi = \pi/2$ and $\Delta\Phi = 3\pi/2$ at the corresponding odd fractional Talbot distances $d_{1,3,5}\,(\pi/2)$.

Chapter 4

Experimental setup

4.1 Sensitivity

X-ray grating interferometry is by now a well-established phase-contrast imaging technique at synchrotron radiation facilities for the investigation of biological tissue samples (Momose et al. 2006, Pfeiffer et al. 2007a, McDonald et al. 2009, Schulz et al. 2010). The successful translation to laboratory sources in 2006 was followed by several studies that demonstrated the high potential of the method for a broad application in biomedical imaging (Bech et al. 2009, Donath et al. 2010, Kottler et al. 2010). However, the image quality obtained at the first laboratory prototype systems was clearly degraded compared to the results obtained at synchrotrons. The first goal within the scope of this thesis was the design and subsequent optimization of an experimental phase-contrast imaging setup with high phase sensitivity for tissue examinations in a laboratory setting.
The smaller the refraction angles that can be resolved by the setup, the higher the phase sensitivity that can be realized. For this purpose the signal-to-noise ratio

$$\mathrm{SNR}_{\Delta\phi_1} = \frac{\Delta\phi_1}{\sigma_{\Delta\phi_1}} \tag{4.1}$$

of the data extracted from the stepping curves has to be maximized. As described in the previous chapter, the difference in the relative phase $\Delta\phi_1$ of the stepping scans with and without sample is directly connected to the refraction angle α_r by

$$\Delta\phi_1 = \frac{2\pi d}{p_2}\alpha_\mathrm{r}. \tag{4.2}$$

In case of large refraction angles, the intensity pattern is shifted by more than one period and the relative phase is wrapped back into the interval]-π,π]. This so-called phase wrapping due to the limited dynamic range of the relative phase can distort the phase-contrast imaging results as will be discussed later in Chapter 5.

An analytical formula for the noise of the relative phase σ_{ϕ_1} is given by

$$\sigma_{\phi_1} = \frac{\sqrt{2}}{V\sqrt{N}}, \tag{4.3}$$

where V is the visibility of the interferometer and N is the total number of photons over all acquired images during the stepping scan (Engel et al. 2011). The relation is based on Fourier analysis of the stepping curve and is restricted to pure quantum (Poisson) noise, which implies that any read-out noise by the detector is neglected. In addition, perfectly accurate stepping positions are assumed. Both the detector and jitter of the gratings can increase the actual noise of the retrieved relative phase (Revol et al. 2010). The dependency of the noise on the visibility and the total photon counts was further confirmed by a least-square-fit analysis of the stepping curve (Weber et al. 2011). Equation 4.3 is not valid for very low photon counts. Statistical phase wrapping then causes a uniform distribution of the relative phase on the interval]-π,π], which leads to a constant noise level of

$$\sigma_{\phi_1} = \sqrt{\frac{\pi^2}{3}} \tag{4.4}$$

as described by Chabior (2011). Because two stepping scans, the one with sample and the reference flat-field without the sample, are needed to determine the difference in the relative phase $\Delta\phi_1$, the noise of both acquisitions adds up according to

$$\sigma_{\Delta\phi_1} = \sqrt{\sigma^2_{\phi_1^{\mathrm{s}}} + \sigma^2_{\phi_1^{\mathrm{r}}}}. \tag{4.5}$$

Assuming the same noise levels in the processed images ($\sigma_{\phi_1^{\mathrm{s}}} = \sigma_{\phi_1^{\mathrm{r}}}$) and following Equations 4.2 and 4.3, the signal-to-noise ratio can be expressed by

$$\mathrm{SNR}_{\Delta\phi_1} = \alpha_{\mathrm{r}} \frac{2\pi d}{p_2} \frac{V\sqrt{N}}{2}. \tag{4.6}$$

The considerations so far can be directly transferred to the signal-to-noise ratio of the actual refraction angle α_{r} as given by

$$\mathrm{SNR}_{\alpha_{\mathrm{r}}} = \frac{\alpha_{\mathrm{r}}}{\sigma_{\alpha_{\mathrm{r}}}}. \tag{4.7}$$

A comparison to Equation 4.6 yields a corresponding noise level of

$$\sigma_{\alpha_{\mathrm{r}}} = \frac{p_2}{2\pi d} \frac{2}{V\sqrt{N}} \tag{4.8}$$

and defines the smallest detectable refraction angle

$$\alpha_{\mathrm{r,min}} \equiv \sigma_{\alpha_{\mathrm{r}}}. \tag{4.9}$$

This minimum resolvable refraction angle $\alpha_{\mathrm{r,min}}$ is a good measure to quantify the sensitivity of a grating-based phase-contrast imaging system (Modregger et al. 2011, Thüring et al. 2012).

4.2 Source

The first step in the interferometer design is the choice of an X-ray source that generates X-rays in a suitable energy range. As mentioned in Chapter 2, the refraction angle correlates with the differential phase shift introduced by the sample

$$\alpha_\mathrm{r} = \frac{\lambda}{2\pi}\frac{\partial\Phi}{\partial x}. \tag{4.10}$$

The refractive index decrement δ is proportional to $1/E^2$ (Equation 2.14), so that the phase shift $\Delta\Phi = \delta kd$ (Equation 2.13) induced by the sample is energy-dependent with $\Delta\Phi \propto 1/E$. Thus, the measured refraction angle α_r shows the energy dependence

$$\alpha_\mathrm{r} \propto 1/E^2. \tag{4.11}$$

As a consequence, the refraction angles caused by the sample become larger when working at lower energies and are therefore easier to detect. At the same time, the increased attenuation of lower energy photons leads to higher noise according to Equation 4.3 and, thus, to a reduced sensitivity. Taking the attenuation by the silicon wafers that carry the grating structures into account and assuming soft-tissue samples of 2–4 cm in diameter, the optimum trade-off between signal and counts is achieved for energies in the range of 20 to 30 keV.
The two main components of a conventional laboratory X-ray tube are the cathode and the anode. A current flows through a filament in the cathode, which emits electrons based on the thermo-electric effect. The free electrons are accelerated towards the anode of the tube by applying a voltage U. As they strike the target, X-rays are produced. In this process, two different X-ray origination mechanisms can be distinguished. On the one hand, the electrons are decelerated in the electric fields of the atoms in the anode and as a consequence irradiate X-rays, which are known as *Bremsstrahlung*. Their energy distribution is continuous, but limited to the maximal kinetic energy $E_\mathrm{kin} = eU$ of the electrons. On the other hand, the electrons collide with tightly bound electrons in the target material causing the electrons to be expelled from their atomic shell, whereupon weakly bound electrons from higher orbitals fill the vacant quantum states. The gained energy is released as photons. The energies of the resulting photons are the differences between the former binding energies of the electrons and the binding energies of their new quantum states. Similar to the absorption edges, these energies are characteristics of the utilized anode material and therefore referred to as characteristic spectrum.
About 99 % of the kinetic energy of the accelerated electrons is converted to heat and the maximum power of the tube is limited due to the ultimate stress of the anode material. The outcoming X-ray flux can be significantly increased by using high-power rotating-anode X-ray sources. As indicated by the name, an anode ring is rotating up to 6000 times per minute or even faster and the heat is dis-

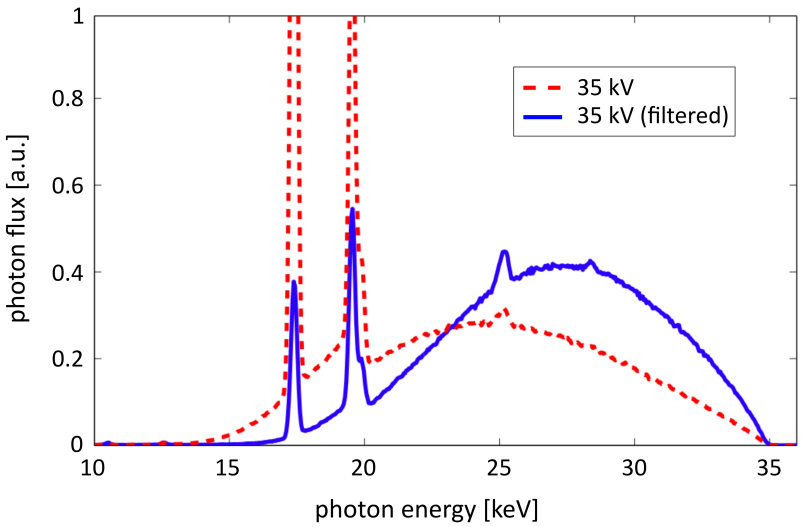

Figure 4.1: Two exemplary energy spectra of the rotating molybdenum anode X-ray source *Enraf Nonius FR 591*. The red dashed line represents the spectrum that arises from a tube voltage of 35 kV. A modified spectrum, which is caused by the attenuation of a 3 cm-thick soft-tissue sample in the beam, is illustrated by the blue line. [Figure adapted from Hipp (2013).]

tributed on the anode surface instead of being concentrated on one single spot. The rotating-anode X-ray tube *Enraf Nonius FR 591* was available to be used in the phase-contrast imaging setup and identified to be an optimal solution for this purpose. It is equipped with a molybdenum anode and can be operated at voltages up to 60 kV and a maximal power of 4.8 kW. The X-ray spectrum of the source running at a voltage of 35 kV was measured by an energy-resolving detector and is shown in Figure 4.1. The red spectrum was filtered by silicon to reproduce the attenuation of the grating wafers. The blue spectrum was additionally filtered by 3 cm of water to demonstrate the influence of a tissue sample. In both cases, the energies in the range of 20 to 30 keV are well represented. The relevant characteristic energies of molybdenum are at 17.5 keV and 19.6 keV.

4.3 Detector

Aside from the X-ray source, the detector is an essential component of every X-ray imaging device. Different types and working principles exist to register impinging photons. In digital medical imaging systems, scintillator-based X-ray detectors are usually used. Thereby, the X-rays are first converted into visible light, which can then be detected by charge coupled devices (CCDs) or complementary metal-oxide semiconductors (CMOS) sensors. The electrical charge

created in the sensor is then summed up over a certain integration time, which is referred to as exposure time. Lower energy photons contribute less to the integrated signal than higher energy photons, because the amount of charge carriers is proportional to the energy of an X-ray photon. Thus, the contribution of lower energies, which result in larger refraction angles, is underestimated and the overall phase sensitivity is reduced. A further drawback is that thermally generated charge carriers, commonly known as dark current, are accumulated as well and manifest in additional noise. This is in particular problematic in cases of low X-ray flux and low-energy photons. Another source of noise is electronic noise, which arises during signal amplification and readout.

New developments in X-ray detector technology include the ability to process and count each individual X-ray photon. The *PILATUS* system from *Dectris* is one of these novel single-photon counting detectors. It is a hybrid-pixel detector, which is composed of a silicon sensor connected to an array of readout channels. The charge that is generated by an incoming photon in the sensor material of a certain pixel gets amplified and a digital signal is produced, if the charge exceeds a pre-defined threshold (Broennimann et al. 2006). The number of such signals corresponds to the number of photons registered by the pixel. Each photon contributes equally regardless of its energy, because the X-ray photons are counted. Compared to charge-integrating detectors, low-energy photons are therefore not underestimated. The threshold further allows to define a minimum energy of the photons in order to be detected. This feature and the direct conversion of the individual X-rays eliminate all sources of classical detector noise. By that, the resulting image noise, in principle, is reduced to the theoretical limit given by the Poisson counting statistics.

The point spread function characterizes the spatial response of an imaging system. It describes the degree of blurring in the final image and should ideally resemble a box function. Contrarily to CCD- or CMOS-based imaging systems, this nearly applies to the *PILATUS* detectors. As a result, edges and small features can be clearly and sharply reproduced in images that are obtained therewith. The effect particularly matters with regard to differential phase-contrast images, which exhibit more edge contrast than the conventional absorption images (Bech et al. 2008).

The *PILATUS II 100k* was chosen for the setup. It consists of 487×195 pixels, with a pixel size of $0.172 \times 0.172\,\mathrm{mm}^2$, and a resulting active area of about $8.4 \times 3.4\,\mathrm{cm}^2$ (width×height). The pixels are evenly distributed over 16 chips (8×2), while the readout electronics cause small gaps between the chips. At these positions, virtual pixels are created by interpolation of the values that are measured by the adjoining pixels. The readout time of the system is in the range of milliseconds.

A drawback of the *PILATUS II 100k* is the low quantum-detecting efficiency of the 450 µm-thick silicon sensor for photons with energies above 20 keV. The

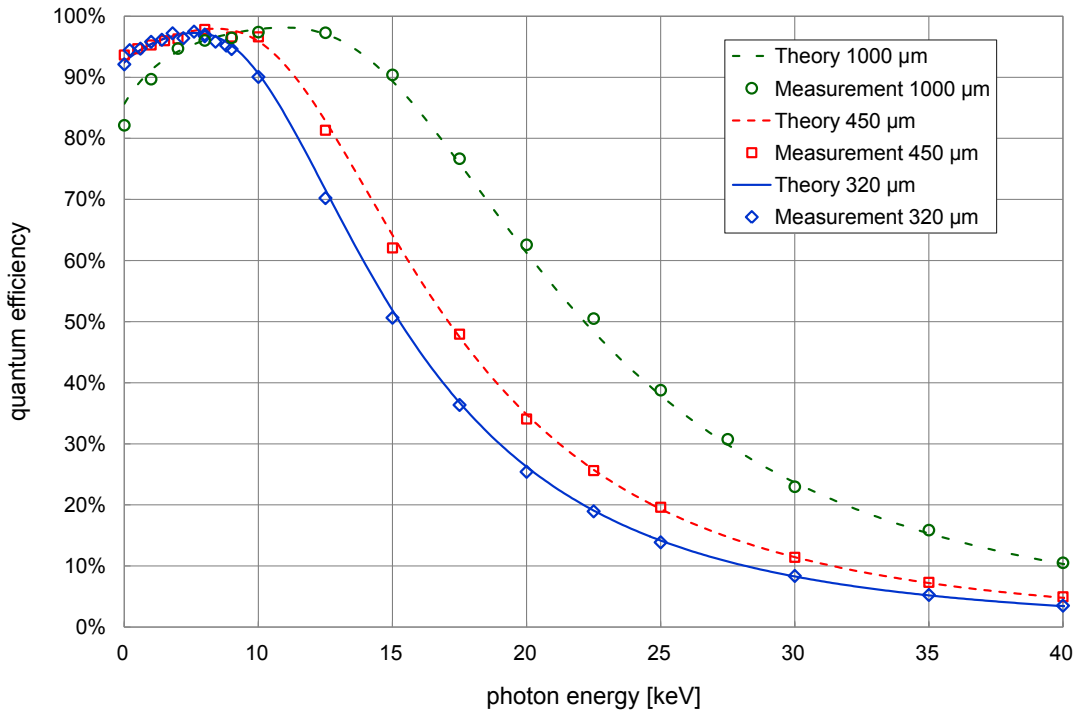

Figure 4.2: The quantum-detecting efficiency of the photon-counting hybrid-pixel detector *PILATUS II 100k* from *Dectris* for different thicknesses of the incorporated silicon sensor. The initial sensor of 450 µm was replaced by a 1 mm thick sensor during the course of this thesis. [Figure kindly provided by *Dectris*.]

quantum-detecting efficiency of the detector describes the probability of a photon to be absorbed in the sensor material. As shown in Figure 4.2, only 20 % of all photons with an energy of 25 keV are detected by a 450 µm-thick silicon sensor. Because a better quantum-detecting efficiency leads to a higher number of total counts and less noise, the initial silicon sensor of the *PILATUS II 100k* was exchanged by a 1 mm-thick sensor. By doing so, the quantum-detecting efficiency in the energy range of 20 keV to 30 keV could be doubled as illustrated in Figure 4.2. Alternative sensor materials like CdTe and GaAs are currently investigated and have the potential to further enhance the quantum-detecting efficiency in near future (Gkoumas et al. 2016).

4.4 Gratings

The most important components of a grating interferometer are the gratings themselves. These optical elements can be divided into two types. On the one hand side the phase grating G1, which is used as beam splitter grating to create the interference pattern. On the other hand side the highly absorbing gratings,

which are used as source grating G0 and analyzer grating G2. The phase grating is made of nickel, silicon, or gold. The height of the grating structures is only a few microns depending on the chosen material and the design energy of the setup. The grating structures of G0 and G2 are typically made of gold. They are substantially higher than those of the phase grating to provide an adequate attenuation of the X-rays.
For the monochromatic case and odd fractional Talbot distances, the visibility of a Talbot-Lau interferometer V can be described by

$$V = \frac{4}{\pi} \cdot V^*_{\mathrm{G0}} \cdot V^*_{\mathrm{G2}} \tag{4.12}$$

with

$$V^*_{\mathrm{G0,G2}} = \frac{\kappa_{0,2}\,(1-\tau_{0,2})\,sinc\,(\kappa_{0,2})}{\tau_{0,2}+\kappa_{0,2}\,(1-\tau_{0,2})}, \tag{4.13}$$

where $\tau_{0,2}$ describe the transmission through the gratings bars and $\kappa_{0,2}$ are the duty cycles of the source and analyzer grating, respectively (Thüring & Stampanoni 2014a). If the gratings have duty cycles of $\kappa_0 = \kappa_2 = 0.5$ and achieve ideal attenuation ($\tau_0 = \tau_2 = 0$), a visibility of

$$V = 2\left(\frac{2}{\pi}\right)^3 = 0.516 \tag{4.14}$$

can be realized. Transmission through the grating bars leads to reduced visibility values. Gold grating structures with a height of 30 µm absorb nearly 100 % of the photons with an energy of $E = 20\,\mathrm{keV}$, but 50 % of the photons with an energy of $E = 40\,\mathrm{keV}$ pass through the grating bars. To assure an attenuation of 95 % for 40 keV, a grating height of 120 µm is required. The small grating periods of a few microns in combination with the enormous aspect ratios (height-to-width ratio of a grating bar) on the order of 50 to 100 demand to push the limits of today's micro-fabrication technologies.
A close collaboration with the *Karlsruhe Institute of Technology* and *microworks GmbH* was established to receive appropriate gratings and to support the progress in grating manufacturing by extensive characterization and continuous exchange. The gratings are fabricated employing the LIGA-process (Kenntner 2013), which is illustrated in Figure 4.3 and briefly described in the following. First, a silicon wafer is covered with the negative resist SU-8 (a) and is exposed by X-rays (b). By doing so, a mask, which has been written before using an electron beam writer, is placed in front of the wafer and prevents certain areas to be exposed. In the next step, these structures are removed by developing the substrate (c) and the gaps are finally filled with the actual grating material like nickel or gold during an electroplating process (d). Facing high aspect ratios, the SU-8 structures tend to collapse due to capillary forces. They are therefore stabilized by keeping bridges at regular distances in between one another (e.g., a bridge of 3 µm is

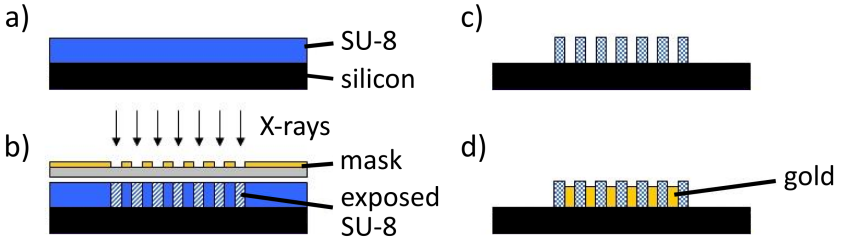

Figure 4.3: Illustration of the grating fabrication process. a) Silicon wafer covered with the resist SU-8. b) Exposure with X-rays. c) Removal of the unexposed SU-8. d) Gaps filled by electroplating.

positioned every 30 µm). As a consequence, the grating bars have small gaps, which result in a lower visibility of the grating interferometer. A SU-8 resist that was prepared with this so-called *bridge design* and the grating structures after electroplating are displayed in Figures 4.4a and 4.4b, respectively. Despite the presence of bridges, capillary effects can cause wavy grating structures, which further affect the visibility. Another reason for potential grating deformations can be stress within the SU-8 matrix (Kenntner et al. 2012).
The gratings that have been employed in the installed phase-contrast imaging system changed over the years and the performance of the Talbot-Lau interferometer could be gradually enhanced by advances in grating manufacturing. The height of the grating structures of G0 and G2 were increased from about 50 µm to 70 µm to provide a nearly ideal attenuation of $\tau < 0.02$ for energies below 30 keV. At the same time, the quality and homogeneity of the grating structures could be clearly improved. A new approach in the fabrication process enabled to remove the gaps within the grating bars caused by the bridges in the SU-8 resist. Instead of bridges, thin stabilizing rods traversing the SU-8 structures are induced by a second exposure before developing the substrate (Kenntner 2013). This kind of resist architecture is named *sunray design* and is shown in Figure 4.4c. The resulting grating bars (Figure 4.4d) feature little holes, but do not have any gaps, which degrade the image quality (Trimborn et al. 2016).
According to Equation 4.13, a gain in visibility can be further obtained by increasing the duty cycles of G0 and G2. Because higher duty cycles simultaneously decrease the photon flux, the best results are achieved for $\kappa_0 = \kappa_2 = 2/3$ (Chabior et al. 2012b). The silicon wafer that carries the grating structures does not affect the visibility, but unnecessarily cuts down on X-ray photons. For this reason, the thickness of the wafer was reduced from 525 µm to 200 µm. Since very thin silicon wafers can break easily, new wafer types made of low absorbing materials are currently under investigation (Koch et al. 2015).
For their installation in the imaging system, the gratings are clamped on holders, which are attached to motorized goniometers. The latter allow to tilt the gratings

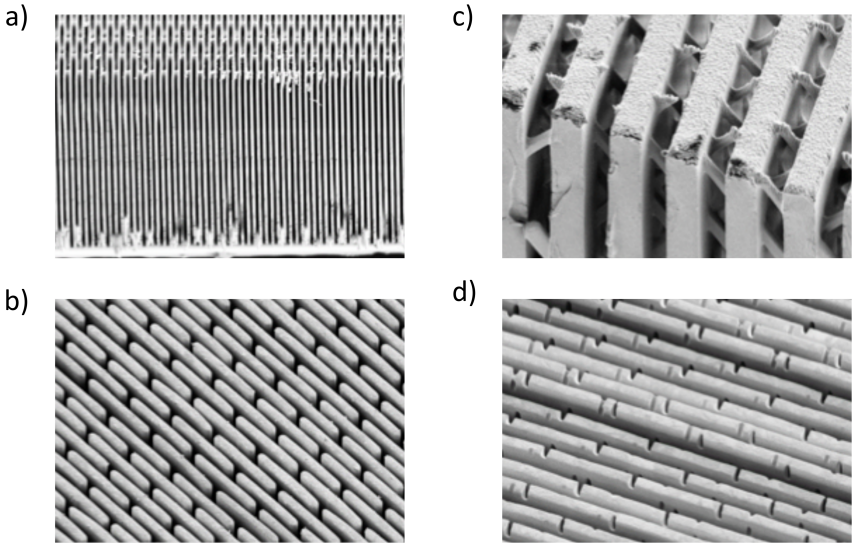

Figure 4.4: The exposed and developed photo-resist in *bridge design* (a) and *sunray design* (c) before filling by electroplating. The resulting grating structures of the *bridge design* (b) exhibit small gaps along the bars which can be avoided by applying the *sunray design* (d). [Images kindly provided by the *Karlsuhe Institute of Technology*.]

with respect to the optical axis for alignment purposes. The stepping process is performed with a mechanical nano-converter designed by the *Paul Scherrer Institute* and driven by a precision motorized actuator. The software package *SPEC* from *Certified Scientific Software* is used to coordinate the motor movements and the data acquisition.

4.5 Configuration

The effective spot size of the rotating-anode X-ray tube *Enraf Nonius FR 591* is $0.3\times0.3\,\mathrm{mm}^2$. This requires the use of a source grating for a functioning interferometer. Summarizing from Chapter 3, the periods p_0, p_1, and p_2 of the three gratings of a Talbot-Lau interferometer have to fulfill the following conditions

$$p_2 = M p_\mathrm{e} = \frac{L+d}{L} p_\mathrm{e} \tag{4.15}$$

with

$$p_\mathrm{e}\,(\pi) = p_1/2 \quad \& \quad p_\mathrm{e}\,(\pi/2) = p_1 \tag{4.16}$$

and

$$p_0 = \frac{L}{d} p_2. \tag{4.17}$$

As a reminder, L is the distance from G0 to G1 and d is the distance from G1 to G2. The three gratings can be arranged in three different ways (Donath et al. 2009). The symmetric geometry ($L = d$) gives the shortest possible interferometer that can be realized for a given period p_1. The conventional and inverse geometry denote the non-symmetric solutions with $L > d$ and $L < d$, respectively. Depending on the purpose of the imaging system, the one or the other configuration might be the best choice.
A large distance d and a small analyzer grating period p_2 are preferable to maximize the sensitivity of the interferometer according to Equation 4.8:

$$\alpha_{\mathrm{r,min}} \equiv \sigma_{\alpha_\mathrm{r}} = \frac{p_2}{2\pi d}\frac{2}{V\sqrt{N}}. \tag{4.18}$$

However, the photon flux decreases with larger distances s from the source. The total number of counts N that are registered by the detector during the stepping procedure can be expressed by

$$N = I_0 D \frac{a^2}{s^2} t, \tag{4.19}$$

where I_0 is the initial X-ray flux and D accounts for any loss of photons due to a limited quantum-detecting efficiency of the detector and due to the attenuation by the grating wafers. The parameter a is the pixel size of the detector and t is the total exposure time over all acquired images. Inserting Equation 4.19 into Equation 4.18 gives the time-dependent minimal refraction angle

$$\alpha_{\mathrm{r,min}}\,(t) = \frac{p_2 s}{2\pi d}\frac{2}{V\sqrt{I_0 D t a}} \tag{4.20}$$

as introduced by Thüring & Stampanoni (2014a). If there are no spacings between the source and G0 and between G2 and the detector ($s = L + d$), the term $p_2 s/d$ can be rewritten to $p_0 + p_2$, which results in

$$\alpha_{\mathrm{r,min}}\,(t) = \frac{p_0 + p_2}{2\pi}\frac{2}{V\sqrt{I_0 D t a}}. \tag{4.21}$$

In this case, a higher signal due to a larger propagation distance d is exactly compensated by the reduced photon flux at the detector. The sensitivity is then optimized by the smallest sum of the grating periods p_0 and p_2. For a given phase grating period p_1, this is achieved for $p_0 = p_2$ and a symmetric setup configuration.
Although the total setup length s does not affect the sensitivity, a longer arrangement can be beneficial for several reasons. The high aspect ratios of G0 and G2 can cause strong shadowing effects, if the beam divergence becomes too large (Thüring et al. 2011). As a consequence, compact setups suffer from a limited

FOV or demand the operation of bent gratings, which are more complicated to produce and hinder the system's flexibility. In addition, a position dependence of the measured signal has to be taken into account for samples that are thick in relation to the setup dimension (Chabior et al. 2012a).
The previous considerations in this section were all based on the assumption that the X-ray source and the detector can be placed directly in front of G0 and behind G2, respectively. This cannot always be realized. A proper shielding of the rotating-anode X-ray tube required to install the discussed interferometer about 0.5 m away in a neighboring hutch. An extra spacing of a few centimeters between G2 and the detector was unavoidable due to the grating holder and its motorized goniometer. An increase of the propagation distance d then slightly outweighs the involved loss of photon flux. The symmetric geometry is still the most sensitive scenario, but the realization of a good visibility becomes more difficult for larger distances between the gratings when dealing with polychromatic X-ray sources.

4.6 Optimization

In order to set up a grating interferometer that features a high visibility at a polychromatic X-ray source, material and height of the phase grating, and the position of the analyzer grating have to be optimized with respect to the energy spectrum. First, one has to decide whether a π- or $\pi/2$-shifting setup should be installed. Then, the grating periods can be chosen according to $p_0 = p_1 = p_2$ for a π-shifting and $p_0 = 2p_1 = p_2$ for a $\pi/2$-shifting configuration. The material and height of the phase grating have to be specified next and require to define a design energy of the interferometer. Afterwards, the distances between the gratings that give the best performance have to be found.
First studies demonstrated that the propagation distance d is not in general limited by the width of the energy spectrum (Weitkamp et al. 2006, Engelhardt et al. 2008). Later, theoretical and experimental investigations revealed that a π-shifting phase grating is preferable, when aiming to build longer setups (Willner 2011, Hipp 2013, Thüring & Stampanoni 2014a). As it was shown in Figure 3.1, the intensity patterns behind a π-shifting phase grating are always at the same vertical position. The intensity patterns behind a $\pi/2$-shifting phase grating, on the other hand, can be shifted by half a period relative to each other. This effect was additionally indicated by the labeling in the corresponding *visibility carpet* of the $\pi/2$-shifting setup that was presented in Figure 3.6. For longer arrangements and a broad spectral width, the line in the *visibility carpet* that is representing the energy spectrum can cross several visibility peaks and the contributions of single energies to the overall visibility can cancel out. In case of the π-shifting setup, the overall visibility is only reduced to some extent due to monoenergetic contributions of low or zero visibility, but no annihilation takes place. An experimental verification of this effect is illustrated in Figure 4.5. A series of

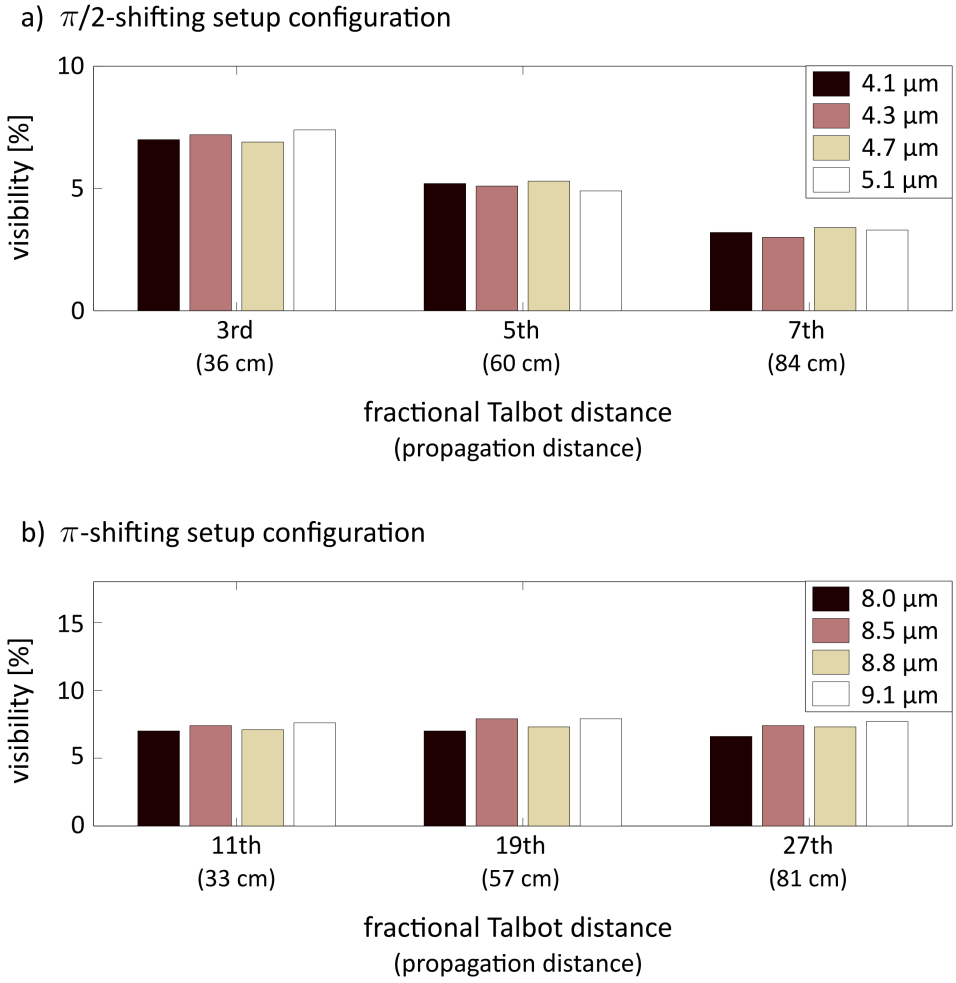

Figure 4.5: Comparison of $\pi/2$-shifting and π-shifting setup configurations with increasing propagation distances and different phase gratings. Whereas the visibility decreases in the $\pi/2$-shifting setup (a), the visibility of the π-shifting setup (b) remains constant. [Figure adapted from Hipp et al. (2014).]

measurements was performed with 2.4 µm-periodic phase gratings. The source and analyzer gratings had either periods of 2.4 µm (π-shifting setup) or periods of 4.8 µm ($\pi/2$-shifting setup). Whereas the overall visibility of the $\pi/2$-shifting setup decreased with increasing propagation distance (36 cm, 60 cm, and 84 cm), the visibility of the π-shifting setup remained nearly constant at all distances (33 cm, 57 cm, and 81 cm).
The periods of the three gratings within a π-shifting symmetric setup configuration are all identical ($p_0 = p_1 = p_2$). The smaller the grating periods, the more sensitive the interferometer. Although gratings with periods down to 2.4 µm are fabricated, gratings with periods of 5.4 µm are employed in the installed phase-

contrast imaging system. This relaxes the manufacturing process of larger grating areas and enables a better grating quality in terms of more homogeneous structures or gratings in the *sunray design*. The design energy of the setup, which is defined by the material and height of the phase grating and the distances between the gratings, changed over time. Within the scope of the master thesis *Highly sensitive grating interferometry using a polychromatic X-ray source* by Hipp (2013), several studies including energy-resolved visibility measurements were performed to better understand and optimize the Talbot-Lau interferometer.
In the beginning, phase gratings for design energies of around 23 keV were utilized. Later, they were outperformed by phase gratings that introduce a phase shift of π to an X-ray energy of about 27 keV. The phase gratings were either made of nickel or gold. The distances between the gratings varied between 80 cm and 90 cm. Most of the times, the position of the analyzer grating did not equal an odd fractional Talbot distance of the design energy, which was predefined by the respective phase grating. In addition, an immense influence of the phase grating duty cycle κ_1 on the setup design could be observed. Deviations of the duty cycle from $\kappa_1 = 0.5$ can strongly deform the resulting *visibility carpet* and even lead to annihilation as it is the case for the $\pi/2$-shifting setup configuration (Hipp et al. 2014). There are always tolerances in the grating fabrication, so that an experimental optimization of a grating-based phase-contrast imaging setup, in addition to any theoretical considerations, is highly recommended.

4.7 Performance

In summary, the phase-contrast imaging system that was designed during this thesis combines a rotating-anode X-ray tube (*Enraf Nonius FR 591*), a photon-counting hybrid-pixel imaging detector (*PILATUS II 100k* from *Dectris*), and a Talbot-Lau interferometer. A photograph of the setup is presented in Figure 4.6. The interferometer consists of three gratings with periods of 5.4 µm, which are installed in equal distances from each other (symmetric geometry). It is operated in a π-shifting setup configuration and has a design energy between 20 keV and 30 keV depending on the height of the phase grating that is utilized.
As mentioned in the previous sections, the experimental system underwent several modifications over time. These include the employment of various gratings, which were all fabricated by the *Karlsruhe Institute of Technology* or *microworks GmbH* and constantly advanced in quality. The distances between the gratings were optimized to increase the visibility of the interferometer. In addition, the quantum-detecting efficiency of the *PILATUS II 100k* was improved by changing the thickness of the incorporated silicon sensor from 450 µm to 1 mm to increase photon statistics. Several biomedical studies were conducted with varying setup parameters. The different settings are listed in Table 4.1 at the end of this Chapter.

The sensitivity of the latest setup configuration (setting H) was measured as a function of the exposure time for an evaluation of the system's performance (Birnbacher et al. 2016). In this study, 11 images were recorded at a tube voltage of 40 kV during each stepping procedure and the acquisition time per image was gradually increased for each stepping scan. The standard deviations of the relative phase $\sigma_{\Delta\phi_1}$ were then determined in areas of 190×190 pixels within the processed images and converted into minimum resolvable refraction angles following Equation 4.2. A second measurement series was performed after inserting a water bath of 4 cm thickness in the beam to simulate the attenuation caused by respective soft-tissue samples. The resulting refraction angles of both experiments are plotted over the total number of counts registered by the detector in Figure 4.7. In addition, corresponding theoretical values were calculated according to Equation 4.8. The interferometer visibility V of 38.7 % that is achieved by the setup configuration H was used for the calculations.
Experimental and theoretical values are well in line. This is due to the absence of any read-out noise when using the photon-counting detector *PILATUS II 100k*. The longer the exposure time, the higher is the number of total counts and the achievable sensitivity. At some point, the experimentally evaluated minimum detectable refraction angles diverge from theory and increase again. The reason for

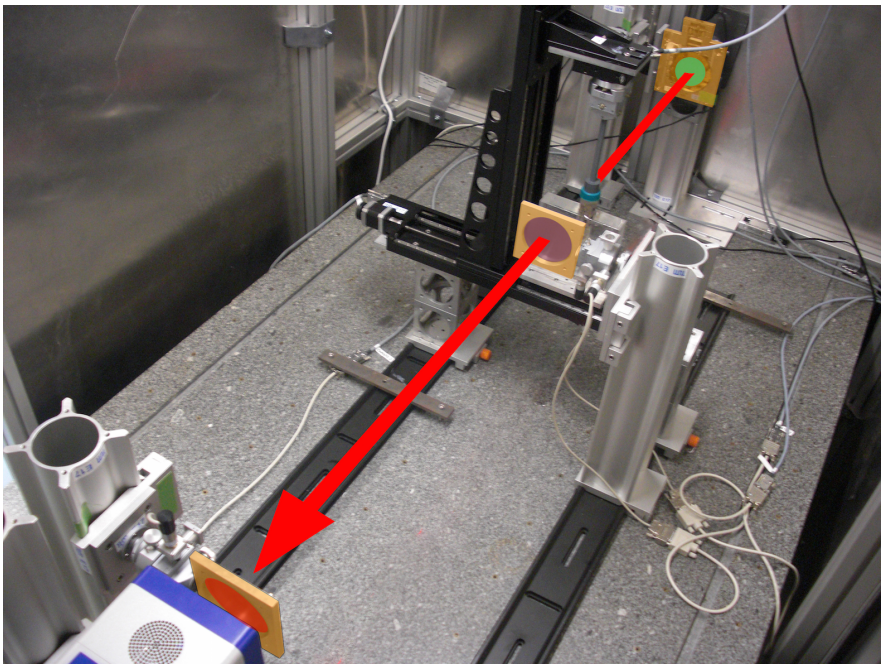

Figure 4.6: Photograph of the experimental phase-contrast imaging setup. The X-ray source *Enraf Nonius FR 591* is located in the neighboring hutch. The X-ray beam indicated by the red arrow traverses the three colored gratings and then hits the photon-counting detector *PILATUS II 100k*.

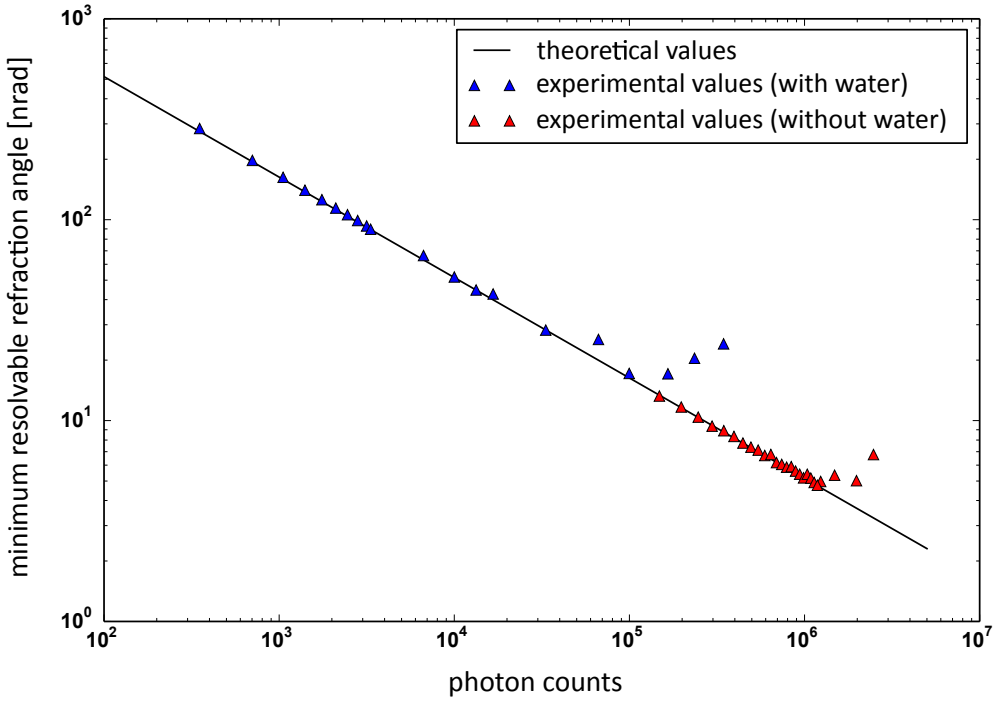

Figure 4.7: Log-log plot of the minimum resolvable refraction angle over the total number of photon counts obtained by increasing the exposure times (red data points). The blue data points were measured with an additional water container in the beam to simulate the attenuation caused by soft-tissue samples. The black line represents calculated values based on Equation 4.8. [Figure adapted from Birnbacher et al. (2016).]

this behavior are thermal drifts of the gratings and other instabilities that become noticeable at very long exposure times. The best sensitivity in both series of measurements was attained for a total exposure time of $11 \times 25\,\mathrm{s} = 275\,\mathrm{s}$. Without water bath, the minimum resolvable refraction angle accounted for 5 nrad. With water bath, the photon flux is reduced by a factor of ten and the minimum refraction angle was determined to be 17 nrad. At a shorter exposure time of $11 \times 5\,\mathrm{s} = 55\,\mathrm{s}$, which is a more realistic scenario for tomographic imaging, sensitivity values of 10 nrad and 38 nrad, respectively, could be achieved.
These results keep up with numbers reported from grating-based phase-contrast setups at synchrotron radiation facilities. A sensitivity of 67 nrad was measured at the grating interferometer integrated into *TOMCAT*, a beamline at the *Swiss Light Source* (McDonald et al. 2009, Modregger et al. 2011). This value was obtained at an X-ray energy of 25 keV, a total exposure time of $6 \times 0.35\,\mathrm{s} = 2.1\,\mathrm{s}$, and a detector pixel size of 48 µm. At the beamline *ID19* of the *European Synchrotron Radiation Facility* (ESRF), a sensitivity of 14 nrad was achieved in the same energy range and with a pixel size of 28 µm by applying a total exposure

time of $8 \times 0.4\,\mathrm{s} = 3.2\,\mathrm{s}$ (Pfeiffer et al. 2007a). The laboratory phase-contrast imaging system that was installed during this thesis, however, cannot compete with both synchrotron setups in terms of spatial resolution and scanning time. A comparable lab-based Talbot-Lau interferometer was built for a design energy of 28 keV and consists of three 2.4 µm-periodic gratings that are positioned in a symmetric geometry (Thüring et al. 2011). The setup is relatively compact (up to 325 mm in total length) and features bent gratings to avoid shadowing effects. The incorporated detector has a pixel size of 48 µm which enables a higher spatial resolution compared to the *PILATUS II 100k* with its pixel size of 172 µm. The system can resolve refraction angles down to 200–300 nrad at a total exposure time of $16 \times 8\,\mathrm{s} = 128\,\mathrm{s}$ (Thüring et al. 2012, 2013a). Thus, the experimental setup described in this chapter offers a significantly better sensitivity and enables high-contrast phase-contrast imaging of biomedical samples at a laboratory X-ray source in a quality that has only been possible at synchrotron radiation facilities before.

Table 4.1: List of technical parameters of the different setup configurations that the laboratory phase-contrast imaging setup underwent during this thesis.

	G0 height (material)	G1 height (material)	G2 height (material)	distance G0-G1	distance G1-G2	Si-sensor thickness
A	55 µm (gold)	8.5 µm (nickel)	55 µm (gold)	87.5 cm	87.5 cm	450 µm
B	55 µm (gold)	8.5 µm (nickel)	55 µm (gold)	87.5 cm	87.5 cm	1 mm
C	55 µm (gold)	8.5 µm (nickel)	55 µm (gold)	80 cm	80 cm	1 mm
D	55 µm (gold)	8.5 µm (nickel)	65 µm (gold)	80 cm	80 cm	1 mm
E	55 µm (gold)	9.5 µm (nickel)	65 µm (gold)	80 cm	80 cm	1 mm
F	55 µm (gold)	8.5 µm (nickel)	65 µm (gold)	80 cm	80 cm	1 mm
G	70 µm (gold)	5.2 µm (gold)	65 µm (gold)	85.7 cm	85.7 cm	1 mm
H	70 µm (gold)	5.2 µm (gold)	70 µm (gold)	85.7 cm	85.7 cm	1 mm

Chapter 5

Phase-contrast computed tomography

5.1 Tomographic imaging

So far, only radiographic imaging was discussed. The X-rays penetrate the object from one direction and project all inner structures onto the detector, so that they overlay each other in the final images. This is sufficient for screening purposes like clinical mammography, but in many cases a 3D representation of the sample needs to be generated for examination. In a tomographic scan, many radiographic projection images are taken from different angles θ by rotating the sample around its axis or the whole imaging system around the sample as it is done in medical CT systems (Hounsfield 1973). The 3D object can then be reconstructed from the acquired data (Kak & Slaney 2001). The same procedure can be applied, when using a grating interferometer. Thereby, quantitative information on the linear attenuation coefficient $\mu(x_i, y_i, z_i)$ and the refractive index decrement $\delta(x_i, y_i, z_i)$ of every volume element (x_i, y_i, z_i), called voxel, can be retrieved (Herzen et al. 2009).
There are several ways to obtain the information of the individual voxels from the values that are measured in the radiographic images. A fast and accurate solution for data recorded with sufficient and regular angular sampling is the filtered back-projection (FBP) algorithm. Assuming the function $f(x, y, z)$ to represent the 3D distribution of a physical quantity within an object, which is rotated around the y-axis during the tomographic scan, then the projection $P(x', \theta)$ of one slice $f(x, z)$ at one of the angles θ can be expressed by

$$P(x', \theta) = \int f(x, z)\, dz' = \int f(x' \cos\theta - z' \sin\theta, x' \sin\theta + z' \cos\theta)\, dz', \quad (5.1)$$

where the coordinate systems (x', z') and (x, z) are rotated by the angle θ with respect to each other. According to the Fourier slice theorem, the one-dimensional

Fourier transform of $P(x', \theta)$ represents a line (through the origin and tilted by the angle θ) within the 2D Fourier transform of the slice $f(x, z)$

$$\mathcal{FT}\left[P(x', \theta)\right] = \widetilde{P}(u', \theta) = \widetilde{f}(u', \theta), \tag{5.2}$$

with u' being the reciprocal space coordinate of x' (Kak & Slaney 2001). As direct consequence of this relation, the original object function can be reconstructed by applying the FBP

$$f(x, z) = \int_0^{\pi} \mathcal{FT}^{-1}\left[\widetilde{P}(u', \theta)\,\widetilde{F}(u')\right] d\theta, \tag{5.3}$$

where $\mathcal{FT}^{-1}$ is the inverse Fourier transform and $\widetilde{F}(u')$ is a filter function that is operated on the measured projections in Fourier space. The filtering step becomes necessary as the sampling is discrete and done in a polar coordinate system. For this reason, interpolation is needed when the data is backprojected to the Cartesian grid for the reconstruction of the object in real space. Most commonly, the so-called ramp or Ram-Lak filter $\widetilde{F}(u') = |u'|$ is used. It accounts for the denser sampling towards the origin in Fourier space by weighting the high-frequency components stronger than the low-frequency components. A detailed mathematical description of CT can be found in *Principles of Computerized Tomographic Imaging* by Kak & Slaney (2001).
A modification of the acquired radiographic images is needed before reconstruction in order to retrieve quantitative information. This process differs for attenuation contrast and phase contrast as briefly discussed in the following. In attenuation contrast, the content of a processed radiographic image (Equation 3.12) is connected to the Beer-Lambert law (Equation 3.11) by

$$T(x, y) = e^{-\int \mu(x,y,z)dz}. \tag{5.4}$$

Thus, the negative natural logarithm of the transmission image is taken as input for the FBP

$$P_{\mu}(x, \theta) = -\ln T(x', \theta) = \int \mu(x, z)\, dz'. \tag{5.5}$$

The reconstructed slices then represent the linear attenuation coefficient $\mu(x, z)$. In phase contrast, the differences in the relative phases $\Delta\phi_1(x, y)$ are extracted from the recorded stepping curves. These values can be associated to the refraction angles $\alpha_{\mathrm{r}}(x, y)$ (Equation 3.10) and further to the differential phase shift $\partial\Phi(x, y)/\partial x$ introduced by the sample (Equations 2.13 and 2.17) via

$$\Delta\phi_1(x, y) = \frac{2\pi d}{p_2}\alpha_{\mathrm{r}}(x, y) = \frac{2\pi d}{p_2}\frac{1}{\partial x}\int \delta(x, y, z)\, dz. \tag{5.6}$$

As a consequence, the factor $p_2/2\pi d$ is taken into account during data processing

$$P_{\delta}(x, \theta) = \frac{p_2}{2\pi d}\Delta\phi_1(x', \theta) = \frac{1}{\partial x'}\int \delta(x, z)\, dz'. \tag{5.7}$$

Additionally, an integration step has to be performed, because the modified image is not a projection of $\delta(x,z)$, but a projection of its derivative in the direction perpendicular to the grating lines. The integration can be done either for each single radiographic image or during reconstruction by simply changing the filter function (Pfeiffer et al. 2007b). According to the Fourier theorem for derivatives

$$\mathcal{FT}\left[\frac{\partial f(x)}{x}\right] = 2\pi i u \widetilde{f}(u), \tag{5.8}$$

the integration can be operated in Fourier space by replacing the original ramp filter $\widetilde{F}(u') = |u'|$ by the imaginary Hilbert filter

$$\widetilde{H}(u') = \frac{|u'|}{2\pi i u'} = \frac{1}{2\pi i \mathrm{sgn}(u')}, \tag{5.9}$$

where $\mathrm{sgn}(u')$ is the sign function.
For monochromatic radiation and known X-ray energy E, the electron-density distribution $\rho_\mathrm{e}(x,z)$ of the slice can be obtained from the reconstructed refractive index decrement $\delta(x,z)$ by following Equation 2.15

$$\rho_\mathrm{e}(x,z) = \frac{2\pi E^2}{r_0 h^2 c^2}\delta(x,z). \tag{5.10}$$

All the reconstructed slices along the y-axis can be stacked together and then form the 3D volume of the object.

5.2 Scan procedure

The sensitivity of the grating interferometer, as it was derived in the previous chapter, is only valid at the position of the phase grating. Moving the sample away from G1, either towards G0 or to G2, linearly decreases the actual angular sensitivity (Donath et al. 2009). To achieve maximum sensitivity, the rotation stage for tomographic imaging has been installed directly in front of the phase grating. The rotation stage is further mounted on two linear stages. These stages are used to move the sample out of the beam when taking flat-field images and to translate the sample along the rotation axis if several sections need to be imaged. Due to the dimensions of the motors and the grating holder, a gap of a few centimeters between sample and G1 was unavoidable. The exact positions of the sample stage and the detector were chosen to constitute a geometrical object magnification of

$$M_\mathrm{obj} = \frac{x_\mathrm{det}}{x_\mathrm{obj}} = 1.72, \tag{5.11}$$

where x_obj and x_det are the distances of the sample and the detector from the X-ray source, respectively. The geometrical magnification and the $172\times172\,\mu\mathrm{m}^2$

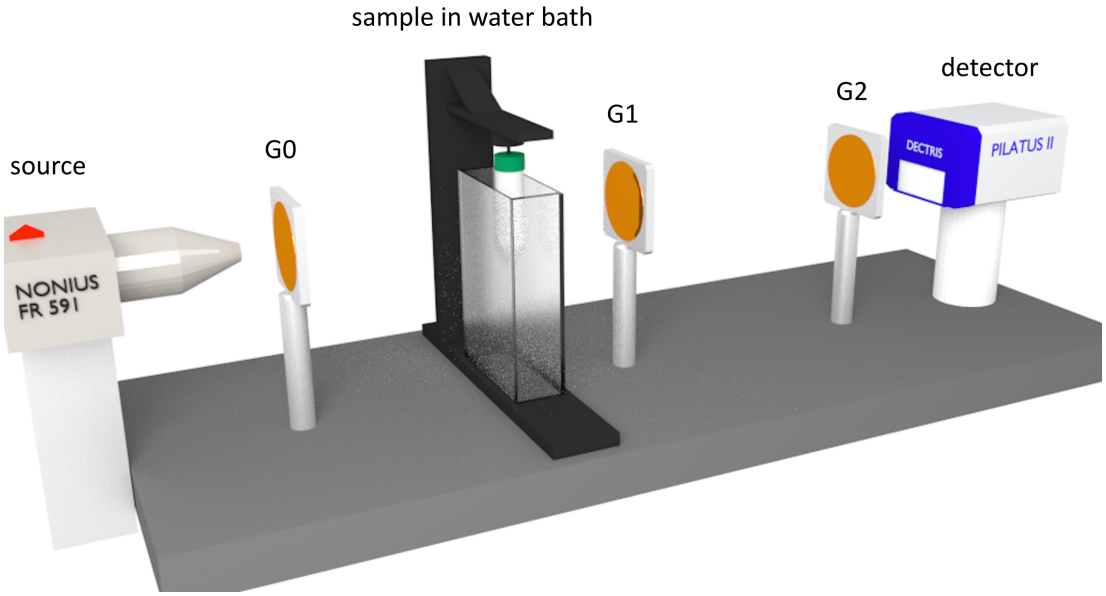

Figure 5.1: Illustration of the experimental phase-contrast CT system. Three gratings with micrometer-sized structures are installed between the rotating-anode X-ray tube (*Enraf Nonius FR 591*) and the photon-counting X-ray detector (*PILATUS II 100k*). The samples are mounted in front of the phase grating G1 and are submerged in a water bath during measurements to avoid image artifacts. [Figure adapted from Willner et al. (2015).]

pixel size of the *PILATUS II 100k* result in an effective pixel size of $100\times100\,\mu m^2$ at the position of the sample. The effective pixel size represents the spatial resolution of the radiographic projection images that are recorded by the setup. This is due to the sufficiently small source size and the box-shaped point spread function of the *PILATUS* (Birnbacher et al. 2016). The detector area of $8.4\times3.4\,cm^2$ and a circular analyzer grating of $\varnothing\,7\,cm$ enable a FOV of up to $4\times2\,cm^2$. A graphical illustration of the setup configuration for phase-contrast CT is shown in Figure 5.1.

Most of the biological soft-tissue samples that are investigated by CT at the imaging system are placed in plastic cylinders of $\varnothing\,3\,cm$. These so-called falcon tubes are mounted underneath the sample rotation stage and are submerged in a water-filled plastic container of about 4 cm thickness throughout the measurements. The use of a water bath is motivated by the large phase differences that would otherwise occur between the walls of the sample cylinder and air. The imaging setup is designed to be very sensitive, so that they would cause strong phase-wrapping artifacts and affect the ability of quantitative imaging (Zanette et al. 2011). In addition, beam hardening effects can be mostly suppressed by the water bath as long as there are no highly absorbing structures within the sam-

ple. Because tissues mainly consist of water, the X-rays then experience similar attenuation along their path regardless of the actual shape of the sample.
Following the noise behavior of the differential phase-contrast projection images, the noise in the reconstructed image data depends on the total number of counts N_{tot} recorded during image acquisition (Chen et al. 2011)

$$N_{\mathrm{tot}} = N_\theta N_{\mathrm{steps}} N_0, \tag{5.12}$$

with N_θ, N_{steps}, and N_0 being the number of projection images, the steps per projection image, and the counts per single image, respectively. This equation indicates that the distribution of the total counts over the number of projections and steps does not matter with regards to the final image quality. However, a few aspects have to be considered. For a correct representation of the reconstructed object using FBP, the sampling of the Fourier space has to be sufficiently dense, even in the more sparsely sampled outer regions. The minimum number of projections that have to be taken in order to fulfill this criterion is given by the Nyquist sampling theorem as

$$N_\theta = \frac{\pi}{2} N_{\mathrm{pix}}, \tag{5.13}$$

where N_{pix} is the number of detector pixels covered by the sample in horizontal direction (Mueller 1998). Consequently, at least 500 projections should be acquired during the CT scan of samples within the $\varnothing\,3\,\mathrm{cm}$ falcon tubes to avoid undersampling artifacts in the final images. Another limit is defined by the projection images themselves. If the number of counts per projection $N_{\mathrm{proj}} = N_{\mathrm{steps}} N_0$ becomes too low, statistical phase wrapping (Equation 4.4) occurs and no phase information can be extracted (Raupach & Flohr 2011). The third constraint concerns the number of steps per projection N_{steps}. Minimum three images have to be acquired during the stepping procedure in order to determine the position of the interference pattern with respect to the grating bars and, thus, to capture the relative phase ϕ_1 (Weitkamp et al. 2005). Due to the discrete sampling of the periodic stepping curve, higher-order terms can cause systematic errors (Yashiro et al. 2008). This effect vanishes if seven or more images are taken per projection, while an odd number of steps generates a lower relative error than an even number of steps (Thüring 2013).
During the early periods of experiments at the imaging setup, 1200 projections with 11 steps and 5 s exposure time per image were recorded during CT measurements. Thanks to the consecutive improvements of the imaging setup as presented in Chapter 4, the number of projections and the exposure time could be reduced to 800 and 3 s. Inhomogeneities of the gratings or the detector sensor can lead to ring artifacts in the reconstructed images. In order to mitigate these artifacts, the sample is laterally displaced by an integer number of pixels between each projection. These shifts are then reversed in the subsequent data processing. Through this procedure, the inhomogeneities finally average out in

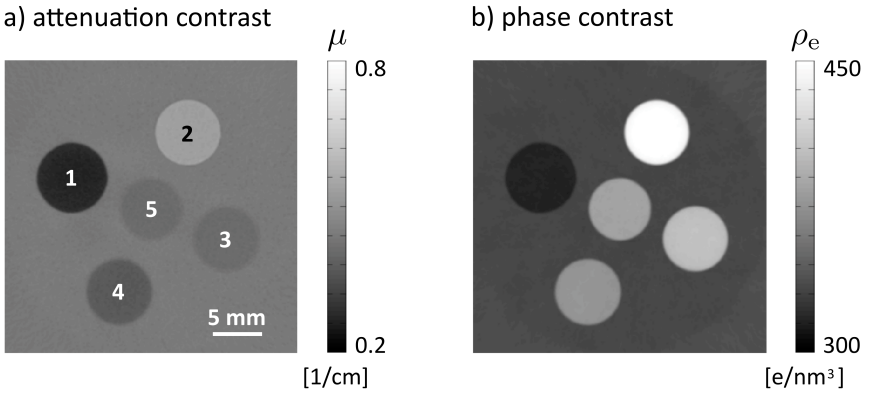

Figure 5.2: Quantitative attenuation-contrast (a) and phase-contrast (b) imaging results of a phantom consisting of five plastic rods (LDPE [1], POM [2], PEEK [3], nylon [4], and PMMA [5]). The rods were submerged in water during the CT measurement.

the reconstruction. Even though the beam divergence in the setup is rather low ($< 1.5°$), the FBP reconstruction algorithm was adapted to divergent beam geometries according to Feldkamp et al. (1984). A detailed description thereof is given by Kak & Slaney (2001).
Exemplary CT imaging results of a phantom in both contrast modes are presented in Figure 5.2. The phantom consists of five different plastic rods ($\varnothing\,6\,\mathrm{mm}$) and was submerged in water. The materials include low-density polyethylene (LDPE), polyoxymethylene (POM), polyetheretherketone (PEEK), nylon, and polymethylmethacrylate (PMMA). The CT scan was performed at 40 kV and with setup configuration F (see Table 4.1). The measurement included 1200 projections, which were recorded with 11 steps and 3 s exposure time per image. The radiographic images $T(x, y, \theta)$ in attenuation contrast were modified before reconstruction as described in Equation 5.5. The voxel values were then divided by the effective pixel size of the system to obtain the linear attenuation coefficient $\mu_\Delta(x_i, y_i, z_i) = \mu(x_i, y_i, z_i) - \mu_{\mathrm{water}}$ (in units of 1/cm) relative to the surrounding water. The phase-contrast projections $P_\delta(x, y, \theta)$ were calculated according to Equation 5.7. The results were additionally multiplied by a factor of $x_{\mathrm{G1}}/x_{\mathrm{obj}}$ to consider the reduced sensitivity, which is caused by the existent distance between the object and the phase grating (Engelhardt et al. 2007). Here, x_{obj} is again the distance of the object from the source and x_{G1} is the distance between the source and G1. After reconstruction via FBP with Hilbert filter, the dimensionless refractive index decrement $\delta_\Delta(x_i, y_i, z_i) = \delta(x_i, y_i, z_i) - \delta_{\mathrm{water}}$ of each voxel relative to the surrounding water is obtained.
To receive the actual distribution of $\mu(x_i, y_i, z_i)$ and $\delta(x_i, y_i, z_i)$ within the sample, the respective energy-dependent μ_{water} and δ_{water} have to be added to the data. These values can be determined by using the PMMA rod as calibration

material and comparing its experimentally evaluated μ_Δ- and δ_Δ-values to theoretical numbers. That way, effective energies $E_{\text{eff},\mu}$ and $E_{\text{eff},\delta}$ can be assigned to the measurement. Using these effective energies, the corresponding linear attenuation coefficient μ_{water} and refractive index decrement δ_{water} of water can be looked up in tabulated data (Chantler et al. 2005, Berger et al. 2010). The effective energy $E_{\text{eff},\delta}$ is further needed to convert the refractive index decrements $\delta(x_i, y_i, z_i)$ into electron densities $\rho_{\text{e}}(x_i, y_i, z_i)$ following Equation 5.10. This calibration procedure can be also applied when imaging biological tissue samples by inserting an PMMA rod into the falcon tubes.
A software tool to establish an easy and fast workflow for data handling at the phase-contrast imaging system was developed by Marschner (2013) during the master thesis *Data processing in grating-based X-ray phase-contrast computed tomography: workflow automation and noise studies*. The package includes the signal extraction from the stepping curves via Fourier analysis or weighted least-square fit and an automatic reversion of the sample shift to avoid ring artifacts. Dead and hot pixels of the X-ray detector are identified and eliminated by interpolation in the raw images before signal extraction. Offsets and gradients within the phase-contrast projections, which can occur due to drifts of the gratings between the flat-field and the sample scan or due to other instabilities, are corrected by applying an adaptive differential phase recovery (Tapfer et al. 2012). Corrupted flat-field and projection images are identified and removed from further data analysis. The center of rotation, an important input parameter for the reconstruction, is determined with sub-pixel accuracy. Different kinds of filter functions can be selected for the FBP algorithm in addition to the typically used Ram-Lak and Hilbert filter. The reconstructed data is displayed within the graphical user interface, where also a 3D region-of-interest (ROI) within the PMMA rod can be quickly defined for calibration. If the required parameters like the effective pixel size, p_2, d, x_{obj} and x_{G1} are correctly stated, the effective energies $E_{\text{eff},\mu}$ and $E_{\text{eff},\delta}$ are evaluated and $\mu(x_i, y_i, z_i)$, $\delta(x_i, y_i, z_i)$, and $\rho_{\text{e}}(x_i, y_i, z_i)$ can be calculated.

5.3 Electron-density resolution

Previous phantom studies that were conducted at the beamline *ID19* of the ESRF demonstrated the high accuracy in the quantitative evaluation of refractive index decrements δ and electron densities ρ_{e}, which can be achieved by grating interferometry using synchrotron radiation (Zanette et al. 2011, Willner et al. 2013). In these studies, the theoretical values are within one standard deviation of the experimental results for most examined materials and substances. This suggests that systematic errors resulting from data processing and uncertainties in the knowledge of the exact propagation distance d or the correct X-ray energy of the monochromator are in the same order of magnitude or even smaller than the actual image noise. Considering the electron-density resolution to be the noise

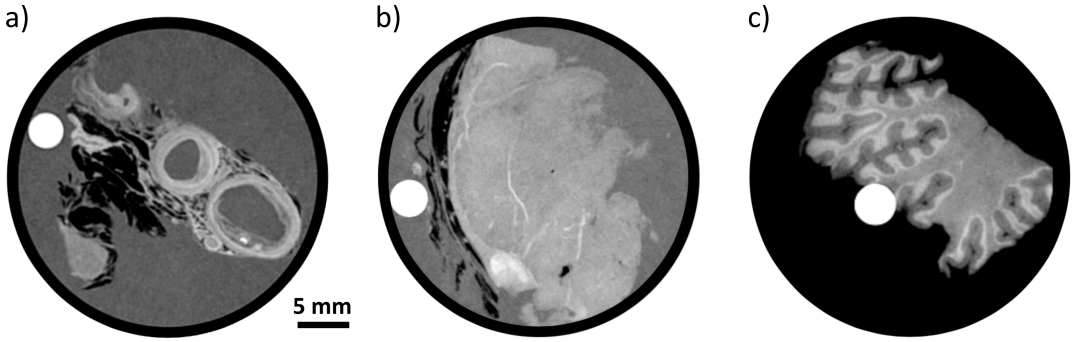

Figure 5.3: Phase-contrast imaging results of different biomedical samples to demonstrate the high soft-tissue contrast. a) Plaque components of carotid arteries (see Chapter 9). b) Fine structure in renal tissue. c) Cerebellum with stratum granulosum. The high-intensity circular areas in the images are the PMMA rods that are used for the calibration of quantitative values.

level within an homogeneous area, a value of 0.18 e/nm^3 was reported for highly sensitive phase-contrast CT at the synchrotron (Pfeiffer et al. 2007a).
In comparison to this benchmarking result, the noise of the phantom measurement shown in Figure 5.2 was around 0.8 e/nm^3. A resolution of 0.45 e/nm^3 was achieved with the latest setup configuration *H* (Birnbacher et al. 2016). This high electron-density sensitivity allows for the visualization of different tissue types and soft-tissue fine structure as demonstrated on the examples of an artery, a kidney, and a cerebellum in Figure 5.3. In the cerebellum sample, a tissue layer called stratum granulosum can be clearly distinguished from grey and white matter, which was previously only realized with synchrotron radiation (Schulz et al. 2010). A spatial resolution of about 170 µm was determined for the reconstructed volume of the cerebellum (Birnbacher et al. 2016). The discrepancy between the effective voxel size ($100\times100\times100$ µm^3) and the actual spatial resolution is due to the reconstruction process and potential imprecisions in the sample positioning.
Noise as measure for the electron-density resolution merely quantifies the relative differences that can be resolved by the laboratory phase-contrast imaging system. In contrast to monochromatic synchrotron measurements, which yield comparably small systematic errors, the accuracy of the retrieved electron-density values might be reduced due to the polychromatic spectrum. Qi et al. (2010) investigated the capabilities of a correct electron-density determination at a polychromatic X-ray source by using water for calibration of the effective energy E_{eff}. The experimental results of their phantom materials are in good agreement with the calculated numbers. The effective energy $E_{\text{eff},\delta}$ in phase contrast depends on various parameters like the tube voltage, beam filtration, and the interferometer design. It can differ greatly from the effective energy $E_{\text{eff},\mu}$ in attenuation contrast by reason of the diverse image formation process (Munro & Olivo 2013).

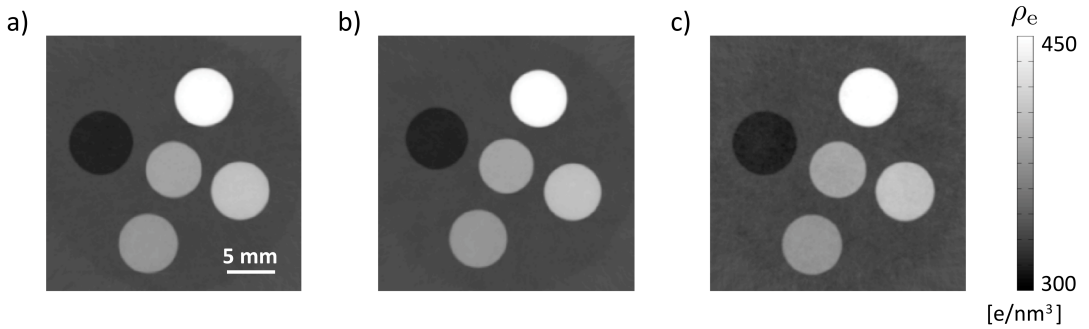

Figure 5.4: Quantitative phase-contrast imaging results of three phantom measurements with different scan parameters to study the accuracy in the determination of electron-density values when using a polychromatic X-ray source. a) Tube voltage of 40 kV ($E_{\text{eff},\delta} = 27.3$ keV). b) Tube voltage of 35 kV ($E_{\text{eff},\delta} = 26.5$ keV). c) Tube voltage of 50 kV with additional aluminum filtering ($E_{\text{eff},\delta} = 31$ keV). The phantom materials are identical to Figure 5.2.

Although there is generally less beam hardening in phase-contrast imaging than in conventional attenuation-based CT (Chabior 2011), it nevertheless can also alter the measured δ-values and impact the recovered electron densities.
In order to study the deviations that arise from the PMMA calibration during the conversion into electron densities, two additional CT scans of the phantom from Section 5.2 have been conducted. One measurement was performed with the X-ray tube being operated at a voltage of 35 kV and the other one at 50 kV with additional aluminum filtering. The employed setup configuration G varied in gratings and distances from the configuration F, which was used before. That way, different source spectra and conditions can be compared concerning their quantitative output. A reconstructed phase-contrast image from each of the three scans is displayed in Figure 5.4. The effective energies $E_{\text{eff},\mu}$ and $E_{\text{eff},\delta}$, which were determined by the PMMA calibration, are listed in Table 5.1. The table further includes the electron densities of the other four materials. They were evaluated in ROIs of 150×30×30 voxels.
As intended, the effective energies ranged from 25 keV to 34.4 keV in attenuation contrast and from 26.5 keV to 31 keV in phase contrast. The noise in the third measurement was 1.9 e/nm^3 and is larger than the 0.8 e/nm^3 of the other two scans. This is due to a decreased visibility at the higher tube voltage. The standard deviations (std) of the electron-density values that were obtained for each of the four materials were 0.51 e/nm^3 (LDPE), 0.26 e/nm^3 (nylon), 0.26 e/nm^3 (PEEK), and 0.76 e/nm^3 (POM). The largest differences Δmax in the values of the electron densities between the three measurements were 1.0 e/nm^3 (LDPE), 0.5 e/nm^3 (nylon), 0.5 e/nm^3 (PEEK), and 1.2 e/nm^3 (POM). This indicates that the accuracy in the determination of electron densities by applying the PMMA

Table 5.1: Scan parameters of the three phantom measurements to investigate the effects of polychromatic radiation on the quantitative imaging results. The mean values of the electron density, the standard deviations (std), and the maximum differences (Δmax) are listed.

	scan 1	scan 2	scan 3	mean	std	Δmax
setup configuration	F	G	G			
voltage [kV] (filter)	40	35	50 (Al)			
$E_{\text{eff},\mu}$ [keV]	27.1	25	34.4			
$E_{\text{eff},\delta}$ [keV]	27.3	26.5	31			
noise [σ_{ρ_e} in e/nm^3]	0.8	0.8	1.9			
LDPE [ρ_e in e/nm^3]	316.5	315.5	316.2	316.1	0.51	1
nylon [ρ_e in e/nm^3]	376.7	377.2	377.1	377	0.26	0.5
PEEK [ρ_e in e/nm^3]	404.9	405.4	405.3	405.2	0.26	0.5
POM [ρ_e in e/nm^3]	451.3	451.5	452.7	451.8	0.76	1.2

calibration is only slightly worse than the electron-density resolution defined by the image noise.

A complementary study was designed to examine the influence of beam hardening on the quantitative results. In general, the differences in attenuation are rather small between various soft tissues. Most tissue types have slightly higher linear attenuation coefficients than water with the exception of adipose tissue (fat), which exhibits a lower attenuation. The employment of a water bath should eliminate most beam hardening effects, because variations in attenuation that are caused by the shape of the sample are confined by adapting the factual penetration length to the thickness of the water container. Three measurements were performed to get an impression of the inaccuracies that still arise from beam hardening. A falcon tube, which is usually used for CT scans of soft-tissue samples at the setup, was filled with water, then with olive oil to resemble adipose tissue, and finally with a 5 % NaCl (in water) solution to simulate the attenuation caused by muscle or connective tissue. For the comparison of electron-density values, four small polypropylene tubes (⌀ 5 mm) filled with water, olive oil, 5 % NaCl (in water), and blood as well as three PMMA rods were placed in the falcon tube for each measurement. The three measurements were conducted in setup configuration F and at a tube voltage of 40 kV. For all three scans, 1200 projections were recorded with 11 steps and 3 s exposure time. Exemplary imaging results are presented in Figure 5.5.

The effective energies $E_{\text{eff},\mu}$ and $E_{\text{eff},\delta}$ were again evaluated by using one of the PMMA rods for the calibration. They accounted for 27.2 keV (water), 27.1 keV (oil), and 27.6 keV (5 % NaCl) in attenuation contrast and 27.0 keV (water), 26.9 keV (oil), and 27.3 keV(5 % NaCl) in phase contrast. As expected, they vary with the three fillings of the falcon tube due to the different absorption properties

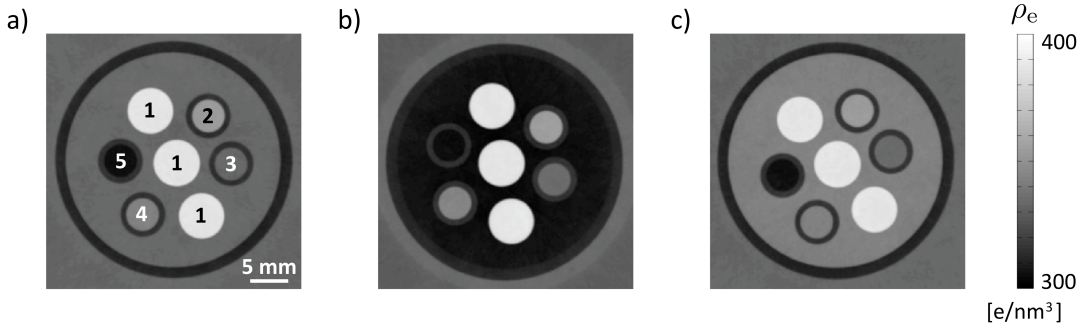

Figure 5.5: Quantitative phase-contrast imaging results of three phantom measurements to investigate the effects of beam hardening on electron-density values. Three PMMA rods [1] and four small polypropylene tubes (filled with blood [2], water [3], 5 % NaCl-water-solution [4], and olive oil [5]) were placed within a falcon tube (⌀ 3 cm). The falcon tube was then filled with another liquid for each of the three scans to simulate the attenuation that is caused by different tissue types. a) Water to resemble muscle tissue. b) Olive oil to resemble adipose tissue. c) 5 % NaCl-water-solution to resemble connective tissue.

Table 5.2: Scan parameters of the three phantom measurements to investigate the effects of beam hardening on the quantitative imaging results.

	scan 1	scan 2	scan 3
setup configuration	*F*	*F*	*F*
voltage [kV]	40	40	40
tube fluid	water	oil	5 % NaCl
$E_{\text{eff},\mu}$ [keV]	27.2	27.1	27.6
$E_{\text{eff},\delta}$ [keV]	27.0	26.9	27.3
noise [σ_{ρ_e} in e/nm^3]	0.7	0.7	0.7
water [ρ_e in e/nm^3]	333.9	334.2	334.0
oil [ρ_e in e/nm^3]	305.8	306.0	305.9
5% NaCl [ρ_e in e/nm^3]	343.4	344.5	343.1
blood [ρ_e in e/nm^3]	354.1	355.1	353.6
PMMA [ρ_e in e/nm^3]	386.3	387.1	386.1
PMMA [ρ_e in e/nm^3]	386.1	387.2	386.1

of the respective liquids. However, the influence of the sample on the effective energy is only small, especially in phase contrast. The electron densities that were determined for the four substances in the inserted little tubes and the other two PMMA rods are listed in Table 5.2. The largest differences of the respective values between the single scans are in the range of 1 to 1.5 e/nm^3 and about twice as high as the actual image noise, which was about 0.7 e/nm^3 in all three measurements.
In conclusion, an accuracy in the electron-density evaluation of about 1–2 e/nm^3 can be achieved despite the polychromatic X-ray source, if the PMMA calibration is applied and the sample is submerged in a water bath. This is valid for soft-tissue samples as long as no highly absorbing features are present. Another presupposition is that the properties of PMMA are known. Possible density variations can affect the effective energies that are determined during the calibration procedure and, thus, lead to wrong electron densities. The PMMA rods that were included in the phantom for the beam hardening study, however, gave consistent results within each of the scans (Table 5.2). This suggests that the material deviations between different PMMA rods are very small and do not markedly degrade the precision.

5.4 Complementarity of signals

Grating-based phase-contrast CT delivers perfectly co-registered distributions of electron densities $\rho_\mathrm{e}(x,y,z)$ and linear attenuation coefficients $\mu(x,y,z)$ within the examined object. As discussed in Chapter 2, the attenuation of X-rays can be largely attributed to photoelectric absorption [ph] and incoherent Compton scattering [incoh]

$$\mu = \mu_\mathrm{ph} + \mu_\mathrm{incoh} = \rho_\mathrm{a}\left(\sigma_\mathrm{a}^\mathrm{ph} + \sigma_\mathrm{a}^\mathrm{incoh}\right). \tag{5.14}$$

Following Equation 2.11, the linear attenuation coefficient for photoelectric absorption can be expressed by

$$\mu_\mathrm{ph} = \sum_i \rho_\mathrm{a,i} C \frac{Z_i^k}{E^3} = \rho_\mathrm{e} C \frac{Z_\mathrm{eff}^l}{E^3}, \tag{5.15}$$

with $l = k - 1$. The material-specific effective atomic number is defined as

$$Z_\mathrm{eff} = \left(\sum \alpha_i Z_i^l\right)^{1/l}, \tag{5.16}$$

where α_i is the fraction of the total number of electrons associated with each element. The attenuation that is caused by photoelectric absorption, thus, yields information on the density and the material composition of the object. In contrast, the linear attenuation coefficient for Compton scattering is according to

Table 5.3: Electron densities and linear attenuation coefficients of different plastic materials and water, which were evaluated from phantom measurements at tube voltages of 35 kV and 50 kV (see Figure 5.4). The effective atomic numbers were calculated from the elemental compositions of the materials.

material	ρ_e (35 kV) [e/nm^3]	μ (35 kV) [1/cm]	ρ_e (50 kV) [e/nm^3]	μ (50 kV) [1/cm]	Z_eff (calc.)
LDPE	315.5	0.296	316.2	0.231	5.44
nylon	377.2	0.418	377.1	0.295	6.12
PEEK	405.9	0.461	405.3	0.321	6.38
POM	451.5	0.607	452.7	0.392	6.95
PMMA	385.8	0.460	385.9	0.315	6.47
water	333.4	0.509	333.5	0.314	7.42

Equation 2.12 given by

$$\mu_\mathrm{incoh} = \sum_i \rho_{\mathrm{a,i}} Z_i \sigma_\mathrm{kn}(E) = \rho_\mathrm{e} \sigma_\mathrm{kn}(E) \tag{5.17}$$

and only depends on the electron density $\rho_\mathrm{e}(x, y, z)$ of the object. As a consequence, the signal in attenuation contrast is proportional to the signal that is obtained in phase contrast, if the attenuation process is purely caused by Compton scattering. Otherwise, the linear attenuation coefficient $\mu(x, y, z)$ contains additional information on the material composition and the imaging results provided by attenuation contrast and phase contrast are complementary.
This signal behavior can be illustrated by the phantom data that was acquired at tube voltages of 35 kV and 50 kV in the previous section. The linear attenuation coefficients obtained for the five plastic rods (LDPE, nylon, PEEK, POM, PMMA) and the surrounding water in the two measurements are plotted versus their corresponding electron-density values in Figure 5.6. The numbers are further listed in Table 5.3 together with the effective atomic numbers of the materials, which were calculated using Equation 5.16 and $l = 2.94$ (Spiers 1946).
Figure 5.6a shows the results from the CT scan at 35 kV ($E_{\mathrm{eff},\mu} = 25$ keV). Nylon ($Z_\mathrm{eff} = 6.12$), PMMA ($Z_\mathrm{eff} = 6.47$), and PEEK ($Z_\mathrm{eff} = 6.38$) have electron densities higher than that of water ($Z_\mathrm{eff} = 7.42$), but present a comparably lower attenuation due to their smaller effective atomic numbers. The linear attenuation coefficients of PMMA ($\rho_\mathrm{e} = 385.5\,\mathrm{e/nm^3}$) and PEEK ($\rho_\mathrm{e} = 405.9\,\mathrm{e/nm^3}$) are nearly identical. Although the electron density of PEEK and, thus, the attenuation by Compton scattering is increased, the higher effective atomic number of PMMA results in a larger contribution of photoelectric absorption. In total, the overall attenuation of both materials is the same. This circumstance changes for the measurement that was performed at 50 kV ($E_{\mathrm{eff},\mu} = 34.4$ keV). Here, PMMA has a smaller linear attenuation coefficient than PEEK. Water as well

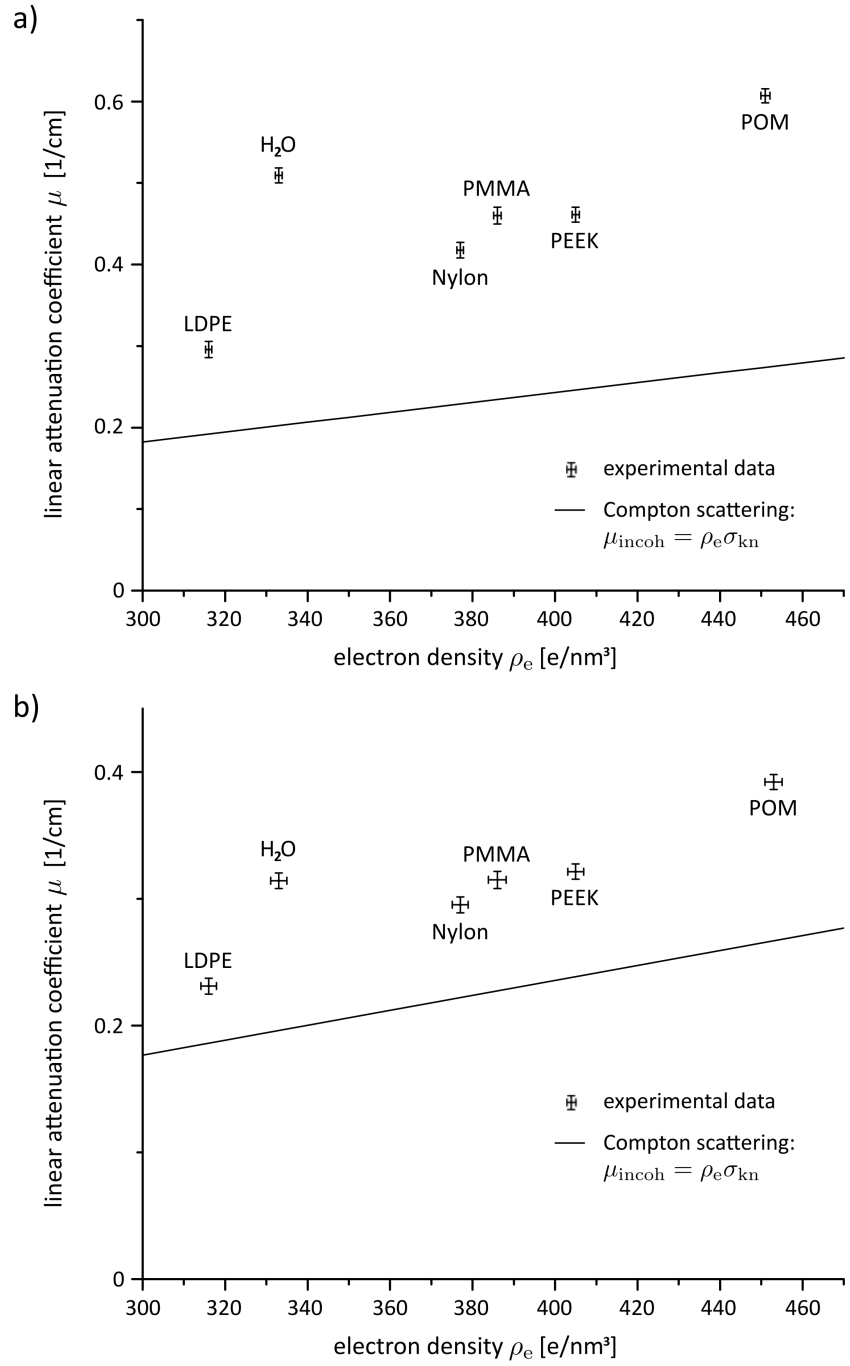

Figure 5.6: Experimental linear attenuation coefficients μ versus corresponding electron densities ρ_{e} obtained from CT measurements at 35 kV (a) and 50 kV (b). Standard deviations are indicated by error bars and the solid line represents the linear attenuation coefficient for Compton scattering μ_{incoh}.

exhibits a lower attenuation than PEEK at this effective energy. Because the photoelectric absorption declines with higher X-ray energies, the differences in the elemental composition of PMMA, water, and PEEK become less important compared to their electron densities. In general, there is less complementarity between $\mu(x, y, z)$ and $\rho_e(x, y, z)$ in the scan at 50 kV than in the scan at 35 kV. As a consequence, the values in Figure 5.6b approach a line. The crucial factor for this observation is the increased contribution of Compton scattering to the overall attenuation. It becomes visually apparent by adding the linear relationship of $\mu_{\text{incoh}} = \rho_e \sigma_{\text{kn}}(E)$ to the graphs in Figure 5.6. Another illustration of the grown relevance of Compton scattering at an X-ray energy of 34.4 keV (effective energy of the scan at 50 kV) compared to 25 keV (effective energy of the scan at 35 kV) is done in Figure 5.7. Here, the ratios of Compton scattering to the total linear attenuation coefficient of light elements ($Z = 1 - 14$) are plotted for both effective energies. The values are based on tabulated data (Berger et al. 2010).
Due to the strong dependence of the photoelectric absorption on the atomic number Z, the Compton scattering ratio decreases for heavier elements at constant energy. This implies that the effective atomic number Z_{eff} of an unknown material can be determined, if the effective energy $E_{\text{eff},\mu}$ of the measurement and the respective Compton scattering ratio for the material are known. Whereas $E_{\text{eff},\mu}$ is anyway specified during the PMMA calibration process, the Compton scattering ratios can be directly obtained from the phase-contrast and attenuation-contrast data according to

$$\frac{\mu_{\text{incoh}}}{\mu} = \frac{\rho_e \sigma_{\text{kn}}(E_{\text{eff},\mu})}{\mu}, \tag{5.18}$$

where the Klein-Nishina cross section σ_{kn} for $E_{\text{eff},\mu}$ can be calculated (Jackson & Hawkes 1981).
Plotting the experimental Compton scattering ratios of the phantom materials against their calculated effective atomic numbers into the graphs of Figure 5.7, all values are well in line with the tabulated data of the single elements.
A more detailed discussion on the complementarity of the signals and on the possibility to assign an effective atomic number to a material by combining both contrast mechanisms is given by Qi et al. (2010) and Chabior (2011).

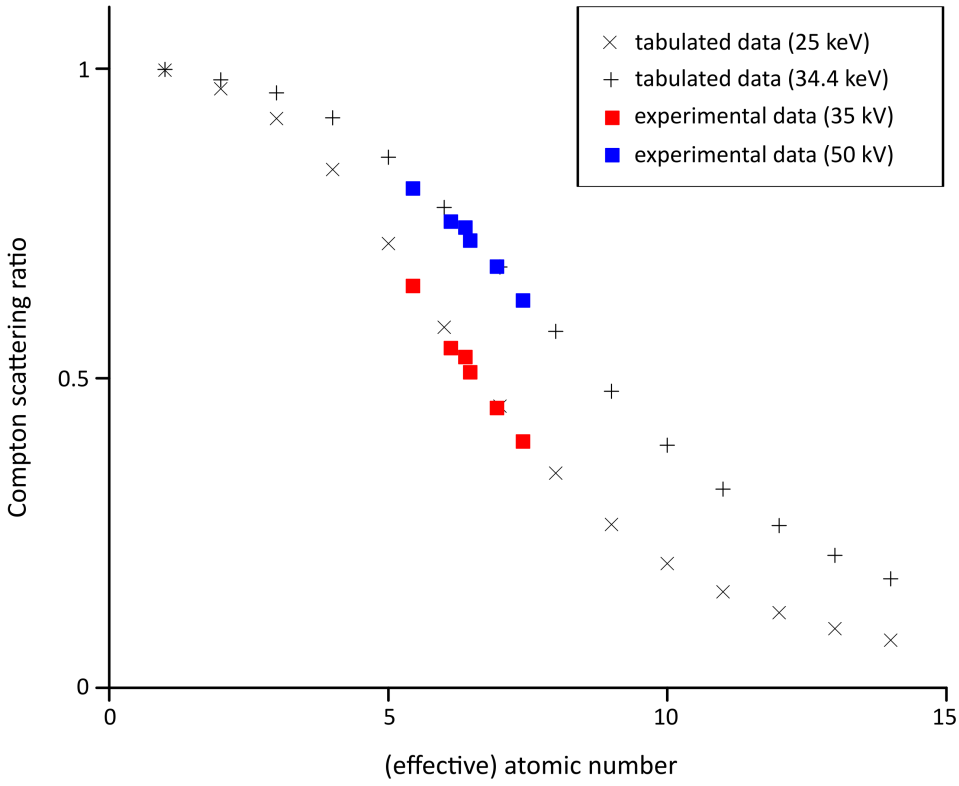

Figure 5.7: The ratio of Compton scattering to the linear attenuation coefficient μ_{incoh}/μ of single elements at two different energies (black markers). The combination of attenuation and phase contrast allows to determine the contribution of Compton scattering to the attenuation process within a material. The colored squares represent the experimental results from the phantom measurements in Figure 5.6 plotted against the calculated effective atomic numbers of the respective materials.

Chapter 6

Hounsfield scale of soft tissues

6.1 Definition of Hounsfield units

In daily diagnostics, the use of Hounsfield units (HU) simplifies the differentiation of certain tissue types with medical CT systems by assigning setup-independent quantitative values to them. These units are defined by

$$\mathrm{HU} = \frac{\mu_{\mathrm{tissue}} - \mu_{\mathrm{water}}}{\mu_{\mathrm{water}} - \mu_{\mathrm{air}}} \cdot 1000, \tag{6.1}$$

where μ_{tissue}, μ_{water}, and μ_{air} are the linear attenuation coefficients of the associated tissue, water, and air. In the Hounsfield scale, the value -1000 represents the attenuation of air and 0 is the attenuation of water. There is no upper limit of the scale. Bones can have HU values of up to 3000 and metallic foreign bodies or implants display even higher numbers. Nearly all types of soft tissues exhibit values between 20 HU and 60 HU except of adipose tissue (fat), which has values between -70 HU and -100 HU. Most of the bodily fluids like blood have values in the same range as tissues. Protein-poor fluids can be noticed by numbers slightly above 0 HU, while fresh hemorrhage can reach up to 80 HU (Prokop & Galanski 2003).
A similar Hounsfield scale (HUp) has been proposed for phase-contrast imaging by replacing the respective linear attenuation coefficients μ by the corresponding refractive index decrements δ (Donath et al. 2010):

$$\mathrm{HUp} = \frac{\delta_{\mathrm{tissue}} - \delta_{\mathrm{water}}}{\delta_{\mathrm{water}} - \delta_{\mathrm{air}}} \cdot 1000. \tag{6.2}$$

Combining Equations 2.15 and 6.2 yields the relation

$$\mathrm{HUp} = \frac{\rho_{\mathrm{e,tissue}} - \rho_{\mathrm{e,water}}}{\rho_{\mathrm{e,water}} - \rho_{\mathrm{e,air}}} \cdot 1000, \tag{6.3}$$

which reveals that phase-contrast Hounsfield units are energy-independent. This is in contrast to conventional Hounsfield units, which are rather constant at clinical CT energies (tube voltages of around 120 kV), but show a strong energy dependence at low energies due to a varying contribution of photoelectric absorption and Compton scattering to the overall attenuation.
If air is neglected in the definition of phase-contrast Hounsfield units, the deviation from exact values is only about 0.1 %. In this case, the measured HUp value can be easily converted to identify a tissue's electron density by reversing Equation 6.3 to

$$\rho_{\mathrm{e,tissue}} = \left(1 + \frac{\mathrm{HUp}}{1000}\right) \rho_{\mathrm{e,water}}, \tag{6.4}$$

where $\rho_{\mathrm{e,water}} = 334\,\mathrm{e/nm^3}$. Positive and negative HUp values, thus, indicate electron densities above and below that of water, respectively. Phase-contrast HU (without air) directly result from division by the theoretical δ_{water}-value and subsequent multiplication by 1000, if the data is recorded relative to water $\delta_{\Delta}(x_i, y_i, z_i) = \delta_{\mathrm{tissue}}(x_i, y_i, z_i) - \delta_{\mathrm{water}}$. The δ_{water}-value can be calculated for the respective effective energy of the measurement, which can be obtained by applying the PMMA calibration as described in the previous chapter. Simplified, the conversion into HUp can be understood as linear rescaling of the original dataset with water (0 HUp) and PMMA (approx. 156 HUp) being the fixed points.
The evaluation of HUp values by phase-contrast CT provides valuable insight into whether the phase-contrast method can adequately discriminate between tissues or not. The energy independence of HUp additionally enables to examine the sensitivity demands of a phase-contrast CT system. As phase-contrast Hounsfield units comprise the electron densities of tissues, they can serve as reference values for simulations and the design of dedicated phantoms for phase-contrast imaging.
In this chapter, phase-contrast Hounsfield units were determined for various types of non-fixated human soft tissues. A large variety of tissue specimens were imaged and their quantitative values were compared to commonly used reference values that are tabulated in the literature. Because X-ray phase-contrast CT is not yet clinically available and biomedical research is currently performed on excised and fixated tissue samples, the effects of formalin fixation on the quantitative phase-contrast imaging results were further investigated. Results, figures, tables, and text parts have been previously published in the article *Phase-contrast Hounsfield units of fixated and non-fixated soft-tissue samples* (Willner et al. 2015).

6.2 Non-fixated human soft tissues

A study for the evaluation of HUp values was conducted on various types of human soft tissues including muscle and adipose tissue, skin, tendon, brain, and several internal organs (heart, liver, spleen, kidney, and pancreas). The experimental results were then compared to literature values calculated from electron

densities that were published by Woodard & White (1986) and derived from elemental compositions. The data of Woodard and White are suggested as reference values by the *International Commission on Radiation Units and Measurements* (ICRU 1989) and underlie many theoretical considerations such as X-ray dose calculations or simulations of phase-contrast imaging.
The investigated human tissue samples were collected at the *Institute of Forensic Medicine* (*Ludwig-Maximilians-Universität München*) under the approval of the ethics committee of the *Faculty of Medicine* (*Technische Universität München*). The review board waived the need for individual consent. Two small pieces of the following tissue types were obtained: heart muscle, skin, tendon, liver, spleen, kidney, pancreas, and brain. The heart muscle, skin, and kidney samples further contained adipose tissue. The tissues were retained in physiological phosphate buffered saline solution (PBS) and stored in the refrigerator at 4°C. Each tissue type was scanned no later than three days after excision.
For the measurements, each sample was placed in the aforementioned plastic cylinders of ∅ 3 cm, which were filled with PBS. PMMA rods were inserted into the tubes for the subsequent calibration of HUp. Throughout the measurements, samples were submerged in a water bath with a thickness of 4 cm and the water was continuously cooled to 4°C to prevent decay of the tissue samples. The samples were scanned in the setup configuration *F* (see Table 4.1). A tomographic scan included 1200 projections consisting of 11 phase-step images, recorded with an exposure time of 3 s per image. The applied tube voltage was 40 kV and the tube current was set to 70 mA. The reconstructed 3D datasets were converted into HUp, neglecting the air contribution. The final data were digitally stored in DICOM-format and analyzed using the software *OsiriX 4.0* (32 bit). To quantify the HUp values, ten ROIs were selected within each tissue type for each measurement and their averages were determined. The mean value and standard deviation of the ten averages were calculated.
Figure 6.1 displays six representative tomographic phase-contrast images of human soft-tissue samples. The evaluated HUp values of all investigated tissue types are presented in Table 6.1. The standard deviations of the ten ROIs' averages are listed (round brackets) and give an idea of the variations within one tissue. For comparison, the literature values from Woodard and White are also listed. They recorded three different densities for some tissue types, reflecting the high variance in their results of which Table 6.1 lists the minimum and maximum.
In the present investigation, the HUp values of muscle tissue are most consistent with the literature values. The two heart muscles yielded values of 37 HUp and 40.7 HUp. The corresponding literature values are approximately 40 HUp. The deviation from literature is less than 3 HUp (i.e., less than 1 e/nm^3 in the electron-density picture). Six HUp values were obtained for adipose tissue; two each from the heart, skin, and kidney samples. The HUp values of adipose tissue range from −42.3 HUp to −63.4 HUp, within the range reported in the literature (−30.6 HUp

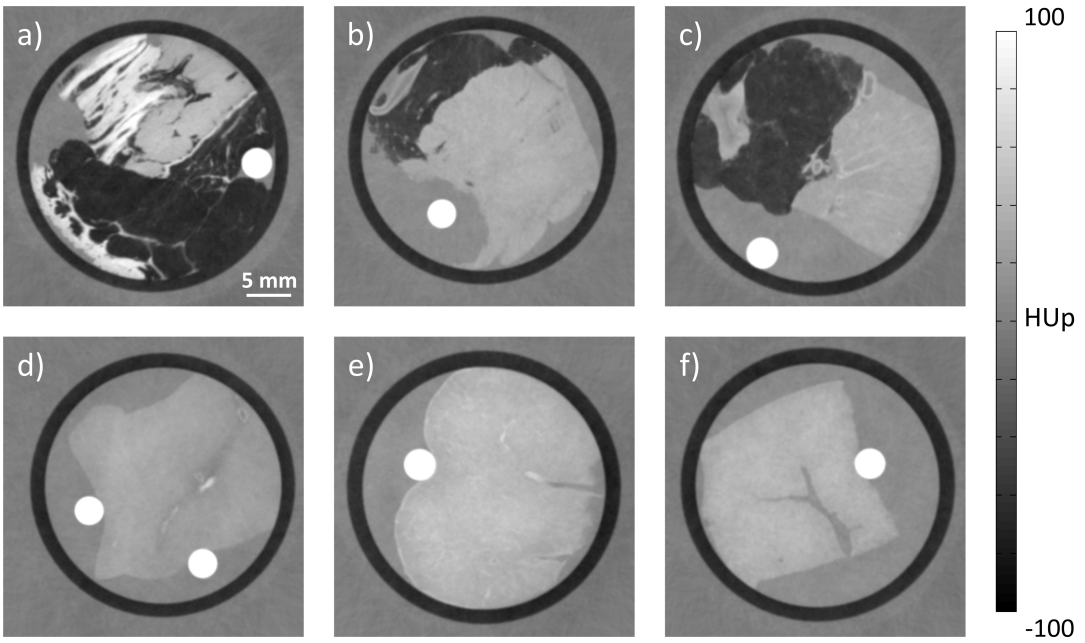

Figure 6.1: Representative phase-contrast imaging results of human tissue samples. a) Sample comprising tendon (bright, top), skin (bright, bottom), and adipose tissue (dark structures). b) Heart muscle tissue with portions of fatty tissue. c) Renal and adipose tissue. d) Brain tissue. e) Spleen tissue. f) Piece of liver tissue. In each image, the high-intensity circular areas are PMMA rods, which are used to calibrate the quantitative phase-contrast Hounsfield units. [Figure adapted from Willner et al. (2015).]

to −66.6 HUp). The HUp results of liver are 53.8 HUp and 41.7 HUp, which are also comparable to the literature values (41.2 HUp to 59.2 HUp). The single electron density of skin reported by Woodward and White (78 HUp) is intermediate between the experimental results of 74.3 HUp and 93.8 HUp. The determined HUp values of the inner organs (spleen, kidney, and pancreas) are up to 10 HUp lower than their corresponding literature values: 44. HUp and 45.9 HUp versus 52.1 HUp for spleen, 32.9 HUp and 32.1 HUp versus 40.3–42.2 HUp for kidney, and 26.4 HUp and 34.3 HUp versus 34.1 HUp for pancreas. Furthermore, the experiments yielded lower HUp values for tendon and brain tissue: 66.5 HUp and 90.1 HUp versus 101.6 HUp for tendon; 29.1 HUp and 32.9 HUp versus 34/35 HUp for brain tissue.

The consistency of the measured phase-contrast Hounsfield units with the literature values confirm that commonly used reference values are suitable for simulations, phantom design, and dose calculations. Unfortunately, the literature values cannot capture the different compositions of diverse tissue types and theoretical approaches are limited to universally classified tissue types. Consequently, sim-

Table 6.1: Phase-contrast Hounsfield units of various human soft-tissue types that were evaluated from measurements and calculated from tabulated literature data. Ten ROIs were analyzed for each tissue type and measurement. The listed numbers are the mean values and standard deviations (round brackets) of the regions' averages. [Table adapted from Willner et al. (2015).]

	sample 1	sample 2	literature
muscle	37.0 (2.2) HUp	40.7 (3.2) HUp	39.4/40.4 HUp
adipose	−42.4 (3.9) HUp	−45.3 (3.2) HUp	−30.6/−66.6 HUp
	−51.3 (1.8) HUp	−48.0 (5.0) HUp	
	−55.7 (4.1) HUp	−63.4 (4.6) HUp	
skin	93.8 (6.7) HUp	74.3 (9.5) HUp	78.0 HUp
liver	53.8 (1.8) HUp	41.7 (1.8) HUp	41.2/42.2 HUp
spleen	44.1 (3.3) HUp	45.9 (2.7) HUp	52.1 HUp
kidney	32.9 (1.7) HUp	32.1 (4.7) HUp	40.3/42.2 HUp
pancreas	26.4 (2.4) HUp	34.3 (3.1) HUp	34.1 HUp
tendon	66.5 (4.7) HUp	90.1 (7.2) HUp	101.6 HUp
brain	29.1 (1.7) HUp	32.9 (2.3) HUp	34/35 HUp

ulation studies may not explore the full potential of phase-contrast imaging and may therefore overlook interesting applications as demonstrated in Chapter 7. Some of the measured HUp values were considerably lower (by up to 10 HUp) than their literature equivalents. Expressed in electron densities, this deviation is small (approximately 1 %) and is attributed either to the natural spectrum of tissue densities or to post-mortem tissue decomposition. Extending the presented results to an in-vivo scenario, the measured HUp values may also be influenced by lack of blood flow in a tissue's vascular system and the shrinkage induced by tissue excision (Dauendorffer et al. 2009). Non-fixated tissues are very soft and buoyant. This makes it difficult to prevent them from slightly moving in the surrounding liquid throughout the measurement. These positional inaccuracies cause blurring in some of the phase-contrast images. Although these motion artifacts do not influence the HUp values, they reduce the visibility of fine tissue structures such as collagen strands.

6.3 Effects of formalin fixation

Research on biomedical phase-contrast imaging is mostly conducted on fixated tissue samples due to longer time periods between the tissue excision, the actual measurement, and the subsequent histopathological workup in the clinics, which is often used as gold standard for reference. The fixation step stabilizes the fine-structural details of cells and tissues prior to examination and is most commonly performed in aldehyde (Kiernan 2000). Although formalin fixation

preserves tissues from decay, it induces intra- and inter-molecular cross-linking of macromolecules, thereby altering the physical characteristics of the tissues (Fox et al. 1985). Consequently, the imaging results may considerably deviate from those of non-fixated samples, leading to incorrect impressions of the possible clinical benefits. For this reason, another study was designed to quantify HUp in fixated and non-fixated tissues and to evaluate the effects of formalin fixation on phase-contrast imaging. Two series of measurements were performed on porcine muscle, fat, and rind samples. First, the differences in the quantitative HUp values of fixated and non-fixated tissue samples were investigated. Then, the relationship between the obtained HUp values and formalin concentration was examined.

For the two series, porcine fat and rind was obtained from the local butcher and cut into cubic pieces (approximately 2 cm each side). Representative samples are photographed in Figure 6.2a. All samples included the rind (representing skin or connective tissue), two layers of fat (adipose tissue), and two layers of muscle tissue. The non-fixated samples were immersed in PBS and measured within 24 h of acquisition and preparation. The fixated samples were placed in containers filled with different concentrations of formaldehyde gas in water (1.85 %, 3.7 %, 7.4 %, 12.3 %, and 18.5 %) and were incubated for approximately 2 weeks before measurement. All samples were again cooled to 4°C during the phase-contrast CT scans, which included 1200 projections with 11 images and 3 s exposure time. The images were acquired with setup configuration F and a tube voltage of 40 kV. The first series of measurements included five non-fixated samples of porcine fat and rind (in PBS) and five samples that were preserved in 3.7 % formaldehyde solution (typical formaldehyde concentration of tissue fixative). The results of these measurements were used to identify the variances of a tissue's HUp value among different samples and to quantify the magnitude of formalin-induced changes. The second series of measurements was performed to get a better idea of how or why the formalin fixation may influence a tissue's HUp value. Four additional porcine fat and rind samples were examined within this series, each of them prepared with a different concentration of formaldehyde gas in water (1,85 %, 7.4 %, 12.3 %, and 18.5 %).

Representative tomographic phase-contrast imaging results of a non-fixated and two fixated (in 3.7 % and 18.5 % formaldehyde solution) porcine samples are displayed in Figure 6.2. The different tissue layers are clearly distinguishable in all three axial slices. Skin yields the brightest signal, adipose tissue appears darker than the surrounding water, and muscle tissue shows intermediate brightness. The PMMA rods used for the calibration appear as small white circular areas to the left of the porcine fat and rind. Visually, the non-fixated and fixated samples are very similar. The major difference is that formalin stiffens the fixated samples, preventing their conformation to the plastic cylinder as observed for non-fixated tissues. The image noise in all measurements is approximately 3 HUp. The HUp

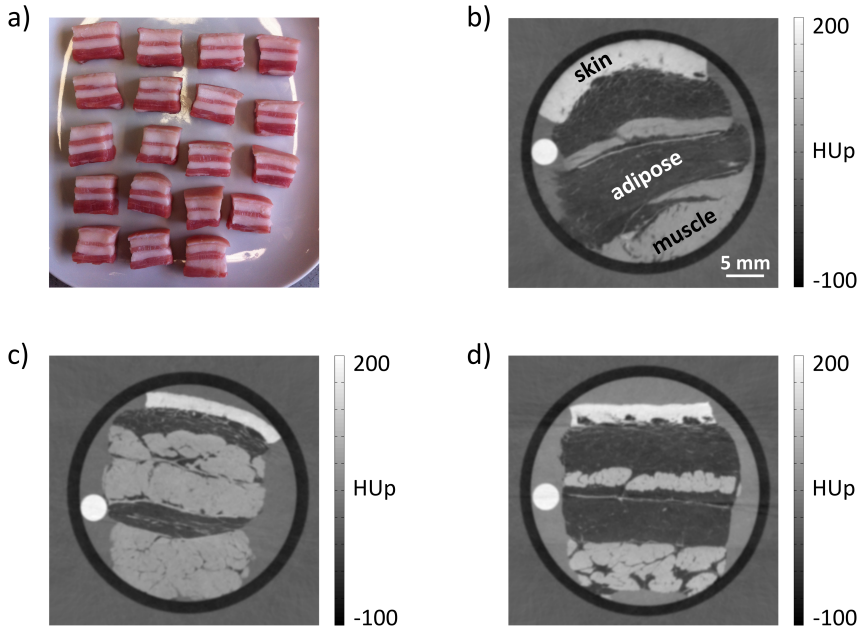

Figure 6.2: Representative phase-contrast imaging results of non-fixated and fixated tissue samples. a) Photograph of porcine fat and rind samples, on which the effects of formalin fixation were investigated (note the presence of skin, muscle, and adipose tissue). Samples were immersed in physiological saline or fixated with formaldehyde solutions of varying concentrations. b) Phase-contrast axial slice through a non-fixated porcine sample. Skin, muscle, and adipose tissues are clearly differentiated by their signal intensities. c) Phase-contrast image of a sample fixated in typical preservation solution (containing 3.7 % formaldehyde). d) Phase-contrast image of a sample fixated in 18.5 % formaldehyde solution. The signal intensities in (b) are visually indistinguishable from those of (c). [Figure adapted from Willner et al. (2015).]

values of the three tissue types that were obtained for the five non-fixated (PBS) and the five fixated (3.7 %) samples, and their corresponding means, are listed in Table 6.2.

Fresh and fixated adipose tissue ranges from −30.1 HUp to −35.7 HUp and from −28.5 HUp to −33 HUp, respectively, with respective means of −32.2 HUp and −31.0 HUp. The difference is within the image noise, suggesting that fixation induces marginal changes in the quantitative tissue values. In contrast, fixation affects the values of muscle tissue and skin. In both cases, fixation increases the HUp values by approximately 10 % (55.8 HUp versus 62.3 HUp in muscle tissue and 108.8 HUp versus 119.1 HUp in skin). The graphical overview in Figure 6.3a provides a quick visual assessment of these results.

Table 6.2 further displays the standard deviations that were calculated during the

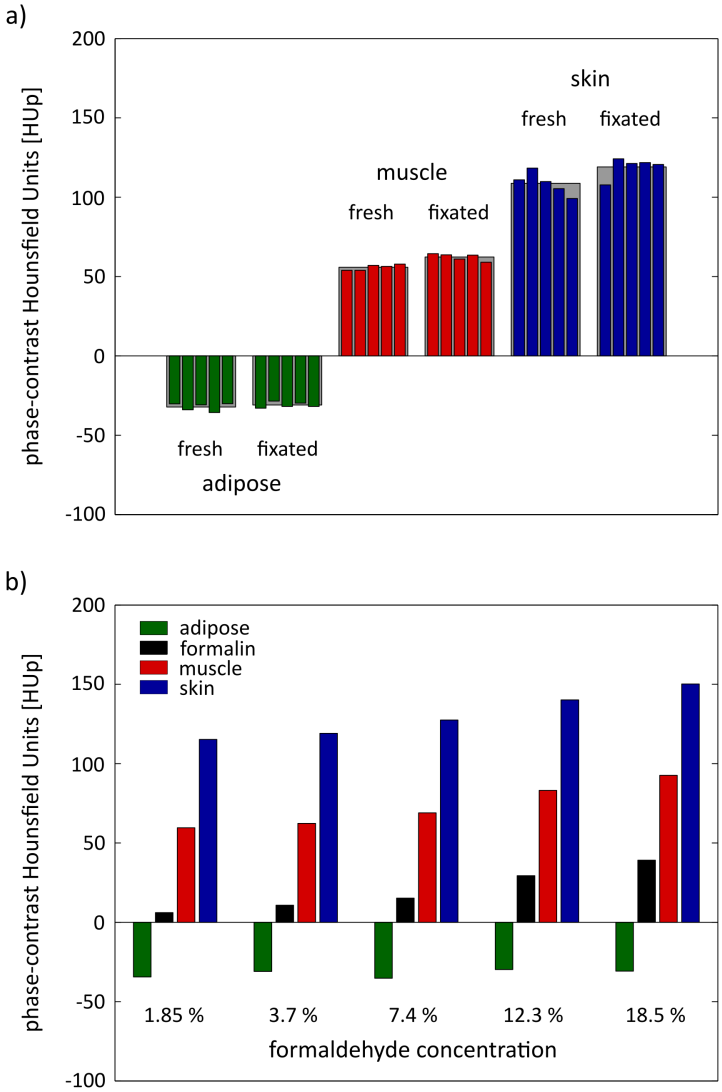

Figure 6.3: Graphical representation of the quantitative analysis of non-fixated and fixated tissue samples. a) Comparison of phase-contrast Hounsfield units that were evaluated for five non-fixated porcine samples and five samples fixed in 3.7 % formaldehyde solution. Formalin fixation does not affect adipose tissue, but increases the Hounsfield units of muscle and skin by approximately 10 %, most likely by tissue shrinkage. b) Phase-contrast Hounsfield units of the three investigated tissue types fixated at different formaldehyde concentrations. Again, adipose tissue is not altered by the fixation, but the HUp of muscle and skin increase with higher concentrations. This effect is due to replacement of water by the formaldehyde solution within the tissues. [Figure adapted from Willner et al. (2015).]

Table 6.2: HUp values of five non-fixated (fresh) and five fixated (3.7 % formaldehyde solution) tissue samples containing adipose tissue, muscle tissue, and skin. The numbers in regular typeface represent the mean values and standard deviations (round brackets) obtained from ten ROIs that were analyzed for each of the three tissue types and each individual sample. The bold numbers finally give the mean values and standard deviations (square brackets) of these individual results and reflect the differences in the tissues' HUp in non-fixated and fixated state. [Table adapted from Willner et al. (2015).]

	adipose	muscle	skin
fresh sample 1	−30.3 (3.3) HUp	53.9 (2.0) HUp	111.0 (4.0) HUp
fresh sample 2	−34.0 (4.0) HUp	54.0 (3.4) HUp	118.4 (5.3) HUp
fresh sample 3	−30.8 (3.0) HUp	57.0 (3.3) HUp	109.9 (4.4) HUp
fresh sample 4	−35.7 (1.2) HUp	56.4 (3.8) HUp	105.4 (5.1) HUp
fresh sample 5	−30.1 (2.9 HUp	57.9 (3.0) HUp	99.2 (3.6) HUp
fixated sample 1	−33.0 (3.0) HUp	64.4 (2.9) HUp	107.8 (5.8) HUp
fixated sample 2	−28.5 (3.0) HUp	63.7 (2.2) HUp	124.2 (3.2) HUp
fixated sample 3	−31.8 (3.8) HUp	61.0 (3.7) HUp	121.2 (3.2) HUp
fixated sample 4	−29.8 (1.7) HUp	63.5 (3.0) HUp	121.8 (4.5) HUp
fixated sample 5	−31.9 (0.9) HUp	59.1 (1.2) HUp	120.6 (2.4) HUp
fresh (mean)	**−32.2 [2.5] HUp**	**55.8 [1.8] HUp**	**108.8 [7.1] HUp**
fixated (mean)	**−31.0 [1.8] HUp**	**62.3 [2.2] HUp**	**119.1 [6.5] HUp**

data handling. The standard deviations of the ten ROIs that were analyzed for each tissue type and measurement are stated in round brackets. They illustrate the variance of a tissue's HUp within one sample. The standard deviations of the five mean values that were determined for a certain tissue type in the non-fixated and fixated case are given in square brackets. These numbers represent the variance of a tissue's HUp among different samples. Most standard deviations are in the order of image noise (3 HUp) or smaller, implicating that uncertainties arising from tissue variability can be assumed to be low. Higher standard deviations are obtained for skin.

In addition to the five samples fixated with 3.7 % formaldehyde solution, four porcine pieces that were fixated at different formaldehyde concentrations (1.85 %, 3.7 %, 7.4 %, and 18.5 %) were examined to get a clearer picture of the reasons for the formalin-induced changes. The determined HUp values of fat, muscle, and rind at each formaldehyde concentration are presented in Table 6.3. For the case of no fixation and 3.7 % formaldehyde concentration, the mean values of the five samples from the first series are listed. The HUp values of the respective PBS or formaldehyde solutions are added to the analysis. The results are further illustrated in Figure 6.3b. The quantitative HUp values of adipose tissue are insensitive to formaldehyde concentration, whereas the HUp values of muscle tissue and

Table 6.3: Effect of formaldehyde concentration on the quantitative phase-contrast Hounsfield units of adipose tissue, muscle tissue, and skin. For higher formaldehyde concentrations, the increase in the Hounsfield units of muscle tissue and skin correlates with the Hounsfield unit of the formaldehyde solution itself. [Table adapted from Willner et al. (2015).]

	adipose 1	muscle	skin	PBS/formalin
no fixation (PBS)	−32.2 HUp	55.8 HUp	108.8 HUp	8.8 HUp
1.85 % formaldehyde	−34.4 HUp	59.6 HUp	115.3 HUp	6.1 HUp
3.7 % formaldehyde	−31.0 HUp	62.3 HUp	119.1 HUp	10.8 HUp
7.4 % formaldehyde	−35.3 HUp	69.0 HUp	127.5 HUp	15.2 HUp
12.3 % formaldehyde	−29.8 HUp	83.2 HUp	140.2 HUp	29.3 HUp
18.5 % formaldehyde	−30.8 HUp	92.6 HUp	150.2 HUp	39.1 HUp

skin are increasing with higher formaldehyde concentration. The measured HUp values of the formaldehyde solutions themselves follow the same trend; increasing from 6.1 HUp at 1.85 % formaldehyde to 39.1 HUp at 18.5 % formaldehyde. On further examination, the HUp values of muscle tissue and rind are directly correlated with the HUp values of the formaldehyde solution. If the values are adjusted for this effect, they are very similar at all five formaldehyde concentrations: 53.5, 51.5, 53.8, 53.9, and 53.5 HUp in muscle tissue and 109.2, 108.3, 112.3, 110.9, and 111.1 HUp in skin. The porcine fat and rind sample fixated at the highest formaldehyde concentration (18.5 %) was transferred to PBS after the first scan and re-measured several days later. In this measurement, the HUp values were altered to −30.2 HUp (up from −30.8 HUp) in adipose tissue, 61.8 HUp (down from 92.6 HUp) in muscle, and 118.8 HUp (down from 150.2 HUp) in rind. Evidently, the elevated HUp values of muscle tissue and rind in formaldehyde solution were negated after incubation in PBS. However, the HUp values of both tissue types are approximately 10 % higher than those of their fresh counterparts and nearly identical to those of samples fixated with 3.7 % formaldehyde.

Formaldehyde fixation is a complex process initialized by rapid penetration that stops autolysis, followed by covalent bonding and cross-linking with proteins (Fox et al. 1985, Buesa 2008). This process causes stiffening and shrinkage of the tissue sample. The reported shrinkage of excised skin specimens (size change from ex vivo to post-fixation) ranges from minimal to around 10 % (Dauendorffer et al. 2009, Golomb et al. 1991, Gregory et al. 2003, Hudson-Peacock et al. 1995). Substances such as carbohydrates, lipids, and nucleic acids become trapped in the matrix of cross-linked protein molecules, but are not chemically changed by formaldehyde unless fixation is prolonged for several weeks (Kiernan 2000, Heslinga & Deierkauf 1962). Comparing non-fixated porcine samples incubated in PBS with samples fixated in 3.7 % formaldehyde, the HUp values of rind (skin) and muscle were elevated by 10 % in the latter. The corresponding gain in electron

density (≈ 0.5–$1\,\%$) is probably caused by tissue shrinkage. This small density response compared to the large size reduction is attributed to the large amounts of water within tissues, which is displaced but not compressed during the shrinking process. The electron density increases mainly because the existent proteins become more closely packed within the tissues. The quantitative HUp values of muscle and skin tissues are also affected by the replacement of water with formaldehyde solution in fixated samples. The electron density of $3.7\,\%$ formaldehyde solution is similar to that of physiological PBS (337.6 versus $336.9\,\mathrm{e/nm^3}$) and, thus, exerts little impact on the HUp values. At higher formaldehyde concentrations, the solutions' electron densities rise from $339.1\,\mathrm{e/nm^3}$ ($7.4\,\%$ formaldehyde) to $343.8\,\mathrm{e/nm^3}$ ($12.3\,\%$) to $347.1\,\mathrm{e/nm^3}$ ($18.5\,\%$). The electron densities of muscle tissue and rind that are fixated at these concentrations of formaldehyde solution increase by nearly the same amount.

Apparently, formalin fixation elevates the quantitative HUp values (i.e., the electron densities) of soft tissues in two ways. First, the protein cross-linking shrinks the tissues and increases their protein density. Second, the water in the tissues is replaced by the penetrating formalin. This idea is supported by the results of the porcine sample that was initially fixated with $18.7\,\%$ formaldehyde solution and, then, incubated for several days in PBS. The HUp values of muscle and rind significantly decreased after PBS incubation to levels comparable with fixation in $3.7\,\%$ formaldehyde, but remained $10\,\%$ higher than those of unfixed tissue samples incubated in PBS. This indicates that the $10\,\%$ increase in HUp is related to closer packing of the proteins. Adipose tissue was insensitive to fixation at any formaldehyde concentration, probably because its high lipid content confers resistance to formalin within the first two weeks of fixation.

Fixated tissue samples are easier to handle than non-fixated (fresh) tissue samples. If the tissues are preserved, they can be subjected to longer storage and scanning times without cooling. Additionally, because the samples are hardened by the preservation, they remain fixed throughout the measurements, enabling sharp image acquisition. Although formalin fixation increases the electron densities of some tissue types, it does not degrade or artificially enhance the resulting image contrast and, thus, is suitable for most biomedical phase-contrast investigations.

Chapter 7

Breast-tissue characterization

7.1 X-ray imaging of the breast

Breast cancer is the most common cause of cancer death in women worldwide (Ferlay et al. 2010). Although mammographic screening programmes and improved systemic therapy could continuously reduce the mortality over the past decades, the rate of missed lesions and the rate of false positives remains crucial (Berry et al. 2005, Smith & Andreopoulou 2004). Many efforts are therefore made to enhance diagnostic performance, especially of dose-free imaging modalities like MRI or sonography (Kuhl 2007*a*,*b*, Sehgal et al. 2006, Athanasiou et al. 2009, Le-Petross & Shetty 2011). Despite radiation risks, new developments in X-ray imaging are still motivated by benefits such as high resolution, low costs, fast acquisition, and operator independence. Whereas tomosynthesis is already established as novel technique, further activities focus on spectral and full tomographic imaging or the combination of both (Skaane et al. 2013, Ding & Molloi 2012, Schmitzberger et al. 2011, Prionas et al. 2010, Kalender et al. 2012).
With respect to X-ray imaging, the healthy breast is composed of two major tissue types: fibroglandular and adipose tissue. Fibroglandular tissue is a mixture of fibrous connective tissue (the stroma) and the functional (or glandular) epithelial cells that line the ducts of the breast (the parenchyma) (Yaffe 2008). Adipose tissue mainly consists of lipid and has a lower linear attenuation coefficient than fibroglandular tissue. Unfortunately, the attenuation of tumor tissue and fibroglandular tissue is very similar, posing a challenge for tumor detection, especially in dense breasts (Johns & Yaffe 1987). Here, X-ray phase contrast is an interesting alternative.
Phase-contrast examinations of the breast at synchrotron radiation facilities go back to the year 2000 (Arfelli et al. 2000, Pisano et al. 2000). Meanwhile, first patient trials of phase-contrast mammography at the *Elettra synchrotron* in Trieste performed strongly with regards to specificity and sensitivity (Castelli et al. 2011). To grant a broad application of the method in clinical routine, current re-

search concentrates on the translation to standard X-ray tubes and the evaluation of such prototype systems (Tanaka et al. 2005, Faulconer et al. 2009, Stampanoni et al. 2011, Michel et al. 2013). Further prospective results have been achieved by phase-contrast CT (Bravin et al. 2007, Keyriläinen et al. 2008, Sztrókay et al. 2012, 2013). Latest developments in this direction include synchrotron measurements at very low doses (Zhao et al. 2012).

This chapter addresses the question whether quantitative tissue characterization in terms of phase-contrast Hounsfield units might be a valuable tool for future 3D breast diagnostics. Results, figures, tables, and text parts have been previously published in *Quantitative breast tissue characterization using grating-based x-ray phase-contrast imaging* (Willner et al. 2014). In this study, measurements of breast-tissue samples have been performed at the synchrotron and at the laboratory system. One specimen that contains healthy breast parenchyma as well as invasive ductal carcinoma has been scanned with high resolution at the beamline *ID19* of the ESRF. In addition, three excised samples that comprise a benign phylloides tumor, a fibroadenoma, and an invasive lobular carcinoma have been examined at the laboratory phase-contrast imaging setup. Present tissue types were specified by histopathology and the associated quantitative results were compared to values calculated based on literature. The latter is particularly interesting for simulations and the design of adequate phantoms for the optimization of phase-contrast mammography systems (Munro et al. 2010, Raupach & Flohr 2012, Vedantham & Karellas 2013).

In context of theoretical tissue properties, Hammerstein et al. (1979) evaluated densities and elemental compositions of adipose and glandular tissue from fresh mastectomy samples for dose calculations in mammography. By interpolation of the results, densities and elemental compositions for various mixed states of both tissue types can be generated to simulate breast tissue (Boone 1999). The extensive collection of human tissue compositions and densities published by Woodard & White (1986) include adipose and glandular tissue as well. The high variance of values in their analysis are reflected by three different numbers that are stated for both tissue types. As the results are partly listed in the report of the *International Commission on Radiation Units and Measurements* (ICRU 1989), they are the basis of many theoretical considerations involving breast tissue. Further elemental compositions and densities of glandular and adipose tissue that are used for the comparison are taken from Poletti et al. (2002) and were obtained by a commercial elemental analyzer.

Furthermore, electron densities of breast tissues that have been quantified by Compton scattering methods can be found in literature for reference. First results were presented by Shrimpton (1981) who examined adipose and breast tissue among others. The size of the specimens was about 3 cm (side length) and breast tissue was presumably a mixture of both adipose and fibroglandular tissue. Another investigation involving Compton scattering concentrated solely on

breast-tissue samples (including tumor tissue) to determine electron densities for the design of a mammography phantom (Al-Bahri & Spyrou 1998). Later studies, which comprised a high number of samples, were performed to evaluate the potential of Compton scattering for the diagnosis of breast biopsies (Ryan et al. 2005, Antoniassi et al. 2010, 2012).

7.2 Phase-contrast measurements

The study in this chapter was conducted in accordance with the *Declaration of Helsinki* and was approved by the local ethics committee. Written informed consent was obtained before imaging. Indication for breast surgery followed recommendation of the interdisciplinary tumor board of the local *Breast Center* (*Ludwig-Maximilians-Universität München*). The excised breast samples were macroscopically examined by an experienced pathologist. Representative and orientable tissue parts were selected and placed in plastic cylinders (⌀ 3 cm) that were filled with 4 % neutral-buffered formaldehyde solution. Histological workup was performed after the measurements to correlate and identify the tissue types. In total, four different specimens were investigated. The first one contained adipose tissue, healthy fibrous breast parenchyma, and invasive ductal carcinoma. It was scanned at the beamline *ID19* of the ESRF. The energy of the coherent monochromatic beam was set to 23 keV. The height of the silicon phase grating with a period of 4.8 µm was matched to introduce a phase shift of π to the X-rays. The corresponding analyzer grating had a period of 2.4 µm and was positioned 48.1 cm behind the phase grating. A Frelon CCD (type e2v, 2048×2048 pixels), lens-coupled to a LuAG scintillator of 125 µm thickness, has been used as detector. The optics have been set to an effective pixel size of 30 µm. 1199 projections with 4 images have been collected with an exposure time of 0.8 s per image during the tomographic scan. Further information on sample, setup, and measurement, can be found in Sztrókay et al. (2013).
The other three specimens, which included adipose tissue, fibrous tissue, phylloides tumor, fibroadenoma, and invasive lobular carcinoma, were examined at the laboratory phase-contrast imaging system. The CT measurements were carried out in the setup configurations *A*, *C*, and *D* (see Table 4.1) at a tube voltage and current of 40 kV and 70 mA, respectively. For each sample, 1200 projections with 11 images per projection and 5 s exposure time per image were recorded.
Phase-contrast imaging results of the specimen that was measured at the synchrotron are presented in Figure 7.1. The two images display healthy breast parenchyma (bright signal) embedded in adipose tissue (dark signal). Two cubic regions of 0.5 cm side length (170×170×170 voxels) were chosen from the 3D-dataset and their histograms are plotted in Figure 7.1c and d. Region A (marked in Figure 7.1b) mainly contains adipose tissue. The associated histogram has one narrow peak with a maximum at −68 HUp. Region B was chosen to cover

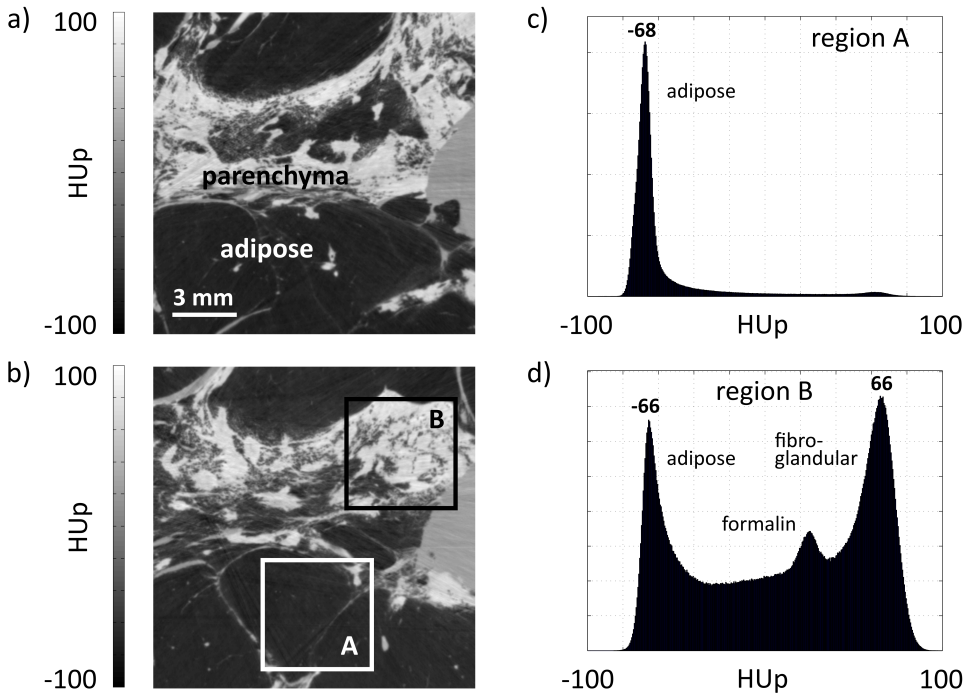

Figure 7.1: Two exemplary tomographic phase-contrast images of healthy breast parenchyma embedded in adipose tissue (a and b) and the distribution of quantitative phase-contrast Hounsfield units (c and d) in two selected cubic ROIs as shown in (b). Whereas adipose tissue yields values around −70 HUp, fibroglandular tissue exhibits positive values with a peak maximum at about 66 HUp. [Figure adapted from Willner et al. (2014).]

as much fibroglandular tissue as possible, but still parts of adipose tissue are enclosed within the parenchyma. Whereas the peak of adipose tissue is again located between −65 HUp and −70 HUp in the histogram, the fibroglandular tissue has its peak maximum at 66 HUp. All values between both tissue types can be found within the analyzed cubic region. The small peak at about 20 HUp corresponds to the surrounding formalin solution.
Further imaging results of the same sample, now comprising adipose tissue and invasive ductal carcinoma, are shown in Figure 7.2. The tumor appears as solid area with clear boundaries (Figure 7.2a). The narrowed scaling of Figure 7.2b reveals bright circular structures within the tumor tissue, which coincide with dilated ducts (Sztrókay et al. 2013). Again, histograms of two cubic regions were prepared to illustrate the distribution of quantitative values. The histogram of region A that was selected within adipose tissue is nearly identical to Figure 7.1c, a narrow peak with its maximum at −68 HUp. Region B contains mainly tumor tissue. The peak in the corresponding histogram has a maximum at 47 HUp,

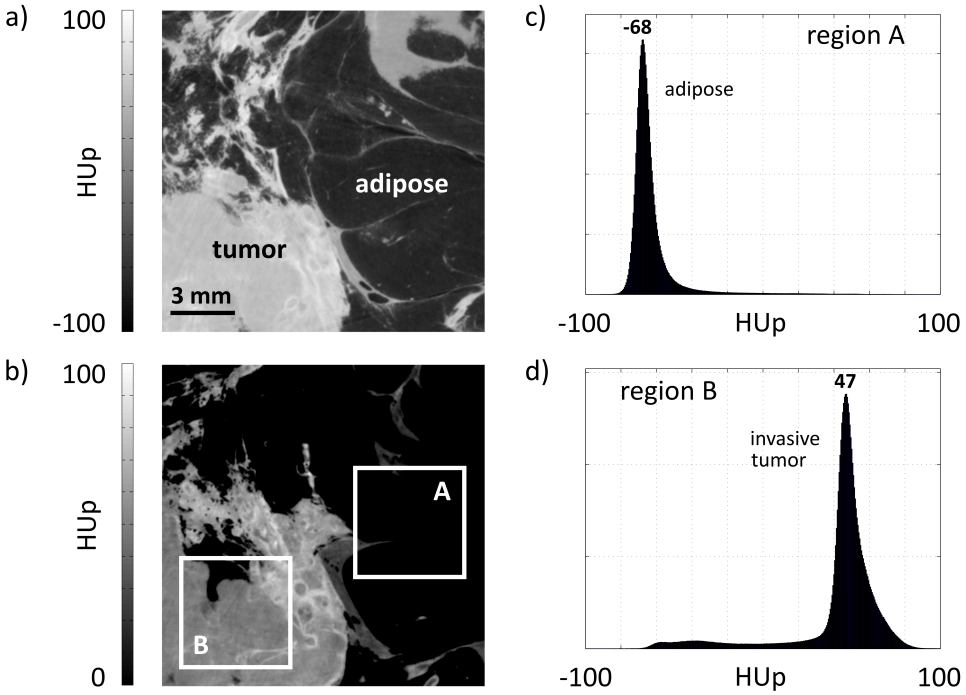

Figure 7.2: Two exemplary tomographic phase-contrast images displaying adipose tissue and an invasive ductal carcinoma, which contains bright circular ductal structures (a and b). The histograms of two cubic regions representing adipose tissue (c) and tumor tissue (d) show distinct peaks with maxima at −68 HUp and 47 HUp, respectively. [Figure adapted from Willner et al. (2014).]

which is about 20 HUp lower than fibroglandular tissue. Moreover, a gentle slope towards higher HUp values can be recognized, which represents the bright signal of the dilated ducts.

To cope with the different sizes of the observed tissue structures, 24 small ROIs (10×10 pixels) were chosen for each type (adipose tissue, fibroglandular tissue, invasive tumor, and ducts) to evaluate and assign quantitative HUp values. The mean values of all considered pixels and the associated standard deviations (std) are listed in Table 7.1. The determined values for adipose, fibroglandular, and tumor tissue are −68.7 (2.7) HUp, 65.2 (6.0) HUp, and 47.0 (2.8) HUp, respectively. They are in good agreement to the peak maxima in the histograms in Figures 7.1 and 7.2. The highest value of 72.5 (5.0) HUp was found for the ducts. Image noise within a homogeneous area of the surrounding formalin solution was around 2.4 HUp. The exceeding standard deviations in the analysis of fibroglandular tissue and ducts (6.0 HUp and 5.0 HUp) suggest higher variances in the actual tissue compositions.

Histological workup of the first sample that was examined at the laboratory

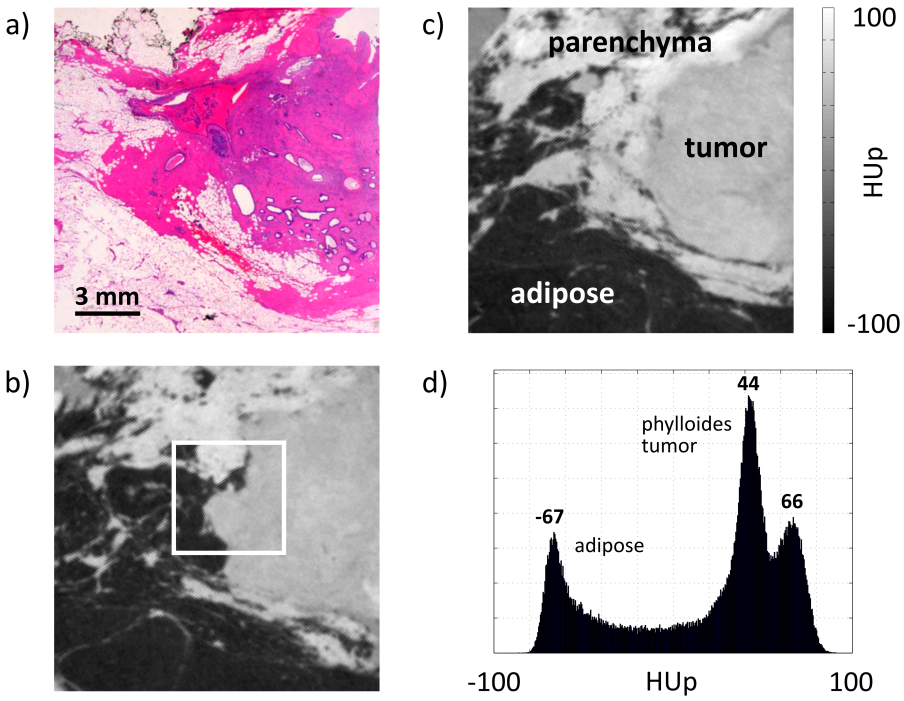

Figure 7.3: Histological slice in H&E-staining (a) and two correlated phase-contrast images (b and c) of a benign phylloides tumor that is surrounded by adipose and fibroglandular tissue. The three peaks in the histogram (d) of a cubic region, which covers all three tissue types, resemble the HUp values that were previously obtained at the synchrotron: adipose tissue between −70 HUp and −65 HUp, tumor tissue around 45 HUp, and fibroglandular tissue at about 65 HUp. [Figure adapted from Willner et al. (2014).]

phase-contrast imaging setup revealed a benign phylloides tumor surrounded by adipose tissue and healthy parenchyma. An exemplary histological slice in hematoxylin eosin (H&E) staining and two representative phase-contrast images are displayed in Figures 7.3a–c. The benign phylloides tumor is well-defined and can be clearly discriminated from adipose and fibroglandular tissue. A cubic region of 0.5 cm side length (50×50×50 voxels, marked in Figure 7.3b) that covers all three tissue types was chosen to analyze the associated phase-contrast Hounsfield units. The corresponding histogram in Figure 7.3d displays three peaks with maxima at −67 HUp, 44 HUp, and 66 HUp. They can be attributed to adipose, tumor, and fibroglandular tissue, respectively. These results are well consistent with the findings at the synchrotron. Despite the varying type of tumor, again, a difference of about 20 HUp between tumor and fibroglandular tissue can be observed. However, the two peaks are not completely resolved and intermediate values exist.

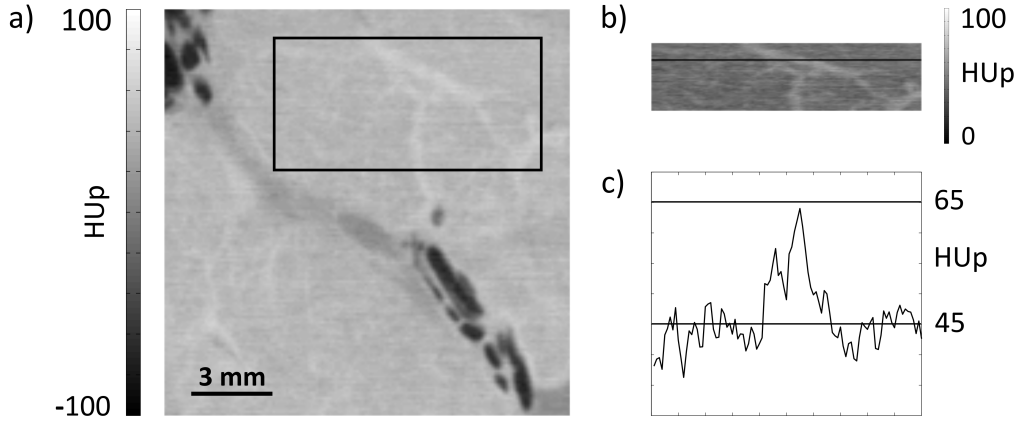

Figure 7.4: Phase-contrast imaging results of a benign fibroadenoma (a). A narrowed window scaling (b) reveals fine bright structures, which can be assigned to fibrous strands in histology. Like the other tumor types before, fibroadenoma features quantitative values around 45 HUp. The high values in the line plot (c) correspond to the fibrous strands. [Figure adapted from Willner et al. (2014).]

The phase-contrast image in Figure 7.4a shows a benign fibroadenoma as confirmed by histopathology. The mean phase-contrast Hounsfield unit of the marked area (50×100 pixels) is 45.1 (5.2) HUp and, thus, is in the same range as the tumor types that were described before. The standard deviation of 5.2 HUp is larger than the actual image noise of about 2.5 to 3.0 HUp. The reason for the higher deviation are thin bright structures within this area. They become visible, when choosing a narrowed window scaling (Figure 7.4b). These features reach values of up to 65 HUp as illustrated in the line plot in Figure 7.4c. In histology, they were related to fibrous strands pervading the fibroadenoma.
The third sample that was investigated at the laboratory setup comprises an infiltrating lobular carcinoma, which is one of the most difficult breast tumors to diagnose. Histological slices thereof in H&E-staining and elastica van gieson (EvG) staining are presented together with a correlated phase-contrast image in Figure 7.5. Two small ROIs are marked within the pictures. Region A can be assigned to lobular carcinoma, whereas region B contains none or only a few tumor cells, but mainly fibrous tissue. The mean phase-contrast Hounsfield units of these two areas account for about 52 HUp and 68 HUp, respectively. The standard deviations are around 4.5 HUp. The resulting contrast-to-noise ratio of the two regions is 3.1, which allows for a differentiation between the specified tissue types.

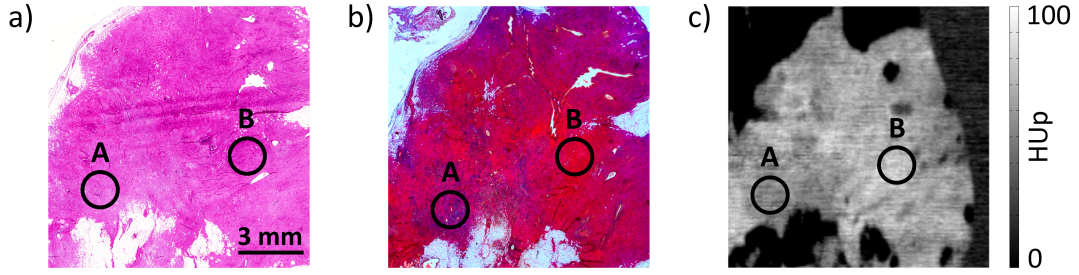

Figure 7.5: Two histological slices in H&E-staining (a) and EvG-staining (b) that display an infiltrating lobular carcinoma. A correlated phase-contrast image is shown in (c). Region A contains many tumor cells, while region B represents mainly fibrous tissue. The two areas can be distinguished by their mean phase-contrast Hounsfield units of 52 HUp and 68 HUp. [Figure adapted from Willner et al. (2014).]

7.3 Comparison to literature values

For a comparison to previously published breast tissue properties, phase-contrast Hounsfield units were calculated from the elemental compositions and corresponding mass densities or directly from the given electron densities that were found in literature. All values and the experimental synchrotron results of this study are listed in Table 7.1. Woodard & White (1986) specified three different sets of properties for each tissue. They represent the mean of the included data (denoted as W&W 2) and the mean plus/minus the standard deviation (W&W 1 and 3). Overall, a wide spread of values can be noticed, ranging from about −70 HUp to almost 80 HUp. The reference values in the literature for adipose and tumor tissue are more consistent than those for fibroglandular tissue. The value of −68.7 HUp that was quantified for adipose tissue in the synchrotron measurement is in very good agreement to the values that were derived from the tabulated tissue compositions. In case of the data quoted from Woodard and White (W&W), this applies to the lowest of the three values. With exception of Shrimpton (1981), the results obtained by Compton scattering methods tend to be somewhat higher (around −40 to −30 HUp). The results of Al-Bahri & Spyrou (1998) have previously been criticized to be inaccurate due to freeze-drying of the samples ahead of the measurements and the lack of essential corrections for background, multi-scattering, and self-attenuation (Ryan et al. 2005, Antoniassi et al. 2010). This might explain the large discrepancies of their results for adipose tissue.
The value of 65.2 HUp that was experimentally evaluated for fibroglandular tissue exceeds most reference values, but is close to the higher value of the data from W&W and the HUp that was calculated from the electron density determined by Antoniassi et al. (2010). The values that were observed for the tumor tissues

Table 7.1: Phase-contrast Hounsfield units of adipose, fibroglandular, tumor tissue, and ducts that were obtained at synchrotron measurements. They are compared to calculated values from previously published tissue properties.

Tissue type:	adipose	fibro-glandular	tumor [ducts]
This study	−68.7 (2.7) HUp	65.2 (6.0) HUp	47.0 (2.8) HUp [72.5 (5.0) HUp]
Tissue composition:			
Hammerstein (1979)	−71.2 HUp	30.9 HUp	
W&W 1 (1986)	−67.7 HUp	−13.0 HUp	
W&W 2 / ICRU	−48.8 HUp	14.4 HUp	
W&W 3	−30.4 HUp	50.7 HUp	
Poletti (2002)	−70.8 HUp	22.7 HUp	
Compton scattering:			
Shrimpton (1981)	−71.9 HUp	18.0 HUp	
Al-Bahri (1997)	36.8 HUp	42.5 HUp	67.1 HUp
Ryan (2005)	−29.9 HUp		56.9 HUp
Antoniassi (2010)	−29.9 HUp	56.9 HUp	77.8 HUp
Antoniassi (2012)	−38.9 HUp		41.9 HUp

in the phase-contrast measurements of the previous section are in line with the findings made by applying Compton scattering.
The most likely reason for discrepancies between the phase-contrast imaging results and the numbers that are stated in the literature is the high spatial resolution of the phase-contrast measurements. This enables a clear distinction between certain tissue types like fibroglandular and adipose tissue. In the other studies, the results rather reflect the average of volumes with side lengths of a few millimeters. The histogram displayed in Figure 7.1d, which represents the HUp-distribution within a cubic region of 0.5 cm side length covering as much fibroglandular tissue as possible, clarifies this assumption. The mean value of this volume amounts to 10.5 HUp and is significantly lower than the value attained for *pure* fibroglandular tissue, which is due to the remaining adipose tissue within this volume. The three considerably differing phase-contrast Hounsfield units that are based on the tissue compositions of W&W and the high standard deviations stated by Ryan (2005) and Antoniassi (2010 and 2012) further indicate the great variance of values that arises from an insufficient spatial resolution and the presence of both adipose and fibroglandular tissue within the samples.
The tumor tissue exhibits around 45 HUp in the phase-contrast measurement and, thus, has a lower value than fibroglandular tissue. This is in contrast to the Compton scattering measurements, where the highest values are obtained for tumor tissue. Once again, this inconsistency might be caused by the limited spatial

resolution in these experiments. Whereas fibroglandular tissue often incorporates portions of adipose tissue, these inclusions are displaced during tumor growth, leading to larger and more homogeneous areas of high density.
A similar line of argument, but on a smaller length scale, could explain the lower HUp of tumor tissue compared to healthy parenchyma in the phase-contrast measurements. Fibrous tissue components, such as collagen strands, give rise to increased phase-contrast signals as observed for the dilated ducts. These components are mostly missing on a subpixel length scale within a tumor cell proliferation and might be responsible for the difference in HUp between tumor and fibroglandular tissue. As side note at this point, the conventional Hounsfield units, which were quantified by analyzing exactly the same ROIs of the synchrotron data are 60 HU for fibroglandular tissue, 63 HU for tumor tissue, and 70 HU for the ductal structures. Apparently, the absence of fibrous components in the tumor tissue is in this case outweighed by another effect, presumably by the absence of subpixel-sized adipocytes.
Concerning the use of tissue properties for the calculation of input parameters in simulations or the choice of suitable phantom materials, the study suggests following conclusions: If the electron density of a certain mixture of adipose and fibroglandular tissue is needed, the values of *adipose tissue 1* and *mammary gland 3* published by Woodard & White (1986) should be taken for the interpolation. The actual mean values (*adipose tissue 2* and *mammary gland 2*), which are also quoted in the ICRU report 44, are seemingly no good representatives as they already comprise fractions of the respective other tissue type. The tissue compositions and densities of Hammerstein et al. (1979) and Poletti et al. (2002) deliver quite adequate values as well. Their fibroglandular tissue, however, might have contained small amounts of adipose tissue as the corresponding HUp appear a little bit too low.
Tumor tissue seems to have values around 45 to 50 HUp ($\rho_\mathrm{e} = 349$–$351\,\mathrm{e/nm^3}$) according to the conducted phase-contrast measurements. This is the case for all investigated tumor types, the malignant ductal and lobular carcinomas as well as the benign phylloides tumor and fibroadenoma. Whereas it is not possible to discriminate between malignant and benign tumor cells by quantitative numbers alone, the morphological information revealed by differences in fibrous and less fibrous tissue values as well as the appearance and shape of fibrous strands or dilated ducts might allow for tumor identification. However, the examination of more samples is necessary to understand the fingerprints of certain tumor types and clarify the potential diagnostic value of phase-contrast CT. The results acquired at this stage implicate that a dose-compatible phase-contrast breast CT or a phase-contrast system for the examination of biopsy samples should be able to resolve at least 15–20 HUp for a potential diagnostic benefit.

Chapter 8

Advanced tissue analysis

8.1 Lipid, protein, and water contents

Lipid, protein, and water are major components of biological tissues and other organic materials. Their concentrations play an important role in medical research and diagnosis as they are crucial parameters that can reflect the progress of diseases.

The concentrations of lipid, protein, and water can for example provide insight regarding tissue functional changes associated with the appearance, progression, and treatment of breast cancer. The water content of tumors is nearly two-fold greater than that of normal tissue, and the lipid content is reduced by about 45 % (Tromberg et al. 2005). The amount of collagen, a major stromal protein, increases in all abnormal breast tissues (Haka et al. 2005).

Hepatic steatosis is characterized by an abnormal accumulation of lipids within the liver. This is the earliest manifestation and hallmark of non-alcoholic liver disease, which has a prevalence of approximately 20–30 % in the adult population (Schreuder et al. 2008). The disease may further progress into cirrhosis and liver failure. Several studies have shown that fibrosis, an excess deposition of extracellular matrix components including collagen, is a strong predictor of further progression to cirrhosis (Wynn 2008, Farrell & Larter 2006).

Traditionally, laboratories have depended on a wide range of chemical analysis techniques to measure the levels of lipid, protein, and water. The Kjeldahl procedure for protein content and the Gerber or Rose-Gottlieb method for fat content are accurate and reliable, but are time-consuming and destructive methods for analysis (O'Sullivan et al. 1999). The reference standard for tissue characterization in a clinical setting is histopathology. Biopsy specimens are taken from a patient, fixed in paraffin, and sectioned into thin slices. Various staining methods and subsequent visual assessments by light microscopy allow the pathologist to grade breast cancer, evaluate the degree of steatosis, or stage fibrosis (Elston & Ellis 1991, Kleiner et al. 2005, Afdhal & Nunes 2004). The disadvantages of

histopathology are its invasiveness, observer-dependence, and the subjective estimation of the concentration of lipids or proteins, such as collagen, within the tissue.
Diffuse optical spectroscopy and Raman spectroscopy have generated considerable interest for non-invasive or minimally-invasive diagnosis of a variety of breast pathologies and for monitoring the therapeutic response in tumor treatment (Haka et al. 2005, Tromberg et al. 2005, Cerussi et al. 2007). Like histopathology, the technique is subject to sampling variability, because only small fractions or portions of the sample under investigation can be analyzed at a given time. For this reason, quantitative 3D imaging approaches, such as MRI or X-ray CT, are generally preferable for specific applications and examinations because they provide full spatial coverage.
Advanced MRI techniques allow the separate depiction of the water and fat components at any site of the human body (Machann et al. 2003). These techniques exploit the difference in resonance frequencies between water and fat proton signals to quantitatively measure the proton density fat-fraction. This is a fundamental tissue property and a direct measure of fat content. MRI techniques currently under development have demonstrated high potential for the accurate detection and quantification of hepatic steatosis (Reeder et al. 2011, Ligabue et al. 2013). When compared to histopathology, MRI is less time-consuming and allows the non-invasive evaluation of the entire liver parenchyma, resulting in a more complete assessment of liver-fat content.
CT can visualize the distribution of fat and the degree of steatosis can be semi-quantitatively estimated (Frisullo et al. 2009, Reeder et al. 2011). In the absence of lipids, the contrast between various tissue types is very low and no conclusions regarding water or protein concentration can be drawn. However, previous studies have shown that phase-contrast imaging in combination with conventional attenuation-contrast CT can open new possibilities for enhanced tissue segmentation (Nielsen et al. 2012, Einarsdóttir et al. 2014). In this chapter, the great potential of phase-contrast CT for advanced tissue characterization is demonstrated by assessing the chemical composition of tissues in terms of water, lipid, and protein contents in each 3D voxel. The results, figures, tables, and text parts have been published in *Quantitative three-dimensional imaging of lipid, protein, and water contents via X-ray phase-contrast tomography* (Willner et al. 2016).

8.2 Vector decomposition

Exemplary attenuation-contrast and phase-contrast images that show an axial slice through one of the porcine fat and rind samples of Chapter 6 are displayed in Figures 8.1a and 8.1b. The complementarity of the imaging signals becomes clearly apparent in the collagen-rich rind (uppermost feature), which provides high values in phase contrast, but is rather unremarkable in attenuation con-

trast. The latter, on the other hand, achieves good contrast for fatty tissue (dark regions), as is commonly known from medical CT imaging. This implies that an advanced tissue characterization with respect to protein or lipid content might be possible when combining both contrast modes.
For a more systematic investigation of the issue, theoretical (conventional) HU (Equation 6.1) and (phase-contrast) HUp (Equation 6.2) were calculated for fictive tissues with varying protein and lipid volume fractions. The remaining unaccounted for volume fraction of up to 100 % was assumed to be water. For a mixture of density ρ_{mix} that consists of several chemical elements i, the linear attenuation coefficient μ_{mix} is given by

$$\mu_{\mathrm{mix}} = \rho_{\mathrm{mix}} \cdot \sum w_i \cdot \frac{\mu_i}{\rho_i}, \tag{8.1}$$

where w_i, μ_i, and ρ_i are the weight fraction, the linear attenuation coefficient, and the density of the i-th element, respectively. The corresponding refractive index decrement δ_{mix} can be determined according to

$$\delta_{\mathrm{mix}} = \frac{r_0 h^2 c^2}{2\pi E^2} \cdot \rho_{\mathrm{mix}} \cdot \sum \left(w_i \cdot N_{\mathrm{A}}/A_i\right) \cdot Z_i, \tag{8.2}$$

using the classical electron radius r_0, the speed of light c, the (effective) energy E of the X-rays, Avogadro's number N_A, and the elements' atomic masses A_i and atomic numbers Z_i (Herzen et al. 2009). The formula is valid for energies far above any absorption edges as it is the case in the present study. For the calculations of HU and HUp values of mixtures with varying protein (p), lipid (l), and water (w) concentrations, the densities ρ_{mix} and weight fractions $w_{i,\mathrm{mix}}$ were obtained by

$$\rho_{\mathrm{mix}} = p \cdot \rho_{\mathrm{p}} + l \cdot \rho_{\mathrm{l}} + w \cdot \rho_{\mathrm{w}} \tag{8.3}$$

and

$$w_{i,\mathrm{mix}} = \frac{\rho_{\mathrm{p}}}{\rho_{\mathrm{mix}}} \cdot w_{i,\mathrm{p}} + \frac{\rho_{\mathrm{l}}}{\rho_{\mathrm{mix}}} \cdot w_{i,\mathrm{l}} + \frac{\rho_{\mathrm{w}}}{\rho_{\mathrm{mix}}} \cdot w_{i,\mathrm{w}}. \tag{8.4}$$

The densities ρ_{p}, ρ_{l}, ρ_{w} and elemental compositions in weight fractions $w_{i,\mathrm{p}}$, $w_{i,\mathrm{l}}$, $w_{i,\mathrm{w}}$ of protein, lipid, and water were taken from tabulated data (Woodard & White 1986). The volume fractions p, l, w of protein, lipid, and water were always chosen to represent the entire mixture ($p + l + w = 1$).
The results are presented in the HU-HUp-scatter plot in Figure 8.1c. In the figure, the HUp values associated with phase contrast are plotted on the x-axis and the corresponding attenuation-based HU values are plotted on the y-axis. Obviously, increasing lipid content has a comparably larger effect on the attenuation signal, whereas the phase-contrast signal is more affected by the protein concentration. Therefore, the values of all considered fictive tissue compositions form a triangle, in which every HU-HUp-pair can be associated with exactly one distinct triplet of protein, lipid, and water content ($p/l/w$). Because of the linear

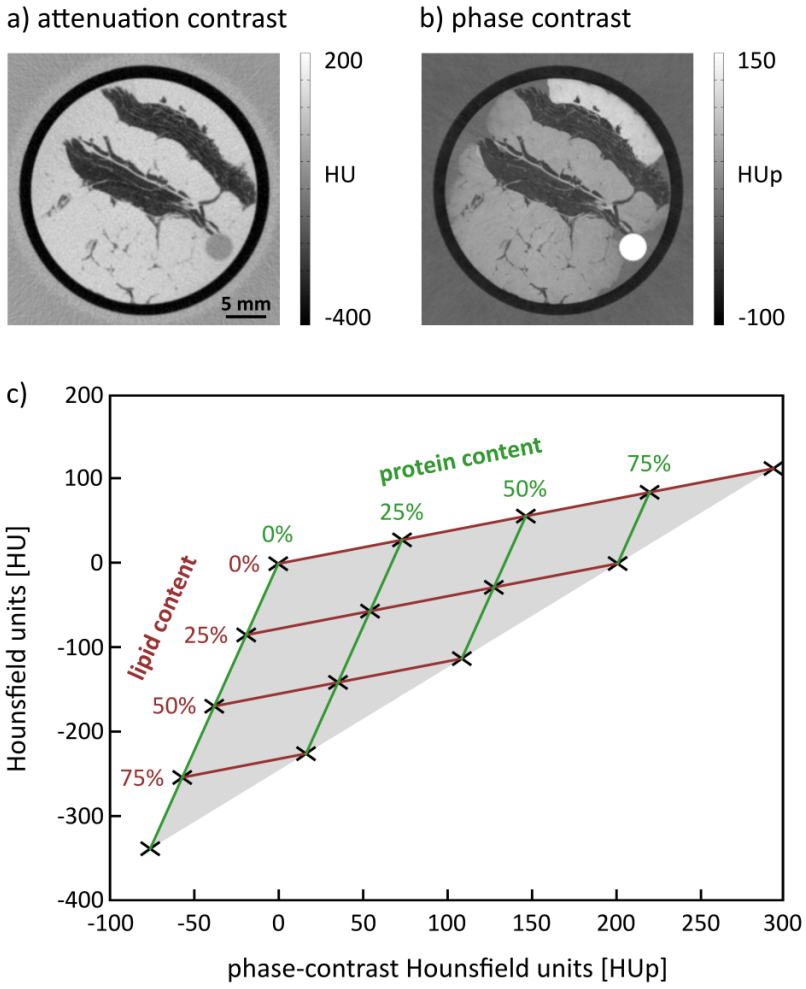

Figure 8.1: Exemplary tomographic imaging results of a porcine fat and rind sample in attenuation (a) and phase contrast (b), respectively. The obtained 3D datasets represent the distribution of the linear attenuation coefficient μ and the refractive index decrement δ within the object and can be converted to quantitative Hounsfield units (HU and HUp). c) Theoretically calculated HU and HUp values for fictive mixtures of varying protein and lipid concentrations. The results span a triangle and every (experimentally evaluated) HU-HUp-pair can be assigned to exactly one specific protein and lipid content. [Figure adapted from Willner et al. (2016).]

increase and decrease in the HU and HUp values with increasing protein and lipid concentrations, every possible mixture can be related to the HU-HUp-pair described by

$$\begin{pmatrix}\mathrm{HUp}\\ \mathrm{HU}\end{pmatrix} = \vec{w} + p \cdot (\vec{p} - \vec{w}) + l \cdot \left(\vec{l} - \vec{w}\right) = \vec{w} + p \cdot \vec{a} + l \cdot \vec{b}, \tag{8.5}$$

where $\vec{w}$, $\vec{p}$, and $\vec{l}$ represent the HU-HUp-pairs of 100 % water, 100 % protein, and 100 % lipid, respectively. Conversely, the contents of protein p and lipid l in a mixture/tissue can be evaluated by the vector decomposition of the experimentally determined HU and HUp:

$$p = \frac{\vec{b}\,(1) \cdot [\mathrm{HU} - \vec{w}\,(2)] - \vec{b}\,(2) \cdot [\mathrm{HUp} - \vec{w}\,(1)]}{\vec{a}\,(2) \cdot \vec{b}\,(1) - \vec{a}\,(1) \cdot \vec{b}\,(2)} \tag{8.6}$$

and

$$l = \frac{\vec{a}\,(1) \cdot [\mathrm{HU} - \vec{w}\,(2)] - \vec{a}\,(2) \cdot [\mathrm{HUp} - \vec{w}\,(1)]}{\vec{a}\,(1) \cdot \vec{b}\,(2) - \vec{a}\,(2) \cdot \vec{b}\,(1)}. \tag{8.7}$$

The missing water fraction is then obtained by

$$w = 1 - p - l. \tag{8.8}$$

8.3 Experimental validation

A first evaluation of the approach was performed using a custom-built phantom consisting of five vials filled with various dairy products (3 types of cream cheese and 2 types of sour cream), which were arranged circularly around a PMMA rod. The contents of lipid (ranging from 0.3 % to 33.8 %), protein (ranging from 2 % to 9.3 %), carbohydrates, and water, as mentioned on the packages, were converted into volume fractions. The resulting values are listed in Table 8.1. The phantom was submerged in a water bath and measured in setup configuration *G* (see Table 4.1). 800 projections were acquired at a tube voltage of 40 kV and a current of 70 mA for the tomographic scan. A projection comprised 11 images that were recorded with exposure times of 3 s. Exemplary images in attenuation contrast and phase contrast are shown in Figures 8.2a and 8.2b, respectively. HU and HUp values for a ROI containing 20×20×4 voxels from each product are plotted in Figure 8.2c. Color-coding reveals that all points corresponding to a given product are grouped around a specific point in the HU-HUp-scatter plot. The dimensions of the point clouds are caused by image noise, which was around 18 HU and 3.5 HUp in the measurement.
The end points of the two vectors $\vec{a}$ and $\vec{b}$ that are required for the decomposition were chosen to be the calculated HU-HUp-pairs of 100 % protein and 100 % lipid.

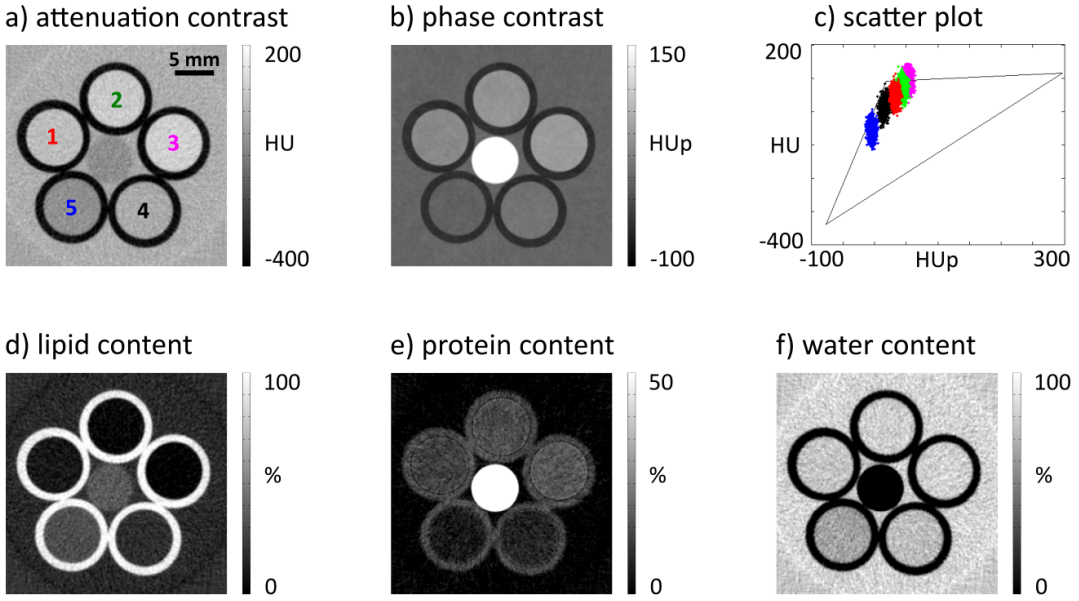

Figure 8.2: Exemplary tomographic attenuation-contrast (a) and phase-contrast (b) images of a test phantom, respectively. They display five vials filled with dairy products (1–3: cream cheese, 4 and 5: sour cream) that are circularly arranged around a PMMA rod. c) The quantitative HU and HUp values of each dairy product group around a certain point in the corresponding HU-HUp-scatter plot according to its protein and lipid content. d–f) Images reflecting the lipid, protein, and water contents of the dairy products generated by the vector decomposition of the attenuation-contrast and phase-contrast data. [Figure adapted from Willner et al. (2016).]

However, their joint starting point was not fixed at 0 HU and 0 HUp (100 % water) to allow for a more flexible data analysis. This becomes necessary to account for influences such as density changes due to organic binders or highly absorbing trace elements within the products. Instead, a dairy product with mid-range lipid and protein contents was used for the calibration. The vector starting points were adjusted to achieve accordance between the analysis results and the product's nutrition table. Carbohydrates (between 2.1 % and 3.1 %) were added to the protein contents in this context and for the validation of the analysis results of the other four products. Decomposed lipid, protein, and water images of the phantom are displayed in Figures 8.2d–f. The lipid image appears generally noisier than the protein image (about 4.3 % versus 1.9 %), because of the major contribution of the attenuation data to the lipid image formation. Mean protein, lipid, and water contents (from the same ROIs as before) are summarized in Table 8.1.
The experimental results show good agreement with the contents stated by the manufacturers. The deviations for the lipid content are only between 0.3 %

Table 8.1: Experimental lipid, protein, and water concentrations (exp.) of the examined dairy products (dp) in comparison to the contents stated by the manufacturers (pack.). Carbohydrates (carb.) stated in the nutrition tables of the packages were counted to the protein content (prot.) for the analysis. [Table adapted from Willner et al. (2016).]

		dp 1	dp 2	dp 3	dp 4	dp 5
lipid content [%]	pack.	0.3	4.7	11.0	16.8	33.8
	exp.	0.6	5.0	11.0	19.9	34.5
protein content [%]	pack. (prot.)	9.3	8.1	7.1	2.1	2.0
	pack. (carb.)	3.0	2.7	2.7	3.1	2.1
	pack. (prot.+carb.)	12.3	10.8	9.8	5.2	4.1
	exp.	14.0	12.1	9.8	6.3	4.5
water content [%]	pack.	87.4	84.5	79.2	78.0	62.1
	exp.	85.4	83.0	79.2	73.8	61.0

and 0.7 % in volume fraction for all dairy products but one, which gave a content of 19.9 % compared to 16.8 %. The protein concentrations differ in the range of 0.4–1.7 % from the actual values. The largest discrepancies (up to 4.2 %) can be observed for the water content.

8.4 Tissue decomposition

As a first biological example, the sample of porcine fat and rind was examined more closely. The sample was placed in a cylindrical falcon tube (⌀ 3 cm) that was filled with PBS and cooled to 4° C during the measurement at a tube voltage of 40 kV in setup configuration *F*. Here, 1200 projections were recorded with 11 images and 3 s exposure time. Attenuation-contrast and phase-contrast images of a section, which contains the three main tissue types (rind, muscle, and fat) are presented in Figures 8.3a and 8.3b, respectively. Small ROIs marked in the rind (blue), muscle (red), and fat (green) can be allocated to distinct points in the HU-HUp-scatter plot (Figure 8.3c), which reflect the different protein and lipid contents of the tissues.
To conduct the decomposition, the measured HU and HUp values of the surrounding physiological PBS solution were taken as the starting point of the vectors. The end points were equivalent to those used in the phantom study. The resulting lipid, protein, and water images are displayed in Figures 8.3d–f. The fatty tissue stands out in the lipid image, whereas rind and muscle scarcely contain any lipids. The higher amount of collagen in the rind is evident in the protein image. Some filaments at the interfaces between fat and muscle are also visible as brighter protein signals. The highest water content is found in the muscle.

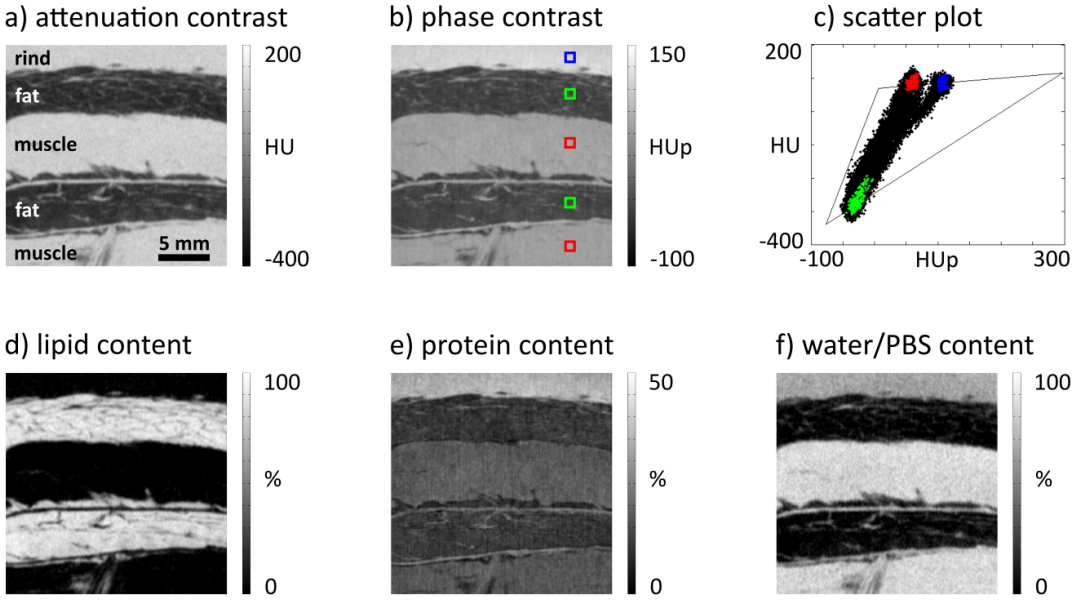

Figure 8.3: Tomographic attenuation-contrast (a) and phase-contrast (b) imaging results, respectively, of a porcine tissue sample covering rind, fat, and muscle. c) Values of the ROIs that are marked within the different tissue types are clearly separated in the HU-HUp-scatter plot. d–f) Decomposed lipid, protein, and water images reveal the high lipid content of the fat, the increased protein (collagen) content in the rind, and the high water concentration of the muscle. [Figure adapted from Willner et al. (2016).]

The second biological sample was taken from the human tissue study in Chapter 6 and comprised four soft-tissue types (adipose/fatty tissue, muscle, skin, and tendon). The tissues were placed in a falcon tube with PBS and cooled during the scan. Figures 8.4a and 8.4b exhibit the obtained attenuation-contrast and phase-contrast imaging results, respectively, for the four tissue types within the plastic cylinder. Panels c–e show the area that is marked by the white box in Figure 8.4b, decomposed into its lipid, protein, and water contents.
The vectors for the decomposition were again defined by the measured HU and HUp values of the PBS and the calculated values for 100 % protein and 100 % lipid. Small ROIs of fat, muscle, and tendon were selected to quantify their respective lipid, protein, and water concentrations. The experimental results are listed in Table 8.2 together with the values reported in the literature for comparison (Woodard & White 1986). Despite the great variety of a tissue's composition in general, the experimental and quoted protein contents are very similar in all the three cases. The differences in volume fraction are only between 0.3 % and 1.1 %. The lipid content of adipose is increased compared to the tabulated content. As a consequence, the water content was determined to be −2.6 %. The

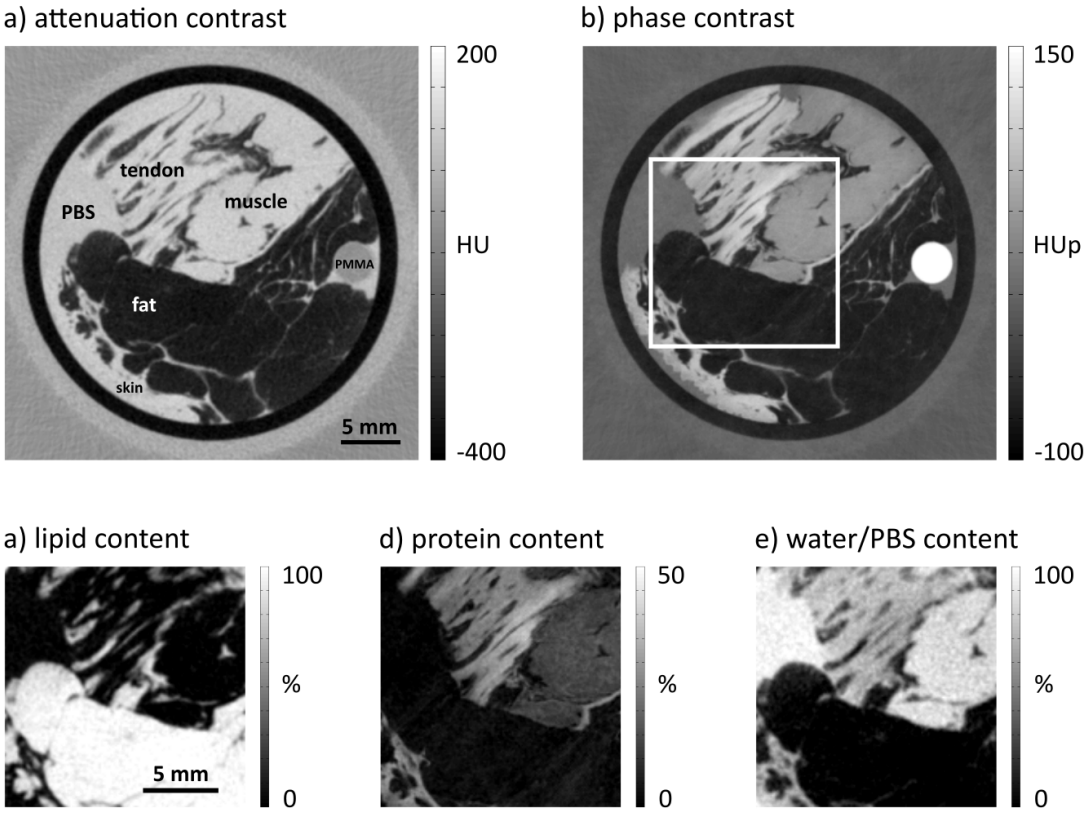

Figure 8.4: Axial tomographic slices in attenuation (a) and phase contrast (b), respectively, through a measured plastic cylinder containing tendon, muscle, fat, and skin tissues. c–e) Decomposed lipid, protein, and water images of the region marked by the white box in (b). [Figure adapted from Willner et al. (2016).]

Table 8.2: Quantitative analysis of the lipid, protein, and water contents (exp.) of human tissue types in comparison to values tabulated in the literature (tab.) (Woodard & White 1986). [Table adapted from Willner et al. (2015).]

		fat	muscle	tendon
lipid content [%]	exp.	99.2	−0.8	0.1
	tab.	76.7	4.9	1.2
protein content [%]	exp.	3.4	15.3	29.3
	tab.	3.1	15.7	30.4
water content [%]	exp.	−2.6	85.5	70.6
	tab.	20.2	79.4	68.2

negative value indicates that a slight modification of the vectors that were chosen for the decomposition is necessary to cover all the data points.
Based on these preliminary but promising results, one can conclude that the high sensitivity of phase-contrast CT and the complementary information provided in addition to conventional attenuation-based imaging allow for enhanced tissue characterization. As demonstrated in this proof-of-concept study, protein, lipid, and water contents within each 3D voxel can be quantified by applying a vector decomposition for the data obtained with both contrast modalities.
Further investigations should address the optimum choice of the utilized vectors and the effect of trace elements on the analysis results. Trace amounts of heavier elements can increase the attenuation signal and affect the extracted lipid content. In the presented phantom study, this issue was mostly addressed by using a single dairy product as a calibration substance and accordingly adjusting the vector starting points. For the biological examples, the consideration of the physiological PBS solution in the definition of the vector starting points accounted for heavier elements. The presence and differences of the manifold types of proteins and lipids have not been examined more closely yet and might have an impact on the correct choice of the vectors. A more comprehensive study alongside with a statistically meaningful analysis is needed to exactly validate the diagnostic specificity of this lipid, protein, and water decomposition technique on a more quantitative basis.

Chapter 9

Further research activities

9.1 Biomedical studies

The core mission during the time of this PhD thesis was the realization of a highly sensitive and reliable laboratory phase-contrast CT system in order to explore the capabilities of phase-contrast imaging for quantitative tissue characterization. In this context, several side projects were carried out, ranging from proof-of-concept measurements at synchrotron radiation facilities to long-term investigations at the laboratory system. The projects included the examination of various tissue types and the experimental assessment of new technical advances. They can be grouped into the two categories *biomedical studies* and *methodical developments*. This chapter is a short review of these research activities, describing their scientific framework and highlighting the publications that arose from these projects.
A large part of the work was done within the *Munich-Centre for Advanced Photonics* (MAP), a cluster of excellence of the *German Research Foundation* (DFG). The main goal of this broad research collaboration is the enhancement of laser technology and state-of-the-art photonic tools to push the frontiers of biomedical and information technologies. One area of research is the application of novel laser-driven X-ray sources and new X-ray imaging modalities for biomedical diagnosis and the early detection of cancer and chronic diseases. This includes the evaluation of phase-contrast imaging in different relevant settings to identify the clinical indications with the highest diagnostic yield and to explore the additional diagnostic possibilities that are gained. For this purpose, several studies have been conducted at the highly sensitive phase-contrast imaging setup in cooperation with the *Department of Clinical Radiology* (*Ludwig-Maximilians-Universität München*).
The main results of the activities that concerned tomographic examinations of breast tissues were presented in Chapter 7 and are published in *Quantitative breast tissue characterization using grating-based X-ray phase-contrast imaging* (Willner et al. 2014). Further imaging results are discussed in *Evaluation of phase-contrast*

CT of breast tissue at conventional X-ray sources – presentation of selected findings (Grandl et al. 2013) and demonstrate the high potential of phase contrast compared to conventional attenuation contrast. Differences in contrast between fibrous and less fibrous breast tissue could be observed in the phase-contrast but not in the attenuation-contrast images. In addition, regions of low phase contrast correlated with the extension of compact tumor components. The study *Visualizing typical features of breast fibroadenomas using phase-contrast CT: an ex-vivo study* (Grandl et al. 2014) further concludes that a successful translation of the technology to a clinical setting may contribute to the reduction of false-positive findings and reduce the recall and core biopsy rate in population-based screening. A greatly improved differentiation of fine structures like fibrous strands or diagnostically valuable dilated ducts is shown in the publication *Assessment of grating-based X-ray phase-contrast CT for differentiation of invasive ductal carcinoma and ductal carcinoma in situ in an experimental ex vivo set-up* (Sztrókay et al. 2013). While this early study was performed at a synchrotron, the imaging results from the laboratory system confirm the capability to depict the 3D structure of dilated ducts as high phase-contrast signals could be successfully correlated to thickened fibrous ductal walls. The current work focuses on the possible differentiation between invasive carcinoma, intraductal carcinoma, and healthy breast tissue at the laboratory to evaluate the potential of phase-contrast CT for assistance during histopathological workup.

Another key topic for the evaluation of phase-contrast imaging within the MAP collaboration is the characterization of atherosclerotic plaque. Cardiovascular and cerebrovascular diseases remain two of the leading causes of death in both developed and developing countries (Lloyd-Jones et al. 2010). CT is today's backbone of whole body vascular imaging due to fast and robust data acquisition. Despite significant technical progress in the last decades, clinical CT imaging is limited to lumenography and cannot reliably differentiate between different plaque components like fibrous tissue, lipid, and intraplaque hemorrhage due to low soft-tissue contrast and a significant overlap in Hounsfield units (U-King-Im et al. 2010, Wintermark et al. 2008). Plaque material and structure play a pivotal role for the risk of subsequent cardiovascular events like stroke. While a large, lipid-rich necrotic core and intraplaque hemorrhage covered by a thin layer of fibrous tissue, the so-called fibrous cap, can be associated with plaque instability and rupture, plaques consisting of fibrous, collagen-rich tissue are considered to be stable and are less likely to cause complications (Naghavi 2003*a*,*b*).

First results of this project that were obtained at the beamline *ID19* of the ESRF and at the laboratory phase-contrast imaging setup are presented in *Translation of atherosclerotic plaque phase-contrast CT imaging from synchrotron radiation to a conventional lab-based source* (Saam et al. 2013). This proof-of-principle study shows that phase-contrast CT of carotid specimens is suitable for vessel characterization and atherosclerosis research due to its enhanced soft-tissue contrast.

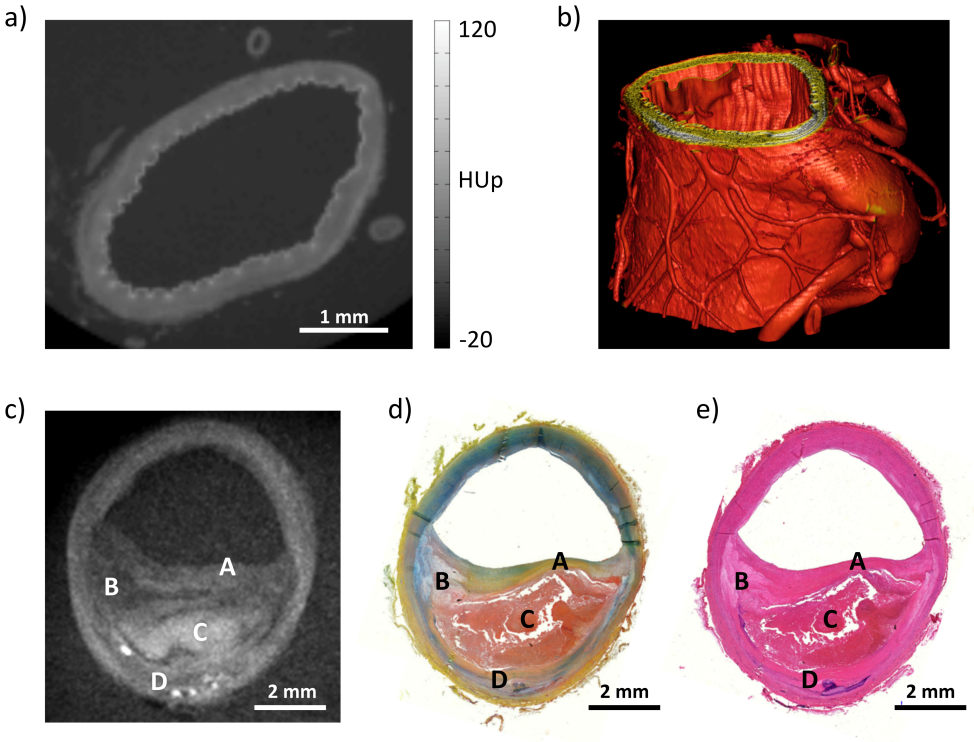

Figure 9.1: Imaging characteristics of human internal carotid arteries in phase-contrast CT. a) Phase-contrast image of a healthy artery measured with synchrotron radiation showing the three vessel layer. The tunica media appears darker than the outer and inner layer. b) 3D rendering of the synchrotron results. c) Phase-contrast image of a complicated atherosclerotic plaque in the common carotid artery obtained at the laboratory system. d) and e) Histopathologic sections stained with Movat pentachrome and H&E, respectively. Fibrous cap (A) overlying the necrotic core (B) with intraplaque hemorrhage (C) and areas of calcifications (D) can be clearly visualized by using phase-contrast CT.

Both experimental setups generated images that allowed for the differentiation of the tunica intima and tunica media (two layers of the vessel wall, see Figure 9.1a). The detection of high-risk atherosclerotic plaque components, such as the fibrous cap and the lipid/necrotic core, was possible. Following these encouraging results, more samples were examined at the laboratory system to further evaluate the potential for atherosclerotic plaque imaging in human carotid arteries. The corresponding publication *Phase-contrast CT: qualitative and quantitative evaluation of atherosclerotic carotid artery plaque* (Hetterich et al. 2014) concludes that phase-contrast imaging can help to identify and quantify atherosclerotic plaque components with excellent correlation to histopathologic findings and may become a valuable tool to monitor the atherosclerotic disease process non-invasively. An exemplary phase-contrast imaging slice through a carotid artery

with complicated atherosclerotic plaque is displayed in Figure 9.1c. All features like the fibrous cap, intraplaque hemorrhage, necrotic core, and calcifications can be matched to the histopathologic workup of this section (Movat pentachrome and H&E-staining, see Figures 9.1d and 9.1e). The phase-contrast datasets at that point were obtained in setup configuration *A* (see Table 4.1). A higher quality example image, which was acquired in the more recent setup configuration *G*, can be found in Figure 5.3a of Chapter 5.

Phase-contrast Hounsfield units of different plaque components were quantified from high-resolution synchrotron data and are discussed in *Grating-based X-ray phase-contrast tomography of atherosclerotic plaque at high photon energies* (Hetterich et al. 2013). High HUp values can be found in regions with a high density of elastic and collagen fibers like healthy intima, healthy adventitia, and densely packed fibrous tissue (> 50 HUp). Regions of only smooth muscle cells in absence of any elastic or collagen fibers and other regions with little connective tissue like lipid/necrotic core or inflammatory cell infiltration show lower HUp values (< 50 HUp). Intraplaque hemorrhage gives values between 50 HUp and 80 HUp. The differentiation between fibrous and lipid-rich tissue in terms of HUp at the laboratory system is demonstrated in *X-ray phase-contrast computed tomography of human arteries* (Hetterich et al. 2015a). The mean HUp values of fibrous tissue (61.7 HUp) and lipid-rich tissue (39.9 HUp) were analyzed from a total of 15 coronary arteries and are within the same range as in the synchrotron study.

The *Committee on Vascular Lesions* of the *American Heart Association* (AHA) suggested an international histopathology classification system to differentiate atherosclerotic plaques according to precisely defined morphology and tissue criteria (Stary 2000). This AHA classification was successfully modified for imaging purposes later. The results published in *AHA classification of coronary and carotid atherosclerotic plaques by grating-based phase-contrast computed tomography* (Hetterich et al. 2015b) indicate that phase-contrast CT can reliably classify atherosclerotic plaques according to modified AHA criteria with excellent agreement to histopathology and high diagnostic accuracy. The superior soft-tissue contrast holds promise to provide comprehensive information on plaque morphology that is currently not available using other imaging modalities.

Further ongoing research projects within the MAP cluster of excellence are the evaluation of phase-contrast CT for the depiction of structural changes in different heart diseases and for the characterization of renal cell carcinoma subtypes.

Another close collaboration partner for biomedical research in the course of this thesis was the *Department of Diagnostic and Interventional Radiology* (*Technische Universität München*). One research focus within this cooperation is on phase-contrast imaging of liver lesions. The synchrotron study *Evaluation of the potential of phase-contrast computed tomography for improved visualization of cancerous human liver tissue* (Noël et al. 2013) shows improved pathological

and morphological information. Especially the tumor capsule and the vascular structures are very good visible. Phase-contrast imaging results of various liver specimens with cancerous tissue that were recorded at the laboratory system can be found in *Imaging liver lesions using grating-based phase-contrast computed tomography with bi-lateral filter post-processing* (Herzen et al. 2014). Tumor boundaries can be again depicted and soft-tissue structures like fibrous septa or necrotic and hemorrhagic areas can be distinguished. Current examinations are done concerning the possibilities of grading and staging liver fibrosis and cirrhosis. In addition, human pancreas samples are investigated, since previous observations on a genetically engineered mouse model of pancreatic ductal adenocarcinoma, which were presented in *X-ray phase-contrast CT of a pancreatic ductal adenocarcinoma mouse model* (Tapfer et al. 2013), gave promising results in this direction. Many CT scans of different kinds of bodily fluids were performed at the laboratory setup in cooperation with the *Department of Diagnostic and Interventional Radiology*. In the thesis *Quantitative X-ray phase-contrast imaging for the differentiation of bodily fluids* by Henningsen (2014), phase-contrast Hounsfield units were determined for protein samples of bovine serum albumin diluted with water to create protein concentrations ranging from 5 % to 30 %. Three different human blood samples were measured, two of which were treated with an anticoagulant (sodium citrate or EDTA) to prevent clotting. The protein samples showed nearly linearly increasing values from 10 HUp to about 50 HUp. The two treated blood samples were completely sedimented at the time of their measurements and the serum component could be differentiated from the cellular components. The serum gave values of about 25 HUp, whereas the sedimented blood cells had values around 60 HUp to 65 HUp. The clotted blood of the third sample reached values of nearly 80 HUp, which correlates to the phase-contrast Hounsfield units observed for intraplaque hemorrhage in the investigations of atherosclerotic plaque. Different types of pathologic fluid collections were further imaged and compared to clinical chemistry measurements. A discrimination between rather pyic and bloody abscesses (above 15 HUp) and watery lymphoceles (around 10 HUp) was possible.

An extensive phantom study was conducted to explore the potential to enhance the differentiation of cystic renal lesions by phase-contrast CT. There exists a variety of renal lesions ranging from simple cysts, which do not need further attention, to malignant tumors, which require intensive treatment. A classification system for renal cysts has been introduced in 1986 and is well established to estimate the malignant potential of a lesion (Bosniak 1986). Briefly, cystic renal lesions are categorized in four types according to certain imaging characteristics like septations, calcifications, density, wall thickening, nodularity, and contrast enhancement. Type I and II are most likely benign, type IV is almost certainly malignant. The Hounsfield scale allows cystic renal lesions to be classified as simple renal cysts only if the lesion has the attenuation of water. Some cystic

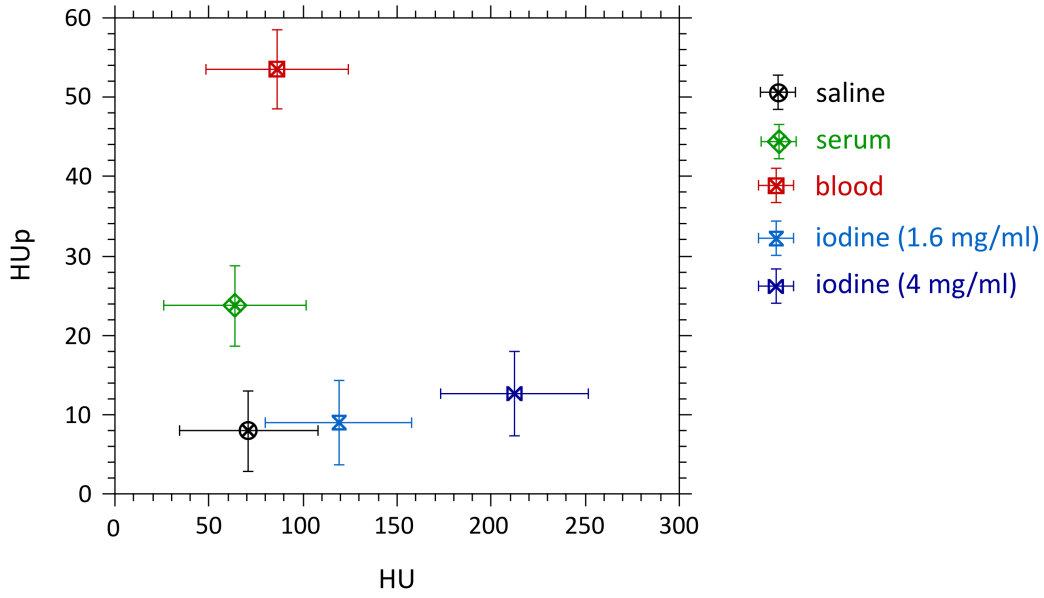

Figure 9.2: HU-HUp-scatter plot showing the quantitative phase-contrast imaging results plotted versus the corresponding quantitative attenuation-based values for different simulated cystic renal lesions. Error bars indicate the standard deviations that were obtained. The combination of both contrast modalities allows differentiation of all types of cystic lesions. [Figure adapted from Fingerle et al. (2014).]

renal lesions, however, show high protein content or undergo interval hemorrhage, leading to increased attenuation. In the presence of hyperattenuating focal renal lesions, contrast enhancement of soft-tissue components may be obscured entirely and malignant transformation might remain undetected. Consequently, renal multi-phasic CT studies that consist of unenhanced and contrast-agent enhanced imaging sequences are used in the clinics to analyze renal enhancement patterns. Whereas this multiphasic imaging approach enables the identification of enhancing soft-tissue nodules, the characterization of hyperattenuating lesions may at time remain difficult and novel methods for iodine detection and protein quantification may have considerable utility (Boll et al. 2010).
Various combinations of saline, serum, blood, and an iodinated contrast agent were used to reproduce the chemical composition of the different types of cysts in the phantom study. Quantitative HU and HUp of all mixtures have been determined from the measurements. Figure 9.2 shows the results of saline, serum, blood, and two iodine concentrations in a HU-HUp-scatter plot. While attenuation contrast allows differentiation of increasing concentrations of iodine, the phase-contrast signal is hardly affected by the contrast agent. A discrimination

of simple and hemorrhagic cysts from enhancing cystic renal lesions is possible by the combination of both imaging modalities. A detailed description of the study is published in *Simulated cystic renal lesions: quantitative X-ray phase-contrast CT – an in vitro phantom study* (Fingerle et al. 2014).

9.2 Methodical developments

One research focus in X-ray grating interferometry are the gratings themselves. The strong collaboration with the *Karlsruhe Institute of Technology* and *microworks GmbH* included several experiments at the laboratory system for the evaluation of latest developments in grating manufacturing. Some aspects like the enhanced quality of the grating structures, the new sunray design to avoid gaps along the grating bars, or the low absorbing carrier substrates to achieve a better photon statistics have already been mentioned in Chapter 4. A promising approach to increase the FOV in phase-contrast CT is the stitching of single grating tiles to produce one large-area grating. First imaging results using a 2×2 stitched analyzer grating were obtained at the laboratory system and are presented in *Increasing the field of view in grating based X-ray phase contrast imaging using stitched gratings* (Meiser et al. 2016). The high and homogeneous visibility of between 30 % and 40 % over the full FOV demonstrates that cutting and assembling of the single tiles can be done within the required precision. The stitching affected only one vertical and horizontal pixel row. The visibility was reduced to approx. 6 % in these inter-grating gaps, but the extraction of all three contrast modalities (attenuation, phase, and dark-field contrast) was still possible as can be seen on the example of a frog in Figure 9.3.
The height of the gratings is another important parameter, which needs to be increased further in order to bring the technique closer to the clinics. One of the first analyzer gratings with an aspect ratio of about 100 was fabricated and provided by the *Karlsruhe Institute of Technology* to assess the feasibility of grating-based phase-contrast imaging at higher energies. The grating with a period of 2.4 µm and gold structures of 100 µm height was used to perform test measurements with monochromatic synchrotron radiation of 82 keV at the beamline *ID19* of the ESRF. At this energy, directly above the absorption edge of gold, the transmission through the grating bars is only 20 %, which enabled to realize an interferometer with a visibility value of 26 %. The corresponding setup is described in *Quantitative X-ray phase-contrast computed tomography at 82 keV* (Willner et al. 2013).
A phantom consisting of well-known materials was designed to investigate the complementarity of attenuation contrast and phase contrast at 82 keV and to compare their image quality in terms of contrast-to-noise ratios. The mass densities of the materials ranged from 1.19 g/cm^3 (PMMA) to 4.5 g/cm^3 (Ti) and the covered elements had atomic numbers up to $Z = 22$ (Ti). A phase-contrast CT

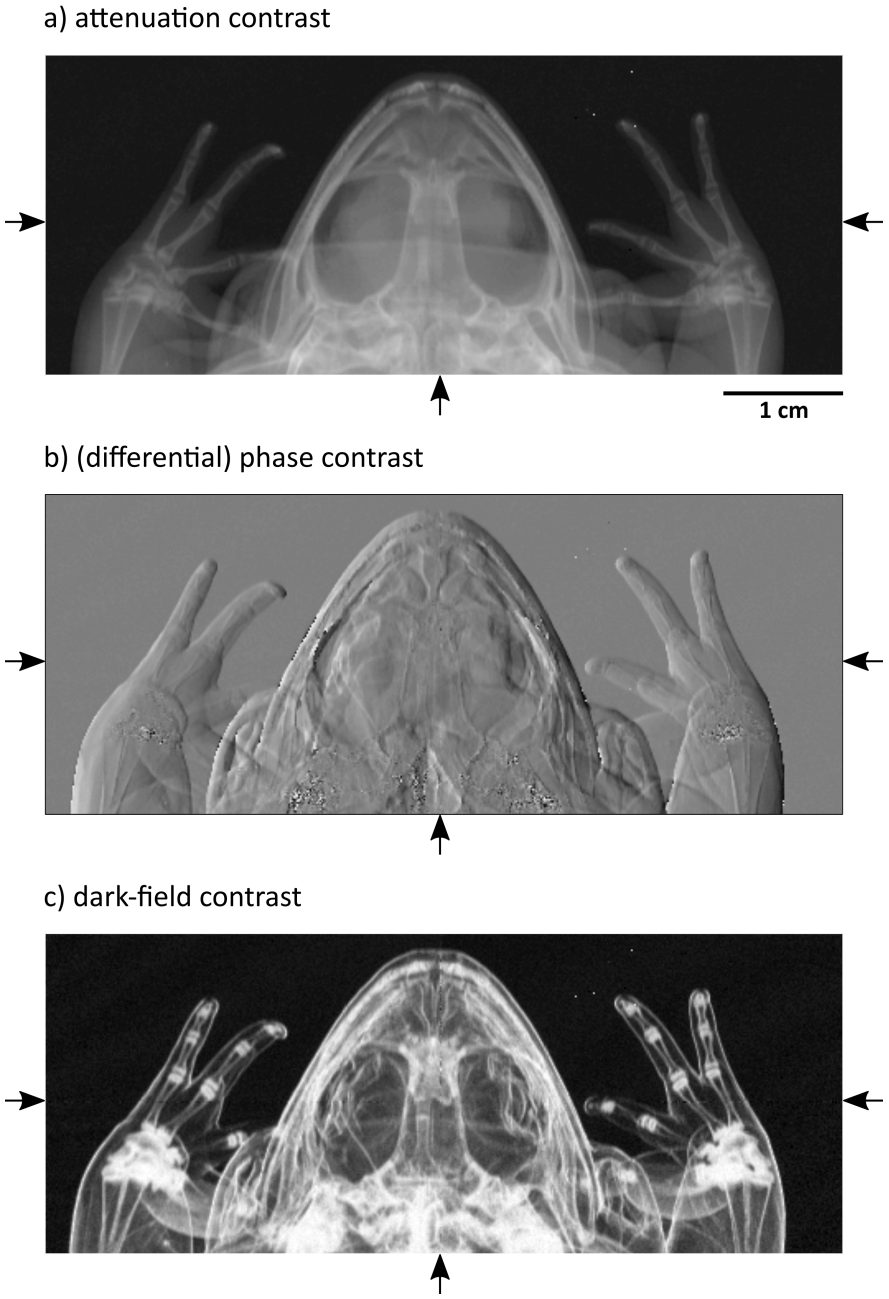

Figure 9.3: Projection images of a frog that were recorded with a 2×2 stitched analyzer grating at the laboratory setup. Images in attenuation contrast (a), phase contrast (b) and dark-field contrast (c) show that the stitching procedure yields only a minor impact on the image quality. The arrows mark the inter-grating gaps. [Figure adapted from Meiser et al. (2016).]

scan of the phantom was executed and the linear attenuation coefficients μ, the refractive index decrements δ, and the electron densities ρ_e were determined. The quantitative values that were evaluated from the measurement are in good agreement with theoretical values. A contrast gain was achieved by phase contrast for all material combinations. Compton scattering is the dominating attenuation process at 82 keV for materials with low effective atomic numbers ($Z < 8$), which include most biological soft tissues. In these cases, the signal of both modalities are proportional to the electron density and their complementarity is lost. The advantage of phase-contrast imaging is then restricted to an enhancement of image quality in terms of contrast-to-noise ratios. However, for materials with higher effective atomic numbers ($Z > 8$), attenuation and phase contrast provide complementary information and conclusions on density and material composition can be drawn as discussed in Chapter 5.

With regard to the human body, this applies in particular to bones and teeth due to the high content of calcium ($Z = 20$). Imaging results of a molar tooth are shown in Figure 9.4. The two main components, enamel and dentin, are well discriminable in both contrast modes. The contrast-to-noise ratio of the two mineralized tissues is around 2 in attenuation contrast and above 10 in phase contrast. To evaluate the potential of a quantitative material characterization, the mass densities ρ and effective atomic numbers have been determined at 50 positions in enamel and 20 positions in dentin. To obtain the respective mass densities ρ, the electron densities ρ_e were divided by the mass electron density (number of electrons per unit mass). The effective atomic numbers were determined by the ratio of Compton scattering to the overall attenuation. The corresponding results are presented in Figures 9.4c–e. The detected mass densities for both enamel and dentin are in the range of values stated in literature. The greater effective atomic numbers that can be observed for enamel compared to dentin represent the higher content of calcium and phosphorus in enamel than in dentin.

By now, even higher grating structures have been produced and X-ray grating interferometry at energies far above 100 keV was demonstrated at the synchrotron (Ruiz-Yaniz et al. 2015a,b). Translation to polychromatic X-ray sources is challenging due to the broad spectral bandwidth at high tube voltages. A laboratory setup that can successfully be operated at 70 kV was installed at the *Department of Physics* (*Technische Universität München*) to image specimens with sizes of up to ⌀ 50 mm. Results from an intervertebral fibrocartilage surrounded by bones to showcase the experimental setup can be found in *Quantitative imaging using high-energy X-ray phase-contrast CT with a 70 kVp polychromatic X-ray spectrum* (Sarapata et al. 2015). The software framework that was introduced in Chapter 5 was further used in this publication to extract quantitative material properties from phantom measurements. Again, there was no additional information content for low-Z materials in phase contrast compared to attenuation contrast. However, phase-contrast imaging provided improved contrast-to-noise

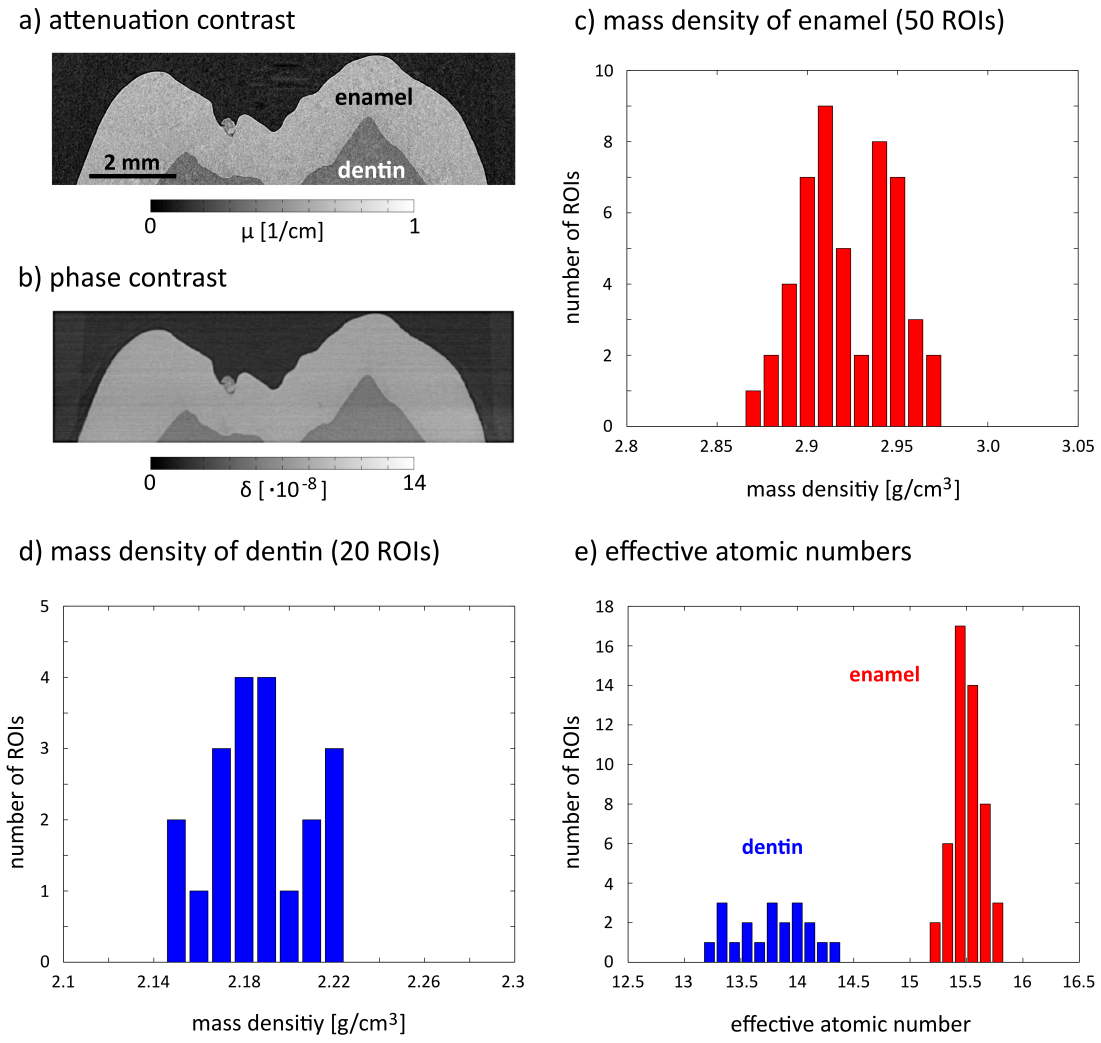

Figure 9.4: Attenuation-contrast (a) and phase-contrast (b) imaging results from a synchrotron CT scan that was performed at an energy of 82 keV. Mass densities ρ that were evaluated at 50 positions in enamel and 20 positions in dentin are presented in (c) and (d), respectively. Effective atomic numbers that were obtained by exploiting both contrast modalities are displayed in (e). [Figure adapted from Willner et al. (2013).]

ratios. In analogy to the synchrotron study, the complementarity of both signals can be seen with increasing effective atomic numbers of the materials and a more comprehensive material characterization becomes possible.
In medical CT systems, a helical scanning procedure is employed to extend the FOV and to reduce measurement time. The patients are translated continuously through the beam, while the gantry (carrying the source and detector) is being rotated around them. A similar approach, in which the sample rotates instead of

the X-ray components, can be applied for long objects in the laboratory phase-contrast imaging setup. First experimental attempts on the helical scanning process for phase-contrast CT were executed and are presented in *Helical differential X-ray phase-contrast computed tomography* (Fu et al. 2014a). The phase-contrast data could be accurately reconstructed. However, as a stepping curve needs to be recorded for each single projection, no continuous sample rotation can be performed. A potential solution is to use the helical motion of the tomographic axis to extend the so-called moiré fringe scanning to the tomographic case as illustrated in Figure 9.5a and briefly described in the following.
Moiré fringe scanning allows for fast data acquisition in radiographic phase-contrast applications such as mammography or in-line product analysis. In this method, the sample is moved over different detector positions instead of performing a translation of the gratings (Kottler et al. 2007). If the reference phase is not constant over the area of the detector, the same region of the sample is recorded at different fringe phases by this scanning approach. Different fringe phases correspond to different relative positions of the gratings in a traditional stepping approach. Therefore, a stepping curve can be obtained by combining these different areas as illustrated in Figures 9.5b and 9.5c. In other words, the stepping process is performed without a translation of the gratings, but is analogous to that obtained with the standard technique. A similar scanning-type system can be realized by upward motion of the tomographic axis during rotation. With this method a continuous helical rotation of the sample or the gantry can be achieved, because no stepping of the gratings is needed. The minimum number of helical rotations corresponds to the number of steps that are planned to be recorded for each projection. For every angle, each section of the sample has to be in the FOV at least three times at different fringe phases. This is necessary, because at least three data points are needed to extract the imaging signals. A detailed description of this approach and a demonstration of its successful implementation are given in *Helical X-ray phase-contrast computed tomography without phase stepping* (Marschner et al. 2016).
Various kinds of datasets were acquired at the phase-contrast imaging setup and provided for the validation of newly developed image processing algorithms. In the thesis *Data processing in grating-based X-ray phase-contrast computed tomography: workflow automation and noise studies* (Marschner 2013), a statistical iterative reconstruction implemented by Hahn et al. (2015) is applied to improve image quality and reduce the number of projection images that need to be recorded. Another approach to decrease the measurement time is a compressed-sensing inspired iterative reconstruction of the phase-contrast CT data as shown in *Iterative reconstruction for few-view grating-based phase-contrast CT – an in vitro mouse model* (Gaass et al. 2013). Further noise-reducing but resolution-preserving reconstruction methods, which aim at boosting the performance of phase-contrast CT, are investigated in *Regularized iterative integration combined*

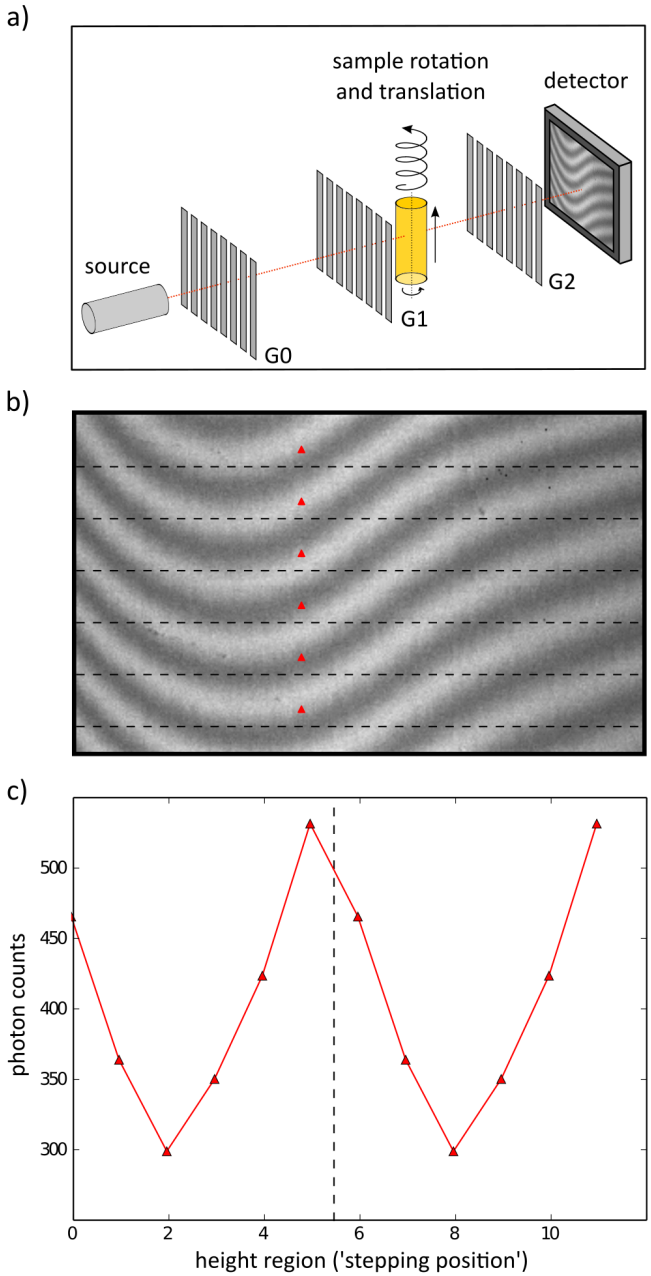

Figure 9.5: a) Illustration of moiré fringe scanning in combination with the upward motion of the tomographic axis during helical data acquisition. b) The interferogram that is recorded by the detector shows moiré fringes, which can be introduced by a deliberate mismatch of the relative positions of the phase grating and the analyzer grating. (c) A stepping curve can be obtained by combining different height regions as exemplarily demonstrated for the pixels marked by the red triangles in (b). [Figure adapted from Marschner et al. (2016).]

with non-linear diffusion filtering for phase-contrast X-ray tomography (Burger et al. 2014). An image-based denoising algorithm that exploits complementary information and noise statistics from multi-modal images is introduced in *Bilateral filtering using the full noise covariance matrix applied to X-ray phase-contrast computed tomography* (Allner et al. 2016). This novel generalized 3D bilateral filter enhances image quality while preserving the edges, when being applied to the attenuation-contrast and phase-contrast images.
An implementation of hybrid fluorescence molecular tomography (FMT) and X-ray phase-contrast CT for the combination of anatomical with functional and molecular contrast in small-animal imaging is presented in *FMT-PCCT: Hybrid fluorescence molecular tomography X-ray phase-contrast CT imaging of mouse models* (Mohajerani et al. 2014). FMT allows for highly sensitive 3D imaging of the distribution of a fluorescent marker in an animal body. However, as a stand-alone technique, it offers only low resolution. The utilization of phase-contrast data as prior information to the fluorescence inversion problem allows for generating optical images of high fidelity and quantification accuracy.
Laminography is an alternative X-ray imaging technique, which is employed for the examination of large but thin objects. Here, the sample is rotated around an axis not normal to the beam path to avoid orientations with large X-ray attenuation. First experiments on laboratory-based phase-contrast laminography were performed at a modified version of the imaging setup and are published in *Cone-beam differential phase-contrast laminography with X-ray tube source* (Fu et al. 2014b).
Although the dark-field contrast has not been discussed in detail within this thesis, because it is an active research field on its own, some contributions were made to this topic. The study *Non-invasive differentiation of kidney stone types using X-ray dark-field radiography* (Scherer et al. 2015) shows that renal calculi like calcium oxalate, uric acid, and mixed types of stones can be differentiated with the additional information content that is gained by X-ray dark-field radiography. A non-biomedical application of the dark-field contrast is the monitoring of moisture in textiles as demonstrated in *Monitoring moisture distribution in textile materials using grating interferometry and ptychographic X-ray imaging* (Esmaeili et al. 2015). Interesting results on dark-field tomography and its capabilities to reveal cracks below the resolution limit of the detector system can be found in *Detection of sub-pixel fractures in X-ray dark-field tomography* (Lauridsen et al. 2015).

Chapter 10

Summary and perspectives

The presented work was carried out in order to advance the application of grating-based X-ray phase-contrast imaging for biomedical research in a laboratory setting. For this purpose, a highly phase-sensitive imaging setup was designed and has been continuously optimized over the years. A wide range of experiments with phantoms and biological specimens were conducted and the capabilities of quantitative tissue characterization have been investigated.
The imaging system combines a rotating-anode X-ray tube, a photon-counting hybrid-pixel detector, and a Talbot-Lau interferometer to extract the phase information. The high photon flux of the source and the absence of classical electronic noise during X-ray detection are the basis for attaining good image quality. The three gratings of the interferometer have periods of 5.4 µm and are spaced at equal distances, because this symmetric configuration is favorable when aiming to resolve small refraction angles. A rather long setup arrangement of around 2 m was chosen to avoid shadowing effects that would otherwise reduce the available FOV. A major challenge in the realization of a highly sensitive phase-contrast imaging system in a laboratory environment is the broad spectral width of the X-ray source. The distances between the gratings and their parameters have to be carefully adjusted to the effective source spectrum. A π-shifting phase grating is generally preferable to a $\pi/2$-shifting phase grating at large propagation distances as the contributions of single energies to the overall visibility of the interferometer do not annihilate each other. Several optimization steps including energy-resolved measurements have been performed to steadily increase the visibility of the system. A crucial factor in this process was further the progress in grating manufacturing by the *Karlsruhe Institute of Technology* and *microworks GmbH* that produced more homogeneous and bridge-less grating structures. The latest setup configuration features a design energy of 27 keV and reaches visibility values of up to 40 %. The sensitivity as defined by the minimum resolvable refraction angle is 10 nrad when recording 11 images with 5 s exposure time each. There is no grating-based imaging setup reported in literature that is operated at a conventional polychromatic X-ray tube and offers a better angular sensitivity.

A tomographic scan procedure was successfully implemented and provides high-quality and quantitative 3D imaging results. The maximum FOV is $4{\times}2\,\mathrm{cm}^2$ (width $\times$ height) at the position of the sample stage, which is directly mounted in front of the phase grating. The voxel size of the final data is $100{\times}100{\times}100\,\mu\mathrm{m}^3$. To avoid ring artifacts in the reconstructed images, which can arise from inhomogeneities of the gratings or the detector sensor, the sample is laterally displaced by an integer number of pixels between each projection. In addition, the examined sample is submerged in a water bath during the measurement to prevent phase-wrapping or beam-hardening artifacts. A calibration process utilizing PMMA rods has been demonstrated to be suitable for the evaluation of effective energies in both contrast modalities. An accurate conversion of the original 3D data into linear attenuation coefficients μ, refractive index decrements δ, and electron densities ρ_e becomes then possible. Phantom studies revealed that an electron-density resolution of below $1\,\mathrm{e/nm}^3$ and an accuracy of 1–$2\,\mathrm{e/nm}^3$ can be achieved despite the polychromatic X-ray source. This high electron-density sensitivity allows for the visualization of different tissue types and soft-tissue fine structure, which has been only realized with synchrotron radiation so far.
Phase-contrast Hounsfield units as proposed by Donath et al. (2010) are a good measure for quantitative tissue characterization. Radiologists are used to this kind of unit from conventional CT imaging in the clinics. HUp numbers are comparable among different setups due to their energy independence. Moreover, the electron density of a tissue can be easily calculated from its HUp. Excised tissue samples need to be placed within falcon tubes of $\varnothing\,3\,\mathrm{cm}$ for the measurements. The employed water bath can be cooled down to $4\,^\circ\mathrm{C}$ to preserve non-fixated tissue samples from decay during the long scanning times of about 12 hours. A study on porcine fat and rind showed that the effects of formalin fixation on HUp values is rather low. The protein cross-linking shrinks the tissues and increases their protein density. In addition, the water in the tissues is replaced by the penetrating formalin. The typical solution of 3.7 % formaldehyde enhances the HUp of muscle and skin tissue by about 10 %, whereas adipose tissue remains unaffected. Because preserved tissue samples can be subjected to longer storage and scanning times without cooling, most biomedical studies are performed with formalin-fixated tissues. Another advantage of the preservation is a stiffening of the sample, which facilitates a sharp image acquisition.
The added value of quantitative phase-contrast imaging for the examination of tissue samples was demonstrated by means of breast imaging. Three different types of tissues could be clearly differentiated by phase-contrast Hounsfield units. Adipose tissue shows values between $-65\,\mathrm{HUp}$ and $-70\,\mathrm{HUp}$, tumor tissue gives values around $45\,\mathrm{HUp}$ to $50\,\mathrm{HUp}$, and healthy fibroglandular tissue has values of about $65\,\mathrm{HUp}$. In addition, fibrous tissue structures like strands or dilated ducts within tumors can be visualized. Whereas it is not possible to discriminate between malignant and benign tumor cells by quantitative numbers alone,

the morphological information revealed by differences in fibrous and less fibrous tissue values as well as by the appearance and shape of fibrous strands or dilated ducts might allow for tumor identification. The study could further show that previously published tissue properties suffer from an insufficient spatial resolution of the applied methods. For this reason, the large variety of tissue types is not appropriately represented in literature and available values often reflect merely the average of mixed tissues. Here, phase-contrast imaging and its capability for 3D tissue characterization can provide electron densities and morphological information that can be used for simulations or the choice of suitable phantom materials. Another biomedical research topic that has been studied in the course of this thesis is the investigation of atherosclerotic plaque. Features like the fibrous cap, intraplaque hemorrhage, or the necrotic core can be depicted by phase-contrast CT and plaques can be classified according to precisely defined morphology and tissue criteria. Current research activities in collaboration with radiologists from the clinics include, for example, the mapping of structural changes in different heart diseases, the appearance of renal cell carcinoma subtypes, and the grading of liver cirrhosis.

Besides the high soft-tissue resolution in phase contrast, grating interferometry delivers a perfectly co-registered dataset of the examined object in conventional attenuation contrast. The signal in attenuation contrast is proportional to the signal that is obtained in phase contrast, if the attenuation process is purely caused by Compton scattering. Otherwise, if photoelectric absorption takes place as well, the linear attenuation coefficient contains additional information on the material composition. This is the case for the energy range of the installed setup and, thus, the imaging results that are provided by the system in attenuation contrast and phase contrast are complementary. The possibility to assign an effective atomic number to a material by the combination of both contrast mechanisms has been illustrated by phantom measurements. Beyond that, an enhanced tissue analysis in terms of water, protein, and lipid contents seems to be feasible. Whereas tissues with enriched protein concentrations have an elevated electron density and, thus, display higher values in phase contrast, attenuation contrast achieves good contrast for lipid-rich tissues like adipose tissue as commonly known from medical CT imaging. Theoretically calculated HU and HUp values for fictive mixtures of varying protein, lipid, and water concentrations showed that every HU-HUp-pair can be associated with exactly one specific protein, lipid, and water content by applying a vector decomposition. The approach was tested on experimental data of a phantom consisting of dairy products, a sample of porcine fat and rind, and an excised human tissue specimen. The preliminary results are promising, but further investigations are needed to address the optimum choice of the utilized vectors and the effect of heavy trace elements on the analysis. A clinically relevant showcase, which demonstrates the benefit of the signal complementarity, is the examination of cystic renal lesions. While attenuation contrast allows the differ-

entiation of increasing concentrations of iodine, the phase-contrast signal is hardly affected by the contrast agent. This enables to discriminate simple and hemorrhagic cysts from enhancing cystic renal lesions by combination of both imaging modalities. Because iodine contrast agents are broadly employed in conventional CT diagnostics, the findings might be transferred to other potential medical applications. A determination of the amount of iodine within a certain tissue in analogy to the evaluation of protein and lipid contents might be conceivable. Concerning lab-based X-ray imaging, the use of iodine or similar contrast agents for staining of tissue samples is increasingly investigated to improve image quality in conventional attenuation contrast (Pauwels et al. 2013, Silva et al. 2015). The intrinsically high soft-tissue contrast provided by phase-contrast imaging together with an enhanced attenuation contrast and the possibility to quantify the accumulation of the contrast agent at each point in the specimen might open up even more new perspectives.

A promising field of application for 3D tissue analysis that is going beyond biomedical research is the assistance of histopathology in clinical routine, for example by virtual histology of biopsies (Zanette et al. 2013, Holme et al. 2014). The two main shortcomings of the phase-contrast imaging setup in this regard are the limited spatial resolution of above 100 µm and the long scanning times of several hours. Smaller effective voxel sizes can be realized either by geometrical magnification or by utilizing a detector with smaller pixel sizes. In the first case, the phase sensitivity is reduced, because the sample stage needs to be placed closer to the source and away from the phase grating. In the second case, less photon counts per pixel lead to higher noise levels, if the measurement times are kept constant. Both scenarios require an alternative X-ray source, which features a smaller focal spot than the current one. Otherwise, blurring that is caused by the extended source size degrades the actually achievable spatial resolution. In conventional X-ray tube technology, a small spot size is unfortunately opposed to an increase in X-ray flux, which is desirable to cut down on scanning times. The reason is the maximum heat load, which is limited by the melting point and the heat conductivity of the target material. Here, new approaches like the liquid-metal-jet source could be a solution (Hemberg et al. 2003, Larsson et al. 2011). In addition to a higher photon flux of the source, a better quantum-detecting efficiency of the detector system is important for a reduction of measurement times. This can be achieved by novel sensor materials like CdTe and GaAs. With respect to the spatial resolution, photon-counting X-ray detectors with pixel sizes below $172 \times 172\,\mu m^2$ as offered by the *PILATUS II* are being developed. The *EIGER* system from *Dectris* and the *Medipix3* read-out chip, which arises from an international collaboration hosted by *CERN*, have pixel pitches of 75 µm and 55 µm, respectively (Gkoumas et al. 2016, Pennicard et al. 2011). When moving towards higher spatial resolutions and smaller sample sizes, the phase-contrast imaging setup should be optimized for lower effective energies by replacing the

phase grating and by adjusting the distances between the gratings accordingly. Grating wafer made of low absorbing materials should be used (Koch et al. 2015). The visibility of the interferometer is another crucial parameter to shorten the scanning times. The current setup configuration reaches values of up to 40 % and further improvements are presumably difficult. An option might be the employment of phase gratings with duty cycles that vary from 0.5 (Rieger et al. 2016). In the future, laboratory sources that can provide monochromatic radiation or energy-resolving imaging detectors have the potential to enhance the visibility by narrowing the spectral width (Eggl et al. 2015, Thüring et al. 2013b, Pelzer et al. 2013). In addition, the realization of higher signal intensities is beneficial to attain good image quality at shorter exposure times. Larger refraction angles are for example induced by lower X-ray energies. Smaller grating periods can improve the signal as well. However, at some point, the grating interferometer is then operated in the far-field regime (Wen et al. 2013, Miao et al. 2015).
The stepping procedure that is performed for the signal extraction is a very time-consuming process, asking for alternative concepts. Several approaches have been proposed to circumvent the need to step one of the gratings during image acquisition. A moiré pattern can be intentionally generated by slightly misaligning the gratings. A single-shot fringe analysis can then be done to retrieve the phase information (Bevins et al. 2012). Another option is to fabricate the analyzer grating in a way that different stepping positions are incorporated for neighboring detector lines. By that, the different stepping positions can be captured within one image (Ge et al. 2014). Both solutions decrease the spatial resolution, because multiple pixels are merged to extract the phase information. The reverse projection method is based on a linear approximation of the stepping curve at its steepest point and is only correct for small refraction angles (Zhu et al. 2010). Another possibility that avoids the stepping of one of the gratings is the combination of a helical sample motion with moiré fringe scanning as it has been discussed in this thesis. At last, new algorithms are being developed that allow for a direct reconstruction of phase-contrast and attenuation-contrast data from the measured detector values (Brendel et al. 2016). The results are very encouraging that the stepping procedure can be abandoned soon and faster phase-contrast CT scans become feasible.
Concerning an implementation of X-ray phase-contrast imaging for in-vivo diagnostics in the clinics, several additional challenges have to be overcome. First experimental prototypes for radiographic applications like mammography have been already installed to evaluate their diagnostic benefits (Koehler et al. 2015, Tanaka et al. 2013). Tomographic examinations, on the other side, face the problem that all X-ray components including the grating interferometer have to be rotated around the living patient. The only device that features a rotating gantry, which is equipped with gratings to perform phase-contrast imaging, is a preclinical small-animal CT scanner of *Bruker Skyscan*. Artifacts that result from

mechanical instabilities can be corrected by adequate data processing algorithms and accurate phase-contrast images can be reconstructed from the acquired data (Tapfer et al. 2012). However, a continuous gantry rotation is not possible up to now due to the stepping procedure. Another crucial point for the realization of a clinical phase-contrast CT system is the comparably large FOV that is required to cover the full width of the human body. Imaging results with stitched grating tiles have been shown earlier in this thesis. This approach may be extended to manufacture gratings for areas of sufficient size. Bent gratings that become necessary at large cone beam angles to prevent shadowing effects have been demonstrated to be feasible (Thüring et al. 2011). Grating structures with aspect ratios that are high enough to guarantee a proper functioning of the interferometer at the energy range of clinical CT scanners (up to 140 keV) are to some extent available (Thüring et al. 2014b, Ruiz-Yaniz et al. 2015a). At these high energies, the complementarity of attenuation contrast and phase contrast is lost for materials with low effective atomic numbers like soft tissues as illustrated by synchrotron measurements in the course of this thesis. A combined data analysis might remain interesting for the quantification of contrast agents and the examination of mineralized structures like bones, teeth, or renal calculi. In this context, phase-contrast CT has to outperform energy-resolving X-ray imaging methods. Spectral CT imaging is steadily evolving and first devices have already been installed for clinical evaluation (Pourmorteza et al. 2016, Gutjahr et al. 2016). If the additional information content that is provided by phase-contrast CT does not justify an implementation for medical use, the increased soft-tissue contrast may open up new opportunities for diagnostics. The expected gain in contrast-to-noise ratios compared to attenuation contrast, however, diminishes at lower spatial resolutions (Raupach & Flohr 2011). Because the detector systems in human CT scanners have usually pixel sizes of about 0.5 to 1 mm, the advantage of phase contrast is controversially discussed (Raupach & Flohr 2012, Weber et al. 2015). Regions-of-interest measurements at higher spatial resolutions, but eventually with slightly elevated radiation dose levels than currently applied, might exploit the full potential of phase-contrast imaging and allow for the examination of predefined areas in order to detect tumors in inner organs or vulnerable plaques in arteries. Apart from that, clinical diagnostics could profit from the third contrast mode that can be obtained by X-ray grating interferometry. The dark-field contrast, which was only briefly described in this thesis, is sensitive to structure sizes below the spatial resolution of the detector and enables for example to track pathologic changes in the lung (Yaroshenko et al. 2014, Velroyen et al. 2015).
Overall, phase-contrast CT will continue to be an active research area in biomedical imaging over the next years. Progress in multiple disciplines like X-ray source technology, detector development, grating manufacturing, and algorithm design is the key to realize the full potential of this novel imaging modality in the future.

Bibliography

Afdhal, N. H. & Nunes, D. (2004), 'Evaluation of liver fibrosis: a concise review', *The American Journal of Gastroenterology* 99(6), 1160–1174.

Al-Bahri, J. S. & Spyrou, N. M. (1998), 'Electron density of normal and pathological breast tissues using a compton scattering technique', *Applied Radiation and Isotopes: Including Data, Instrumentation and Methods for Use in Agriculture, Industry and Medicine* 49(12), 1677–1684.

Allner, S., Koehler, T., Fehringer, A., Birnbacher, L., Willner, M., Pfeiffer, F. & Noël, P. B. (2016), 'Bilateral filtering using the full noise covariance matrix applied to X-ray phase-contrast computed tomography', *Physics in Medicine and Biology* 61(10), 3867–3884.

Als-Nielsen, J. & McMorrow, D. (2008), *Elements of Modern X-ray Physics*, John Wiley & Sons, USA.

Antoniassi, M., Conceição, A. & Poletti, M. (2010), 'Characterization of breast tissues using Compton scattering', *Nuclear Instruments and Methods in Physics Research Section A: Accelerators, Spectrometers, Detectors and Associated Equipment* 619(1-3), 375–378.

Antoniassi, M., Conceição, A. & Poletti, M. (2012), 'Study of electron densities of normal and neoplastic human breast tissues by Compton scattering using synchrotron radiation', *Applied Radiation and Isotopes* 70(7), 1351–1354.

Arfelli, F., Bonvicini, V., Bravin, A., Cantatore, G., Castelli, E., Palma, L. D., Michiel, M. D., Fabrizioli, M., Longo, R., Menk, R. H., Olivo, A., Pani, S., Pontoni, D., Poropat, P., Prest, M., Rashevsky, A., Ratti, M., Rigon, L., Tromba, G., Vacchi, A., Vallazza, E. & Zanconati, F. (2000), 'Mammography with synchrotron radiation: phase-detection techniques', *Radiology* 215(1), 286–293.

Athanasiou, A., Tardivon, A., Ollivier, L., Thibault, F., El Khoury, C. & Neuenschwander, S. (2009), 'How to optimize breast ultrasound', *European Journal of Radiology* 69(1), 6–13.

Bech, M. (2009), *X-ray Imaging with a Grating Interferometer*, Phd thesis, University of Copenhagen, Denmark.

Bech, M., Bunk, O., David, C., Kraft, P., Brönnimann, C., Eikenberry, E. & Pfeiffer, F. (2008), 'X-ray imaging with the PILATUS 100k detector', *Applied Radiation and Isotopes* 66(4), 474–478.

Bech, M., Jensen, T. H., Feidenhans'l, R., Bunk, O., David, C. & Pfeiffer, F. (2009), 'Soft-tissue phase-contrast tomography with an X-ray tube source', *Physics in Medicine and Biology* 54(9), 2747–2753.

Beckmann, F., Bonse, U., Busch, F. & Günnewig, O. (1997), 'X-ray microtomography (CT) using phase contrast for the investigation of organic matter', *Journal of Computer Assisted Tomography* 21(4), 539–553.

Berger, M., Hubbell, J., Seltzer, S., Chang, J., Coursey, J., Sukumar, R., Zucker, D. & Olsen, K. (2010), 'XCOM: Photon Cross Section Database'.
URL: *http://physics.nist.gov/xcom*

Berry, D. A., Cronin, K. A., Plevritis, S. K., Fryback, D. G., Clarke, L., Zelen, M., Mandelblatt, J. S., Yakovlev, A. Y., Habbema, J. D. F. & Feuer, E. J. (2005), 'Effect of screening and adjuvant therapy on mortality from breast cancer', *New England Journal of Medicine* 353(17), 1784–1792.

Bevins, N., Zambelli, J., Li, K., Qi, Z. & Chen, G.-H. (2012), 'Multicontrast X-ray computed tomography imaging using Talbot-Lau interferometry without phase stepping', *Medical Physics* 39(1), 424–428.

Birnbacher, L., Willner, M., Velroyen, A., Marschner, M., Hipp, A., Meiser, J., Koch, F., Schröter, T., Kunka, D., Mohr, J., Pfeiffer, F. & Herzen, J. (2016), 'Experimental realisation of high-sensitivity laboratory X-ray grating-based phase-contrast computed tomography', *Scientific Reports* 6, 24022.

Boll, D. T., Patil, N. A., Paulson, E. K., Merkle, E. M., Nelson, R. C., Schindera, S. T., Roessl, E., Martens, G., Proksa, R., Fleiter, T. R. & Schlomka, J.-P. (2010), 'Focal cystic high-attenuation lesions: characterization in renal phantom by using photon-counting spectral CT—improved differentiation of lesion composition', *Radiology* 254(1), 270–276.

Bonse, U. & Hart, M. (1965), 'An X-ray interferometer', *Applied Physics Letters* 6(8), 155–156.

Boone, J. M. (1999), 'Glandular breast dose for monoenergetic and high-energy X-ray beams: Monte Carlo assessment', *Radiology* 213(1), 23–37.

Bosniak, M. A. (1986), 'The current radiological approach to renal cysts', *Radiology* 158(1), 1–10.

Bravin, A., Coan, P. & Suortti, P. (2013), 'X-ray phase-contrast imaging: from pre-clinical applications towards clinics', *Physics in Medicine and Biology* 58(1), R1–35.

Bravin, A., Keyriläinen, J., Fernández, M., Fiedler, S., Nemoz, C., Karjalainen-Lindsberg, M.-L., Tenhunen, M., Virkkunen, P., Leidenius, M., von Smitten, K., Sipilä, P. & Suortti, P. (2007), 'High-resolution CT by diffraction-enhanced X-ray imaging: mapping of breast tissue samples and comparison with their histo-pathology', *Physics in Medicine and Biology* 52(8), 2197–2211.

Brendel, B., von Teuffenbach, M., Noël, P. B., Pfeiffer, F. & Koehler, T. (2016), 'Penalized maximum likelihood reconstruction for X-ray differential phase-contrast tomography', *Medical Physics* 43(1), 188–194.

Broennimann, C., Eikenberry, E., Henrich, B., Horisberger, R., Huelsen, G., Pohl, E., Schmitt, B., Schulze-Briese, C., Suzuki, M., Tomizaki, T., Toyokawa, H. & Wagner, A. (2006), 'The PILATUS 1M detector', *Journal of Synchrotron Radiation* 13(Part 2), 120–130.

Buesa, R. J. (2008), 'Histology without formalin?', *Annals of Diagnostic Pathology* 12(6), 387–396.

Burger, K., Koehler, T., Chabior, M., Allner, S., Marschner, M., Fehringer, A., Willner, M., Pfeiffer, F. & Noël, P. (2014), 'Regularized iterative integration combined with non-linear diffusion filtering for phase-contrast X-ray computed tomography', *Optics Express* 22(26), 32107.

Castelli, E., Tonutti, M., Arfelli, F., Longo, R., Quaia, E., Rigon, L., Sanabor, D., Zanconati, F., Dreossi, D., Abrami, A., Quai, E., Bregant, P., Casarin, K., Chenda, V., Menk, R. H., Rokvic, T., Vascotto, A., Tromba, G. & Cova, M. A. (2011), 'Mammography with synchrotron radiation: first clinical experience with phase-detection technique', *Radiology* 259(3), 684–694.

Cerussi, A., Hsiang, D., Shah, N., Mehta, R., Durkin, A., Butler, J. & Tromberg, B. J. (2007), 'Predicting response to breast cancer neoadjuvant chemotherapy using diffuse optical spectroscopy', *Proceedings of the National Academy of Sciences* 104(10), 4014–4019.

Chabior, M. (2011), *Contributions to the Characterization of Grating-Based X-ray Phase-Contrast Imaging*, Phd thesis, Technische Universität Dresden, Germany.

Chabior, M., Schuster, M., Goldammer, M., Schroer, C. & Pfeiffer, F. (2012b), 'Influence of the grating profiles on the image quality in grating-based X-ray imaging', *Nuclear Instruments and Methods in Physics Research Section A: Accelerators, Spectrometers, Detectors and Associated Equipment* 683, 71–77.

Chabior, M., Schuster, M., Schroer, C. & Pfeiffer, F. (2012a), 'Grating-based phase-contrast computed tomography of thick samples', *Nuclear Instruments and Methods in Physics Research Section A: Accelerators, Spectrometers, Detectors and Associated Equipment* 693, 138–142.

Chantler, C., Olsen, K., Dragoset, R., Chang, J., Kishore, A., Kotochigova, S. & Zucker, D. (2005), 'X-ray form factor, attenuation and scattering tables'.
URL: *http://physics.nist.gov/ffast*

Chen, G.-H., Zambelli, J., Li, K., Bevins, N. & Qi, Z. (2011), 'Scaling law for noise variance and spatial resolution in differential phase contrast computed tomography', *Medical Physics* 38(2), 584–588.

Cloetens, P., Ludwig, W., Baruchel, J., Van Dyck, D., Van Landuyt, J., Guigay, J. P. & Schlenker, M. (1999), 'Holotomography: quantitative phase tomography with micrometer resolution using hard synchrotron radiation X-rays', *Applied Physics Letters* 75(19), 2912–2914.

Cloetens, P., Pateyron-Salomé, M., Buffière, J. Y., Peix, G., Baruchel, J., Peyrin, F. & Schlenker, M. (1997), 'Observation of microstructure and damage in materials by phase sensitive radiography and tomography', *Journal of Applied Physics* 81(9), 5878–5886.

Dauendorffer, J. N., Bastuji-Garin, S., Guéro, S., Brousse, N. & Fraitag, S. (2009), 'Shrinkage of skin excision specimens: formalin fixation is not the culprit', *The British Journal of Dermatology* 160(4), 810–814.

Davis, T. J., Gao, D., Gureyev, T. E., Stevenson, A. W. & Wilkins, S. W. (1995), 'Phase-contrast imaging of weakly absorbing materials using hard X-rays', *Nature* 373, 595–598.

Ding, H. & Molloi, S. (2012), 'Quantification of breast density with spectral mammography based on a scanned multi-slit photon-counting detector: a feasibility study', *Physics in Medicine and Biology* 57(15), 4719–4738.

Donath, T., Chabior, M., Pfeiffer, F., Bunk, O., Reznikova, E., Mohr, J., Hempel, E., Popescu, S., Hoheisel, M., Schuster, M., Baumann, J. & David, C. (2009), 'Inverse geometry for grating-based X-ray phase-contrast imaging', *Journal of Applied Physics* 106(5), 054703.

Donath, T., Pfeiffer, F., Bunk, O., Grünzweig, C., Hempel, E., Popescu, S., Vock, P. & David, C. (2010), 'Toward clinical X-ray phase-contrast CT: demonstration of enhanced soft-tissue contrast in human specimen', *Investigative Radiology* 45(7), 445–452.

Eggl, E., Schleede, S., Bech, M., Achterhold, K., Loewen, R., Ruth, R. D. & Pfeiffer, F. (2015), 'X-ray phase-contrast tomography with a compact laser-driven synchrotron source', *Proceedings of the National Academy of Sciences* 112(18), 5567–5572.

Einarsdóttir, H., Nielsen, M. S., Miklos, R., Lametsch, R., Feidenhans'l, R., Larsen, R. & Ersbøll, B. K. (2014), 'Analysis of micro-structure in raw and heat treated meat emulsions from multimodal X-ray microtomography', *Innovative Food Science & Emerging Technologies* 24, 88–96.

Elston, C. W. & Ellis, I. O. (1991), 'Pathological prognostic factors in breast cancer. I. The value of histological grade in breast cancer: experience from a large study with long-term follow-up.', *Histopathology* 19(5), 403–410.

Engel, K. J., Geller, D., Köhler, T., Martens, G., Schusser, S., Vogtmeier, G. & Rössl, E. (2011), 'Contrast-to-noise in X-ray differential phase contrast imaging', *Nuclear Instruments and Methods in Physics Research Section A: Accelerators, Spectrometers, Detectors and Associated Equipment* 648(Supplement 1), S202–S207.

Engelhardt, M., Baumann, J., Schuster, M., Kottler, C., Pfeiffer, F., Bunk, O. & David, C. (2007), 'High-resolution differential phase contrast imaging using a magnifying projection geometry with a microfocus X-ray source', *Applied Physics Letters* 90(22), 224101.

Engelhardt, M., Kottler, C., Bunk, O., David, C., Schroer, C., Baumann, J., Schuster, M. & Pfeiffer, F. (2008), 'The fractional Talbot effect in differential X-ray phase-contrast imaging for extended and polychromatic X-ray sources', *Journal of Microscopy* 232(1), 145–157.

Esmaeili, M., Floystad, J. B., Hipp, A., Willner, M., Bech, M., Diaz, A., Royset, A., Andreasen, J. W., Pfeiffer, F. & Breiby, D. W. (2015), 'Monitoring moisture distribution in textile materials using grating interferometry and ptychographic X-ray imaging', *Textile Research Journal* 85(1), 80–90.

Farrell, G. C. & Larter, C. Z. (2006), 'Nonalcoholic fatty liver disease: from steatosis to cirrhosis', *Hepatology* 43(2, Supplement 1), S99–S112.

Faulconer, L., Parham, C., Connor, D. M., Zhong, Z., Kim, E., Zeng, D., Livasy, C., Cole, E., Kuzmiak, C., Koomen, M., Pavic, D. & Pisano, E. (2009), 'Radiol-

ogist evaluation of an X-ray tube-based diffraction-enhanced imaging prototype using full-thickness breast specimens', *Academic Radiology* 16(11), 1329–1337.

Feldkamp, L. A., Davis, L. C. & Kress, J. W. (1984), 'Practical cone-beam algorithm', *Journal of the Optical Society of America A* 1(6), 612–619.

Ferlay, J., Shin, H.-R., Bray, F., Forman, D., Mathers, C. & Parkin, D. M. (2010), 'Estimates of worldwide burden of cancer in 2008: GLOBOCAN 2008', *International Journal of Cancer* 127(12), 2893–2917.

Fingerle, A. A., Willner, M., Herzen, J., Münzel, D., Hahn, D., Rummeny, E. J., Noël, P. B. & Pfeiffer, F. (2014), 'Simulated cystic renal lesions: quantitative X-ray phase-contrast CT—an in vitro phantom study', *Radiology* 272(3), 739–748.

Fox, C. H., Johnson, F. B., Whiting, J. & Roller, P. P. (1985), 'Formaldehyde fixation', *The Journal of Histochemistry and Cytochemistry* 33(8), 845–853.

Frisullo, P., Laverse, J., Marino, R. & Nobile, M. D. (2009), 'X-ray computed tomography to study processed meat microstructure', *Journal of Food Engineering* 94(3-4), 283–289.

Fu, J., Biernath, T., Willner, M., Amberger, M., Meiser, J., Kunka, D., Mohr, J., Herzen, J., Bech, M. & Pfeiffer, F. (2014b), 'Cone-beam differential phase-contrast laminography with X-ray tube source', *EPL (Europhysics Letters)* 106(6), 68002.

Fu, J., Willner, M., Chen, L., Tan, R., Achterhold, K., Bech, M., Herzen, J., Kunka, D., Mohr, J. & Pfeiffer, F. (2014a), 'Helical differential X-ray phase-contrast computed tomography', *Physica Medica* 30(3), 374–379.

Gaass, T., Potdevin, G., Bech, M., Noël, P. B., Willner, M., Tapfer, A., Pfeiffer, F. & Haase, A. (2013), 'Iterative reconstruction for few-view grating-based phase-contrast CT—an in vitro mouse model', *EPL (Europhysics Letters)* 102(4), 48001.

Ge, Y., Li, K., Garrett, J. & Chen, G.-H. (2014), 'Grating based X-ray differential phase contrast imaging without mechanical phase stepping', *Optics Express* 22(12), 14246.

Gkoumas, S., Wang, Z., Abis, M., Arboleda, C., Tudosie, G., Donath, T., Brönnimann, C., Schulze-Briese, C. & Stampanoni, M. (2016), 'Grating-based interferometry and hybrid photon counting detectors: towards a new era in X-ray medical imaging', *Nuclear Instruments and Methods in Physics Research Section A: Accelerators, Spectrometers, Detectors and Associated Equipment* 809, 23–30.

Golomb, F. M., Doyle, J. P., Grin, C. M., Kopf, A. W., Silverman, M. K. & Levenstein, M. J. (1991), 'Determination of preexcision surgical margins of melanomas from fixed-tissue specimens', *Plastic and Reconstructive Surgery* 88(5), 804–809.

Grandl, S., Willner, M., Herzen, J., Mayr, D., Auweter, S. D., Hipp, A., Pfeiffer, F., Reiser, M. & Hellerhoff, K. (2013), 'Evaluation of phase-contrast CT of breast tissue at conventional X-ray sources – presentation of selected findings', *Zeitschrift für Medizinische Physik* 23(3), 212–221.

Grandl, S., Willner, M., Herzen, J., Sztrókay-Gaul, A., Mayr, D., Auweter, S. D., Hipp, A., Birnbacher, L., Marschner, M., Chabior, M., Reiser, M., Pfeiffer, F., Bamberg, F. & Hellerhoff, K. (2014), 'Visualizing typical features of breast fibroadenomas using phase-contrast CT: an ex-vivo study', *PLoS ONE* 9(5), e97101.

Gregory, N., Mulvaney, M., Pattison, T., Hill, J., Carlson, J. A. & Goncharuk, V. (2003), 'Shrinkage of skin excision specimens and downcoding', *Archives of Dermatology* 139(4), 542–543.

Gutjahr, R., Halaweish, A. F., Yu, Z., Leng, S., Yu, L., Li, Z., Jorgensen, S. M., Ritman, E. L., Kappler, S. & McCollough, C. H. (2016), 'Human imaging with photon counting-based computed tomography at clinical dose levels', *Investigative Radiology* 51(7), 421–429.

Hahn, D., Thibault, P., Fehringer, A., Bech, M., Koehler, T., Pfeiffer, F. & Noël, P. B. (2015), 'Statistical iterative reconstruction algorithm for X-ray phase-contrast CT', *Scientific Reports* 5, 10452.

Haka, A. S., Shafer-Peltier, K. E., Fitzmaurice, M., Crowe, J., Dasari, R. R. & Feld, M. S. (2005), 'Diagnosing breast cancer by using Raman spectroscopy', *Proceedings of the National Academy of Sciences* 102(35), 12371–12376.

Hammerstein, G. R., Miller, D. W., White, D. R., Masterson, M. E., Woodard, H. Q. & Laughlin, J. S. (1979), 'Absorbed radiation dose in mammography', *Radiology* 130(2), 485–491.

Hemberg, O., Otendal, M. & Hertz, H. M. (2003), 'Liquid-metal-jet anode electron-impact X-ray source', *Applied Physics Letters* 83(7), 1483.

Henningsen, J. (2014), *Quantitative X-ray Phase-Contrast Imaging for the Differentiation of Bodily Fluids*, Bachelor thesis, Technische Universität München, Germany.

Herzen, J., Donath, T., Pfeiffer, F., Bunk, O., Padeste, C., Beckmann, F., Schreyer, A. & David, C. (2009), 'Quantitative phase-contrast tomography

of a liquid phantom using a conventional X-ray tube source', *Optics Express* 17(12), 10010.

Herzen, J., Willner, M. S., Fingerle, A. A., Noël, P. B., Köhler, T., Drecoll, E., Rummeny, E. J. & Pfeiffer, F. (2014), 'Imaging liver lesions using grating-based phase-contrast computed tomography with bi-Lateral filter post-processing', *PLoS ONE* 9(1), e83369.

Heslinga, F. J. M. & Deierkauf, F. A. (1962), 'The action of formaldehyde solutions on human brain lipids', *Journal of Histochemistry & Cytochemistry* 10(6), 704–709.

Hetterich, H., Fill, S., Herzen, J., Willner, M., Zanette, I., Weitkamp, T., Rack, A., Schüller, U., Sadeghi, M., Brandl, R., Adam-Neumair, S., Reiser, M., Pfeiffer, F., Bamberg, F. & Saam, T. (2013), 'Grating-based X-ray phase-contrast tomography of atherosclerotic plaque at high photon energies', *Zeitschrift für Medizinische Physik* 23(3), 194–203.

Hetterich, H., Webber, N., Willner, M., Herzen, J., Birnbacher, L., Hipp, A., Marschner, M., Auweter, S. D., Habbel, C., Schüller, U., Bamberg, F., Ertl-Wagner, B., Pfeiffer, F. & Saam, T. (2015b), 'AHA classification of coronary and carotid atherosclerotic plaques by grating-based phase-contrast computed tomography', *European Radiology* 26, 3223.

Hetterich, H., Willner, M., Fill, S., Herzen, J., Bamberg, F., Hipp, A., Schüller, U., Adam-Neumair, S., Wirth, S., Reiser, M., Pfeiffer, F. & Saam, T. (2014), 'Phase-contrast CT: qualitative and quantitative evaluation of atherosclerotic carotid artery plaque', *Radiology* 271(3), 870–878.

Hetterich, H., Willner, M., Habbel, C., Herzen, J., Hoffmann, V. S., Fill, S., Hipp, A., Marschner, M., Schüller, U., Auweter, S., Massberg, S., Reiser, M. F., Pfeiffer, F., Saam, T. & Bamberg, F. (2015a), 'X-ray phase-contrast computed tomography of human coronary arteries', *Investigative Radiology* 50(10), 686–694.

Hipp, A. (2013), *Highly Sensitive Grating Interferometry Using a Polychromatic X-ray Source*, Diploma thesis, Technische Universität München, Germany.

Hipp, A., Willner, M., Herzen, J., Auweter, S. D., Chabior, M., Meiser, J., Achterhold, K., Mohr, J. & Pfeiffer, F. (2014), 'Energy-resolved visibility analysis of grating interferometers operated at polychromatic X-ray sources', *Optics Express* 22(25), 30394.

Holme, M. N., Schulz, G., Deyhle, H., Weitkamp, T., Beckmann, F., Lobrinus, J. A., Rikhtegar, F., Kurtcuoglu, V., Zanette, I., Saxer, T. & Müller, B.

(2014), 'Complementary X-ray tomography techniques for histology-validated 3D imaging of soft and hard tissues using plaque-containing blood vessels as examples', *Nature Protocols* 9(6), 1401–1415.

Hounsfield, G. N. (1973), 'Computerized transverse axial scanning (tomography): part 1. Description of system.', *British Journal of Radiology* 46(552), 1016–1022.

Hudson-Peacock, M. J., Matthews, J. N. & Lawrence, C. M. (1995), 'Relation between size of skin excision, wound, and specimen', *Journal of the American Academy of Dermatology* 32(6), 1010–1015.

ICRU (1989), *Report 44: Tissue Substitutes in Radiation Dosimetry and Measurement*, International Commission on Radiation Units and Measurements, Bethesda, USA.

Ingal, V. N. & Beliaevskaya, E. A. (1995), 'X-ray plane-wave topography observation of the phase-contrast from a noncrystalline object', *Journal of Physics D Applied Physics* 28(11), 2314–2317.

Jackson, D. F. & Hawkes, D. (1981), 'X-ray attenuation coefficients of elements and mixtures', *Physics Reports* 70(3), 169–233.

Johns, P. C. & Yaffe, M. J. (1987), 'X-ray characterisation of normal and neoplastic breast tissues', *Physics in Medicine and Biology* 32(6), 675–695.

Kak, A. C. & Slaney, M. (2001), *Principles of Computerized Tomographic Imaging*, Society for Industrial and Applied Mathematics, Philadelphia, USA.

Kalender, W. a., Beister, M., Boone, J. M., Kolditz, D., Vollmar, S. V. & Weigel, M. C. C. (2012), 'High-resolution spiral CT of the breast at very low dose: concept and feasibility considerations', *European Radiology* 22(1), 1–8.

Kenntner, J. (2013), *Herstellung von Gitterstrukturen mit Aspektverhältnis 100 für die Phasenkontrastbildgebung in einem Talbot-Interferometer*, Phd thesis, Karlsruhe Institute of Technology (KIT), Germany.

Kenntner, J., Altapova, V., Grund, T., Pantenburg, F. J., Meiser, J., Baumbach, T. & Mohr, J. (2012), 'Fabrication and characterization of analyzer gratings with high aspect ratios for phase contrast imaging using a Talbot interferometer', *AIP Conference Proceedings* 1437, 89–93.

Keyriläinen, J., Fernández, M., Karjalainen-Lindsberg, M.-L., Virkkunen, P., Leidenius, M., von Smitten, K., Sipilä, P., Fiedler, S., Suhonen, H., Suortti, P. & Bravin, A. (2008), 'Toward high-contrast breast CT at low radiation dose', *Radiology* 249(1), 321–327.

Kiernan, J. (2000), 'Formaldehyde, formalin, paraformaldehyde and glutaraldehyde: what they are and what they do', *Microscopy Today* 12, 8–12.

Kleiner, D. E., Brunt, E. M., Van Natta, M., Behling, C., Contos, M. J., Cummings, O. W., Ferrell, L. D., Liu, Y.-C., Torbenson, M. S., Unalp-Arida, A., Yeh, M., McCullough, A. J., Sanyal, A. J. & Nonalcoholic Steatohepatitis Clinical Research Network (2005), 'Design and validation of a histological scoring system for nonalcoholic fatty liver disease', *Hepatology* 41(6), 1313–1321.

Koch, F. J., Schröter, T. J., Kunka, D., Meyer, P., Meiser, J., Faisal, A., Khalil, M. I., Birnbacher, L., Viermetz, M., Walter, M., Schulz, J., Pfeiffer, F. & Mohr, J. (2015), 'Gratings on low absorbing substrates for X-ray phase contrast imaging', *Review of Scientific Instruments* 86(12), 126114.

Koehler, T., Daerr, H., Martens, G., Kuhn, N., Löscher, S., van Stevendaal, U. & Roessl, E. (2015), 'Slit-scanning differential X-ray phase-contrast mammography: proof-of-concept experimental studies', *Medical Physics* 42(4), 1959–1965.

Kottler, C., Pfeiffer, F., Bunk, O., Grunzweig, C. & David, C. (2007), 'Grating interferometer based scanning setup for hard X-ray phase contrast imaging', *Review of Scientific Instruments* 78(4), 043710.

Kottler, C., Revol, V., Maake, C., Kaufmann, R. & Urban, C. (2010), 'Phase sensitive X-ray imaging: towards medical applications', *Nuclear Science Symposium Conference Record (NSS/MIC), IEEE* 41, 2445–2448.

Kuhl, C. (2007*a*), 'The current status of breast MR imaging. Part I. Choice of technique, image interpretation, diagnostic accuracy, and transfer to clinical practice.', *Radiology* 244(2), 356–378.

Kuhl, C. K. (2007*b*), 'Current status of breast MR imaging. Part 2. Clinical applications.', *Radiology* 244(3), 672–691.

Larsson, D. H., Takman, P. A. C., Lundström, U., Burvall, A. & Hertz, H. M. (2011), 'A 24 keV liquid-metal-jet X-ray source for biomedical applications', *Review of Scientific Instruments* 82(12), 123701.

Lauridsen, T., Willner, M., Bech, M., Pfeiffer, F. & Feidenhans'l, R. (2015), 'Detection of sub-pixel fractures in X-ray dark-field tomography', *Applied Physics A* 121(3), 1243–1250.

Le-Petross, H. T. & Shetty, M. K. (2011), 'Magnetic resonance imaging and breast ultrasonography as an adjunct to mammographic screening in high-risk patients', *Seminars in Ultrasound, CT, and MR* 32(4), 266–272.

Ligabue, G., Besutti, G., Scaglioni, R., Stentarelli, C. & Guaraldi, G. (2013), 'MR quantitative biomarkers of non-alcoholic fatty liver disease: technical evolutions and future trends', *Quantitative Imaging in Medicine and Surgery* 3(4), 192–195.

Lloyd-Jones, D., Adams, R. J., Brown, T. M., Carnethon, M., Dai, S., De Simone, G., Ferguson, T. B., Ford, E., Furie, K., Gillespie, C., Go, A., Greenlund, K., Haase, N., Hailpern, S., Ho, P. M., Howard, V., Kissela, B., Kittner, S., Lackland, D., Lisabeth, L., Marelli, A., McDermott, M. M., Meigs, J., Mozaffarian, D., Mussolino, M., Nichol, G., Roger, V. L., Rosamond, W., Sacco, R., Sorlie, P., Stafford, R., Thom, T., Wasserthiel-Smoller, S., Wong, N. D. & Wylie-Rosett, J. (2010), 'Executive summary: heart disease and stroke statistics—2010 update: a report from the American Heart Association', *Circulation* 121(7), 948–954.

Lohmann, A. W., Knuppertz, H. & Jahns, J. (2005), 'Fractional Montgomery effect: a self-imaging phenomenon', *Journal of the Optical Society of America A* 22(8), 1500–1508.

Machann, J., Bachmann, O. P., Brechtel, K., Dahl, D. B., Wietek, B., Klumpp, B., Häring, H.-U., Claussen, C. D., Jacob, S. & Schick, F. (2003), 'Lipid content in the musculature of the lower leg assessed by fat selective MRI: intra- and interindividual differences and correlation with anthropometric and metabolic data', *Journal of Magnetic Resonance Imaging* 17(3), 350–357.

Marschner, M. (2013), *Data Processing in Grating-Based X-ray Phase-Contrast Computed Tomography: Workflow Automation and Noise Studies*, Diploma thesis, Technische Universität München, Germany.

Marschner, M., Willner, M., Potdevin, G., Fehringer, A., Noël, P. B., Pfeiffer, F. & Herzen, J. (2016), 'Helical X-ray phase-contrast computed tomography without phase stepping', *Scientific Reports* 6, 23953.

McDonald, S. A., Marone, F., Hintermüller, C., Mikuljan, G., David, C., Pfeiffer, F. & Stampanoni, M. (2009), 'Advanced phase-contrast imaging using a grating interferometer', *Journal of Synchrotron Radiation* 16(4), 562–572.

Meiser, J., Willner, M., Schröter, T., Hofmann, A., Rieger, J., Koch, F., Birnbacher, L., Schüttler, M., Kunka, D., Meyer, P., Faisal, A., Amberger, M., Duttenhofer, T., Weber, T., Hipp, A., Ehn, S., Walter, M., Herzen, J., Schulz, J., Pfeiffer, F. & Mohr, J. (2016), 'Increasing the field of view in grating based X-ray phase contrast imaging using stitched gratings', *Journal of X-ray Science and Technology* 24(3), 379–388.

Miao, H., Gomella, A. A., Harmon, K. J., Bennett, E. E., Chedid, N., Znati, S., Panna, A., Foster, B. A., Bhandarkar, P. & Wen, H. (2015), 'Enhancing table-top X-ray phase contrast imaging with nano-fabrication', *Scientific Reports* 5, 13581.

Michel, T., Rieger, J., Anton, G., Bayer, F., Beckmann, M. W., Durst, J., Fasching, P. A., Haas, W., Hartmann, A., Pelzer, G., Radicke, M., Rauh, C., Ritter, A., Sievers, P., Schulz-Wendtland, R., Uder, M., Wachter, D. L., Weber, T., Wenkel, E. & Zang, A. (2013), 'On a dark-field signal generated by micrometer-sized calcifications in phase-contrast mammography', *Physics in Medicine and Biology* 58(8), 2713–2732.

Modregger, P., Pinzer, B. R., Thüring, T., Rutishauser, S., David, C. & Stampanoni, M. (2011), 'Sensitivity of X-ray grating interferometry', *Optics Express* 19(19), 18324.

Mohajerani, P., Hipp, A., Willner, M., Marschner, M., Trajkovic-Arsic, M., Ma, X., Burton, N. C., Klemm, U., Radrich, K., Ermolayev, V., Tzoumas, S., Siveke, J. T., Bech, M., Pfeiffer, F. & Ntziachristos, V. (2014), 'FMT-PCCT: Hybrid fluorescence molecular tomography—X-ray phase-contrast CT imaging of mouse models', *IEEE Transactions on Medical Imaging* 33(7), 1434–1446.

Momose, A. (1995), 'Demonstration of phase-contrast X-ray computed tomography using an X-ray interferometer', *Nuclear Instruments and Methods in Physics Research Section A: Accelerators, Spectrometers, Detectors and Associated Equipment* 352(3), 622–628.

Momose, A. (2003), 'Phase-sensitive imaging and phase tomography using X-ray interferometers', *Optics Express* 11(19), 2303.

Momose, A. (2005), 'Recent advances in X-ray phase imaging', *Japanese Journal of Applied Physics* 44(9A), 6355–6367.

Momose, A., Kawamoto, S., Koyama, I., Hamaishi, Y., Takai, K. & Suzuki, Y. (2003), 'Demonstration of X-ray Talbot interferometry', *Japanese Journal of Applied Physics* 42(7B), L866–L868.

Momose, A., Yashiro, W., Takeda, Y., Suzuki, Y. & Hattori, T. (2006), 'Phase tomography by X-ray Talbot interferometry for biological imaging', *Japanese Journal of Applied Physics* 45(6A), 5254–5262.

Mueller, K. (1998), *From Cone-Beam Projection Data Using Algebraic Methods*, Phd thesis, Ohio State University, USA.

Munro, P. R. T., Ignatyev, K., Speller, R. D. & Olivo, A. (2010), 'Design of a novel phase contrast X-ray imaging system for mammography', *Physics in Medicine and Biology* 55(14), 4169–4185.

Munro, P. R. T. & Olivo, A. (2013), 'X-ray phase-contrast imaging with polychromatic sources and the concept of effective energy', *Physical Review A* 87(5), 053838.

Naghavi, M. (2003*a*), 'From vulnerable plaque to vulnerable patient: a call for new definitions and risk assessment strategies: part I', *Circulation* 108(14), 1664–1672.

Naghavi, M. (2003*b*), 'From vulnerable plaque to vulnerable patient: a call for new definitions and risk assessment strategies: part II', *Circulation* 108(15), 1772–1778.

Nesch, I., Fogarty, D. P., Tzvetkov, T., Reinhart, B., Walus, A. C., Khelashvili, G., Muehleman, C. & Chapman, D. (2009), 'The design and application of an in-laboratory diffraction-enhanced X-ray imaging instrument', *Review of Scientific Instruments* 80, 093702.

Nielsen, M. S., Lauridsen, T., Thomsen, M., Jensen, T. H., Bech, M., Christensen, L. B., Olsen, E. V., Hviid, M., Feidenhans'l, R. & Pfeiffer, F. (2012), 'X-ray tomography using the full complex index of refraction', *Physics in Medicine and Biology* 57(19), 5971–5979.

Noël, P. B., Herzen, J., Fingerle, A. A., Willner, M., Stockmar, M. K., Hahn, D., Settles, M., Drecoll, E., Zanette, I., Weitkamp, T., Rummeny, E. J. & Pfeiffer, F. (2013), 'Evaluation of the potential of phase-contrast computed tomography for improved visualization of cancerous human liver tissue', *Zeitschrift für Medizinische Physik* 23(3), 204–211.

O'Sullivan, A., O'Connor, B., Kelly, A. & McGrath, M. J. (1999), 'The use of chemical and infrared methods for analysis of milk and dairy products', *International Journal of Dairy Technology* 52(4), 139–148.

Paganin, D., Mayo, S. C., Gureyev, T. E., Miller, P. R. & Wilkins, S. W. (2002), 'Simultaneous phase and amplitude extraction from a single defocused image of a homogeneous object', *Journal of Microscopy* 206(1), 33–40.

Parham, C., Zhong, Z., Connor, D. M., Chapman, L. D. & Pisano, E. D. (2009), 'Design and implementation of a compact low-dose diffraction enhanced medical imaging system', *Academic Radiology* 16(8), 911–917.

Pauwels, E., van Loo, D., Cornillie, P., Brabant, L. & van Hoorebeke, L. (2013), 'An exploratory study of contrast agents for soft tissue visualization by means

of high resolution X-ray computed tomography imaging', *Journal of Microscopy* 250(1), 21–31.

Pelzer, G., Weber, T., Anton, G., Ballabriga, R., Bayer, F., Campbell, M., Gabor, T., Haas, W., Horn, F., Llopart, X., Michel, N., Mollenbauer, U., Rieger, J., Ritter, A., Ritter, I., Sievers, P., Wölfel, S., Wong, W. S., Zang, A. & Michel, T. (2013), 'Grating-based X-ray phase-contrast imaging with a multi energy-channel photon-counting pixel detector', *Optics Express* 21(22), 25677.

Pennicard, D., Lange, S., Smoljanin, S., Becker, J., Hirsemann, H., Epple, M. & Graafsma, H. (2011), 'Development of LAMBDA: Large Area Medipix-Based Detector Array', *Journal of Instrumentation* 6(11), C11009–C11009.

Pfeiffer, F., Bech, M., Bunk, O., Kraft, P., Eikenberry, E. F., Brönnimann, C., Grünzweig, C. & David, C. (2008), 'Hard X-ray dark-field imaging using a grating interferometer', *Nature Materials* 7(2), 134–137.

Pfeiffer, F., Bunk, O., David, C., Bech, M., Le Duc, G., Bravin, A. & Cloetens, P. (2007a), 'High-resolution brain tumor visualization using three-dimensional X-ray phase contrast tomography', *Physics in Medicine and Biology* 52(23), 6923–6930.

Pfeiffer, F., Kottler, C., Bunk, O. & David, C. (2007b), 'Hard X-ray phase tomography with low-brilliance sources', *Physical Review Letters* 98(10), 108105.

Pfeiffer, F., Weitkamp, T., Bunk, O. & David, C. (2006), 'Phase retrieval and differential phase-contrast imaging with low-brilliance X-ray sources', *Nature Physics* 2(4), 258–261.

Pisano, E. D., Johnston, R. E., Chapman, D., Geradts, J., Iacocca, M. V., Livasy, C. A., Washburn, D. B., Sayers, D. E., Zhong, Z., Kiss, M. Z. & Thomlinson, W. C. (2000), 'Human breast cancer specimens: diffraction-enhanced imaging with histologic correlation—improved conspicuity of lesion detail compared with digital radiography', *Radiology* 214(3), 895–901.

Poletti, M. E., Gonçalves, D. & Mazzaro, I. (2002), 'X-ray scattering from human breast tissues and breast-equivalent materials', *Physics in Medicine and Biology* 47(1), 47–63.

Pourmorteza, A., Symons, R., Sandfort, V., Mallek, M., Fuld, M. K., Henderson, G., Jones, E. C., Malayeri, A. A., Folio, L. R. & Bluemke, D. A. (2016), 'Abdominal imaging with contrast-enhanced photon-counting CT: first human experience', *Radiology* 279(1), 239–245.

Prionas, N. D., Lindfors, K. K., Ray, S., Huang, S.-Y., Beckett, L. A., Monsky, W. L. & Boone, J. M. (2010), 'Contrast-enhanced dedicated breast CT: initial clinical experience 1', *Radiology* 256(3), 714–723.

Prokop, M. & Galanski, M. (2003), *Spiral and Multislice Computed Tomography of the Body*, Georg Thieme Verlag, Germany.

Qi, Z., Zambelli, J., Bevins, N. & Chen, G.-H. (2010), 'Quantitative imaging of electron density and effective atomic number using phase contrast CT', *Physics in Medicine and Biology* 55(9), 2669–2677.

Raupach, R. & Flohr, T. (2012), 'Performance evaluation of X-ray differential phase contrast computed tomography (PCT) with respect to medical imaging', *Medical Physics* 39(8), 4761–4774.

Raupach, R. & Flohr, T. G. (2011), 'Analytical evaluation of the signal and noise propagation in X-ray differential phase-contrast computed tomography', *Physics in Medicine and Biology* 56(7), 2219–2244.

Reeder, S. B., Cruite, I., Hamilton, G. & Sirlin, C. B. (2011), 'Quantitative assessment of liver fat with magnetic resonance imaging and spectroscopy', *Journal of Magnetic Resonance Imaging* 34(4), 729–749.

Revol, V., Kottler, C., Kaufmann, R., Straumann, U. & Urban, C. (2010), 'Noise analysis of grating-based X-ray differential phase contrast imaging', *Review of Scientific Instruments* 81(7), 073709.

Rieger, J., Meyer, P., Pelzer, G., Weber, T., Michel, T., Mohr, J. & Anton, G. (2016), 'Designing the phase grating for Talbot-Lau phase-contrast imaging systems: a simulation and experiment study', *Optics Express* 24(12), 13357.

Ruiz-Yaniz, M., Koch, F., Zanette, I., Rack, A., Meyer, P., Kunka, D., Hipp, A., Mohr, J. & Pfeiffer, F. (2015b), 'X-ray grating interferometry at photon energies over 180 keV', *Applied Physics Letters* 106(15), 151105.

Ruiz-Yaniz, M., Zanette, I., Rack, A., Weitkamp, T., Meyer, P., Mohr, J. & Pfeiffer, F. (2015a), 'X-ray refractive-index measurements at photon energies above 100 keV with a grating interferometer', *Physical Review A* 91(3), 033803.

Ryan, E. A., Farquharson, M. J. & Flinton, D. M. (2005), 'The use of Compton scattering to differentiate between classifications of normal and diseased breast tissue', *Physics in Medicine and Biology* 50(14), 3337–3348.

Saam, T., Herzen, J., Hetterich, H., Fill, S., Willner, M., Stockmar, M., Achterhold, K., Zanette, I., Weitkamp, T., Schüller, U., Auweter, S., Adam-Neumair,

S., Nikolaou, K., Reiser, M. F., Pfeiffer, F. & Bamberg, F. (2013), 'Translation of atherosclerotic plaque phase-contrast CT imaging from synchrotron radiation to a conventional lab-based X-ray source', *PLoS ONE* 8(9), e73513.

Sarapata, A., Willner, M., Walter, M., Duttenhofer, T., Kaiser, K., Meyer, P., Braun, C., Fingerle, A., Noël, P. B., Pfeiffer, F. & Herzen, J. (2015), 'Quantitative imaging using high-energy X-ray phase-contrast CT with a 70 kVp polychromatic X-ray spectrum', *Optics Express* 23(1), 523.

Scherer, K., Braig, E., Willer, K., Willner, M., Fingerle, A. A., Chabior, M., Herzen, J., Eiber, M., Haller, B., Straub, M., Schneider, H., Rummeny, E. J., Noël, P. B. & Pfeiffer, F. (2015), 'Non-invasive differentiation of kidney stone types using X-ray dark-field radiography', *Scientific Reports* 5, 9527.

Schleede, S. (2013), *X-ray Phase-Contrast Imaging at a Compact Laser-Driven Synchrotron Source*, Phd thesis, Technische Universität München, Germany.

Schmitzberger, F. F., Fallenberg, E. M., Lawaczeck, R., Hemmendorff, M., Moa, E., Danielsson, M., Bick, U., Diekmann, S., Pöllinger, A., Engelken, F. J. & Diekmann, F. (2011), 'Development of low-dose photon-counting contrast-enhanced tomosynthesis with spectral imaging', *Radiology* 259(2), 558–564.

Schreuder, T. C. M. A., Verwer, B. J., van Nieuwkerk, C. M. J. & Mulder, C. J. J. (2008), 'Nonalcoholic fatty liver disease: an overview of current insights in pathogenesis, diagnosis and treatment', *World Journal of Gastroenterology* 14(16), 2474–2486.

Schulz, G., Weitkamp, T., Zanette, I., Pfeiffer, F., Beckmann, F., David, C., Rutishauser, S., Reznikova, E. & Mueller, B. (2010), 'High-resolution tomographic imaging of a human cerebellum: comparison of absorption and grating-based phase contrast', *Journal of The Royal Society Interface* 7(53), 1665–1676.

Sehgal, C. M., Weinstein, S. P., Arger, P. H. & Conant, E. F. (2006), 'A review of breast ultrasound.', *Journal of Mammary Gland Biology and Neoplasia* 11(2), 113–123.

Shrimpton, P. C. (1981), 'Electron density values of various human tissues: in vitro Compton scatter measurements and calculated ranges', *Physics in Medicine and Biology* 26(5), 907–911.

Silva, J. M. d. S. e., Zanette, I., Noël, P. B., Cardoso, M. B., Kimm, M. A. & Pfeiffer, F. (2015), 'Three-dimensional non-destructive soft-tissue visualization with X-ray staining micro-tomography', *Scientific Reports* 5, 14088.

Skaane, P., Bandos, A. I., Gullien, R., Eben, E. B., Ekseth, U., Haakenaasen, U., Izadi, M., Jebsen, I. N., Jahr, G., Krager, M., Niklason, L. T., Hofvind,

S. & Gur, D. (2013), 'Comparison of digital mammography alone and digital mammography plus tomosynthesis in a population-based screening program', *Radiology* 267(1), 47–56.

Smith, J. A. & Andreopoulou, E. (2004), 'An overview of the status of imaging screening technology for breast cancer', *Annals of Oncology* 15(Supplement 1), I18–I26.

Snigirev, A., Snigireva, I., Kohn, V., Kuznetsov, S. & Schelokov, I. (1995), 'On the possibilities of X-ray phase contrast microimaging by coherent high-energy synchrotron radiation', *Review of Scientific Instruments* 66(12), 5486–5492.

Spiers, F. W. (1946), 'Effective atomic number and energy absorption in tissues', *The British Journal of Radiology* 19(218), 52–63.

Stampanoni, M., Wang, Z., Thuering, T., David, C., Roessl, E., Trippel, M., Kubik-Huch, R. A., Singer, G., Hohl, M. K. & Hauser, N. (2011), 'The first analysis and clinical evaluation of native breast tissue using differential phase-contrast mammography', *Investigative Radiology* 46(12), 801–806.

Stary, H. C. (2000), 'Natural history and histological classification of atherosclerotic lesions: an update', *Arteriosclerosis, Thrombosis, and Vascular Biology* 20(5), 1177–1178.

Suleski, T. J. (1997), 'Generation of Lohmann images from binary-phase Talbot array illuminators', *Applied Optics* 36(20), 4686–4691.

Sztrókay, A., Diemoz, P. C., Schlossbauer, T., Brun, E., Bamberg, F., Mayr, D., Reiser, M. F., Bravin, A. & Coan, P. (2012), 'High-resolution breast tomography at high energy: a feasibility study of phase contrast imaging on a whole breast', *Physics in Medicine and Biology* 57(10), 2931–2942.

Sztrókay, A., Herzen, J., Auweter, S. D., Liebhardt, S., Mayr, D., Willner, M., Hahn, D., Zanette, I., Weitkamp, T., Hellerhoff, K., Pfeiffer, F., Reiser, M. F. & Bamberg, F. (2013), 'Assessment of grating-based X-ray phase-contrast CT for differentiation of invasive ductal carcinoma and ductal carcinoma in situ in an experimental ex vivo set-up', *European Radiology* 23(2), 381–387.

Talbot, H. F. (1836), 'Facts relating to optical science', *Philosophical Magazine and Journal of Science* 9, 401–407.

Tanaka, J., Nagashima, M., Kido, K., Hoshino, Y., Kiyohara, J., Makifuchi, C., Nishino, S., Nagatsuka, S. & Momose, A. (2013), 'Cadaveric and in vivo human joint imaging based on differential phase contrast by X-ray Talbot-Lau interferometry', *Zeitschrift für Medizinische Physik* 23(3), 222–227.

Tanaka, T., Honda, C., Matsuo, S., Noma, K., Oohara, H., Nitta, N., Ota, S., Tsuchiya, K., Sakashita, Y., Yamada, A., Yamasaki, M., Furukawa, A., Takahashi, M. & Murata, K. (2005), 'The first trial of phase contrast imaging for digital full-field mammography using a practical molybdenum X-ray tube', *Investigative Radiology* 40(7), 385–396.

Tapfer, A., Bech, M., Velroyen, A., Meiser, J., Mohr, J., Walter, M., Schulz, J., Pauwels, B., Bruyndonckx, P., Liu, X., Sasov, A. & Pfeiffer, F. (2012), 'Experimental results from a preclinical X-ray phase-contrast CT scanner', *Proceedings of the National Academy of Sciences* 109(39), 15691–15696.

Tapfer, A., Braren, R., Bech, M., Willner, M., Zanette, I., Weitkamp, T., Trajkovic-Arsic, M., Siveke, J. T., Settles, M., Aichler, M., Walch, A. & Pfeiffer, F. (2013), 'X-ray phase-contrast CT of a pancreatic ductal adenocarcinoma mouse model', *PLoS ONE* 8(3), e58439.

Thüring, T. (2013), *Compact X-ray Grating Interferometry for Phase and Dark-Field Computed Tomography in the Diagnostic Energy Range*, Phd thesis, ETH Zurich, Switzerland.

Thüring, T., Abis, M., Wang, Z., David, C. & Stampanoni, M. (2014b), 'X-ray phase-contrast imaging at 100 keV on a conventional source', *Scientific Reports* 4, 5198.

Thüring, T., Barber, W. C., Seo, Y., Alhassen, F., Iwanczyk, J. S. & Stampanoni, M. (2013b), 'Energy resolved X-ray grating interferometry', *Applied Physics Letters* 102(19), 191113.

Thüring, T., Hämmerle, S., Weiss, S., Nüesch, J., Meiser, J., Mohr, J., David, C. & Stampanoni, M. (2013a), Compact hard X-ray grating interferometry for table top phase contrast micro CT, *Proceedings of SPIE* 8668, 866813.

Thüring, T., Modregger, P., Grund, T., Kenntner, J., David, C. & Stampanoni, M. (2011), 'High resolution, large field of view X-ray differential phase contrast imaging on a compact setup', *Applied Physics Letters* 99(4), 041111.

Thüring, T., Modregger, P., Hammerle, S., Weiss, S., Nuesch, J. & Stampanoni, M. (2012), Sensitivity in X-ray grating interferometry on compact systems, *AIP Conference Proceedings* 1466, 293–298.

Thüring, T. & Stampanoni, M. (2014a), 'Performance and optimization of X-ray grating interferometry', *Philosophical Transactions of the Royal Society A: Mathematical, Physical and Engineering Sciences* 372, 20130027–20130027.

Trimborn, B., Meyer, P., Kunka, D., Zuber, M., Albrecht, F., Kreuer, S., Volk, T., Baumbach, T. & Koenig, T. (2016), 'Imaging properties of high aspect

ratio absorption gratings for use in preclinical X-ray grating interferometry', *Physics in Medicine and Biology* 61(2), 527–541.

Tromberg, B. J., Cerussi, A., Shah, N., Compton, M., Durkin, A., Hsiang, D., Butler, J. & Mehta, R. (2005), 'Diffuse optics in breast cancer: detecting tumors in pre-menopausal women and monitoring neoadjuvant chemotherapy', *Breast Cancer Research* 7(6), 279–285.

U-King-Im, J. M., Fox, A. J., Aviv, R. I., Howard, P., Yeung, R., Moody, A. R. & Symons, S. P. (2010), 'Characterization of carotid plaque hemorrhage: a CT angiography and MR intraplaque hemorrhage study', *Stroke* 41(8), 1623–1629.

Vedantham, S. & Karellas, A. (2013), 'X-ray phase contrast imaging of the breast: analysis of tissue simulating materials', *Medical Physics* 40(4), 041906.

Velroyen, A., Yaroshenko, A., Hahn, D., Fehringer, A., Tapfer, A., Müller, M., Noël, P., Pauwels, B., Sasov, A., Yildirim, A., Eickelberg, O., Hellbach, K., Auweter, S., Meinel, F., Reiser, M., Bech, M. & Pfeiffer, F. (2015), 'Grating-based X-ray dark-field computed tomography of living mice', *EBioMedicine* 2(10), 1500–1506.

Weber, T., Bartl, P., Bayer, F., Durst, J., Haas, W., Michel, T., Ritter, A. & Anton, G. (2011), 'Noise in X-ray grating-based phase-contrast imaging', *Medical Physics* 38(7), 4133.

Weber, T., Pelzer, G., Rieger, J., Ritter, A. & Anton, G. (2015), 'Report of improved performance in Talbot-Lau phase-contrast computed tomography', *Medical Physics* 42(6), 2892–2896.

Weitkamp, T., David, C., Kottler, C., Bunk, O. & Pfeiffer, F. (2006), 'Tomography with grating interferometers at low-brilliance sources', *Proceedings of SPIE* 6318, 631828.

Weitkamp, T., Diaz, A., David, C., Pfeiffer, F., Stampanoni, M., Cloetens, P. & Ziegler, E. (2005), 'X-ray phase imaging with a grating interferometer', *Optics Express* 13(16), 6296.

Wen, H., Gomella, A. A., Patel, A., Lynch, S. K., Morgan, N. Y., Anderson, S. A., Bennett, E. E., Xiao, X., Liu, C. & Wolfe, D. E. (2013), 'Subnanoradian X-ray phase-contrast imaging using a far-field interferometer of nanometric phase gratings', *Nature Communications* 4, 2659.

Wilkins, S., Gureyev, T., Gao, D., Pogany, A. & Stevenson, A. (1996), 'Phase-contrast imaging using polychromatic hard X-rays', *Nature* 384(28), 335–384.

Willner, M. (2011), *Development of a System for X-ray Phase Contrast Imaging*, Diploma thesis, Friedrich-Alexander-Universität Erlangen & Technische Universität München, Germany.

Willner, M., Bech, M., Herzen, J., Zanette, I., Hahn, D., Kenntner, J., Mohr, J., Rack, A., Weitkamp, T. & Pfeiffer, F. (2013), 'Quantitative X-ray phase-contrast computed tomography at 82 keV', *Optics Express* 21(4), 4155.

Willner, M., Fior, G., Marschner, M., Birnbacher, L., Schock, J., Braun, C., Fingerle, A. A., Noël, P. B., Rummeny, E. J., Pfeiffer, F. & Herzen, J. (2015), 'Phase-contrast Hounsfield units of fixated and non-fixated soft-tissue samples', *PLoS ONE* 10(8), e0137016.

Willner, M., Herzen, J., Grandl, S., Auweter, S., Mayr, D., Hipp, A., Chabior, M., Sarapata, A., Achterhold, K., Zanette, I., Weitkamp, T., Sztrókay, A., Hellerhoff, K., Reiser, M. & Pfeiffer, F. (2014), 'Quantitative breast tissue characterization using grating-based X-ray phase-contrast imaging', *Physics in Medicine and Biology* 59(7), 1557–1571.

Willner, M., Viermetz, M., Marschner, M., Scherer, K., Braun, C., Fingerle, A., Noël, P., Rummeny, E., Pfeiffer, F. & Herzen, J. (2016), 'Quantitative three-dimensional imaging of lipid, protein, and water contents via X-ray phase-contrast tomography', *PLoS ONE* 11(3), e0151889.

Wintermark, M., Jawadi, S., Rapp, J., Tihan, T., Tong, E., Glidden, D., Abedin, S., Schaeffer, S., Acevedo-Bolton, G., Boudignon, B., Orwoll, B., Pan, X. & Saloner, D. (2008), 'High-resolution CT imaging of carotid artery atherosclerotic plaques', *American Journal of Neuroradiology* 29(5), 875–882.

Woodard, H. Q. & White, D. R. (1986), 'The composition of body tissues', *British Journal of Radiology* 59(708), 1209–1218.

Wynn, T. A. (2008), 'Cellular and molecular mechanisms of fibrosis', *The Journal of Pathology* 214(2), 199–210.

Yaffe, M. J. (2008), 'Mammographic density. Measurement of mammographic density.', *Breast Cancer Research* 10(3), 209.

Yaroshenko, A., Hellbach, K., Bech, M., Grandl, S., Reiser, M. F., Pfeiffer, F. & Meinel, F. G. (2014), 'Grating-based X-ray dark-field imaging: a new paradigm in radiography', *Current Radiology Reports* 2(7), 57.

Yashiro, W., Takeda, Y. & Momose, A. (2008), 'Efficiency of capturing a phase image using cone-beam X-ray Talbot interferometry', *Journal of the Optical Society of America A* 25(8), 2025.

Zanette, I., Weitkamp, T., Lang, S., Langer, M., Mohr, J., David, C. & Baruchel, J. (2011), 'Quantitative phase and absorption tomography with an X-ray grating interferometer and synchrotron radiation', *Physica Status Solidi A* 208(11), 2526–2532.

Zanette, I., Weitkamp, T., Le Duc, G. & Pfeiffer, F. (2013), 'X-ray grating-based phase tomography for 3D histology', *RSC Advances* 3(43), 19816.

Zhao, Y., Brun, E., Coan, P., Huang, Z., Sztrokay, A., Diemoz, P. C., Liebhardt, S., Mittone, A., Gasilov, S., Miao, J. & Bravin, A. (2012), 'High-resolution, low-dose phase contrast X-ray tomography for 3D diagnosis of human breast cancers', *Proceedings of the National Academy of Sciences* 109(45), 18290–18294.

Zhu, P., Zhang, K., Wang, Z., Liu, Y., Liu, X., Wu, Z., McDonald, S. A., Marone, F. & Stampanoni, M. (2010), 'Low-dose, simple, and fast grating-based X-ray phase-contrast imaging', *Proceedings of the National Academy of Sciences* **107**(31), 13576–13581.

List of publications and scientific presentations

First-authored publications (peer-reviewed)

Willner, M., Bech, M., Herzen, J., Zanette, I., Hahn, D., Kenntner, J., Mohr, J., Rack, A., Weitkamp, T. & Pfeiffer, F. (2013), 'Quantitative X-ray phase-contrast computed tomography at 82 keV', *Optics Express* 21(4), 4155.

Willner, M., Herzen, J., Grandl, S., Auweter, S., Mayr, D., Hipp, A., Chabior, M., Sarapata, A., Achterhold, K., Zanette, I., Weitkamp, T., Sztrókay, A., Hellerhoff, K., Reiser, M. & Pfeiffer, F. (2014), 'Quantitative breast tissue characterization using grating-based X-ray phase-contrast imaging', *Physics in Medicine and Biology* 59(7), 1557-1571.

Willner, M., Fior, G., Marschner, M., Birnbacher, L., Schock, J., Braun, C., Fingerle, A., Noël, P., Rummeny, E., Pfeiffer, F. & Herzen, J. (2015), 'Phase-contrast Hounsfield units of fixated and non-fixated soft-tissue samples', *PLoS ONE* 10(8), e0137016.

Willner, M., Viermetz, M., Marschner, M., Scherer, K., Braun, C., Fingerle, A., Noël, P., Rummeny, E., Pfeiffer, F. & Herzen, J. (2016), 'Quantitative three-dimensional imaging of lipid, protein, and water contents via X-ray phase-contrast tomography', *PLoS ONE* 11(3), e0151889.

Co-authored publications (peer-reviewed)

Allner, S., Koehler, T., Fehringer, A., Birnbacher, L., Willner, M., Pfeiffer, F. & Noël, P. (2016), 'Bilateral filtering using the full noise covariance matrix applied to X-ray phase-contrast computed tomography', *Physics in Medicine and Biology* 61(10), 3867-3856.

Auweter, S., Herzen, J., Willner, M., Grandl, S., Scherer, K., Bamberg,

F., Reiser, M., Pfeiffer, F. & Hellerhoff, K. (2014), 'X-ray phase-contrast imaging of the breast – advances towards clinical implementation', *The British Journal of Radiology* 87(1034), 20130606.

Birnbacher, L., Willner, M., Velroyen, A., Marschner, M., Hipp, A., Meiser, J., Koch, F., Schröter, T., Kunka, D., Mohr, J., Pfeiffer, F. & Herzen, J. (2016), 'Experimental realisation of high-sensitivity laboratory X-ray grating-based phase-contrast computed tomography', *Scientific Reports* 6, 24022.

Burger, K., Koehler, T., Chabior, M., Allner, S., Marschner, M., Fehringer, A., Willner, M., Pfeiffer, F. & Noël, P. (2014), 'Regularized iterative integration combined with non-linear diffusion filtering for phase-contrast X-ray computed tomography', *Optics Express* 22(26), 32107.

Esmaeili, M., Floystad, J., Hipp, A., Willner, M., Bech, M., Diaz, A., Royset, A., Andreasen, J., Pfeiffer, F. & Breiby, D. (2015), 'Monitoring moisture distribution in textile materials using grating interferometry and ptychographic X-ray imaging', *Textile Research Journal* 85(1), 80-90.

Fingerle, A., Willner, M., Herzen, J., Münzel, D., Hahn, D., Rummeny, E., Noël, P. & Pfeiffer, F. (2014), 'Simulated cystic renal lesions: quantitative X-ray phase-contrast CT – an in vitro phantom study', *Radiology* 272(3), 739-748.

Fu, J., Biernath, T., Willner, M., Amberger, M., Meiser, J., Kunka, D., Mohr, J., Herzen, J., Bech, M. & Pfeiffer, F. (2014), 'Cone-beam differential phase-contrast laminography with X-ray tube source', *EPL (Europhysics Letters)* 106(6), 68002.

Fu, J., Willner, M., Chen, L., Tan, R., Achterhold, K., Bech, M., Herzen, J., Kunka, D., Mohr, J. & Pfeiffer, F. (2014), 'Helical differential X-ray phase-contrast computed tomography', *Physica Medica* 30(3), 374-379.

Gaass, T., Potdevin, G., Bech, M., Noël, P., Willner, M., Tapfer, A., Pfeiffer, F. & Haase, A. (2013), 'Iterative reconstruction for few-view grating-based phase-contrast CT – an in vitro mouse model', *EPL (Europhysics Letters)* 102(4), 48001.

Grandl, S., Willner, M., Herzen, J., Mayr, D., Auweter, S., Hipp, A., Pfeiffer, F., Reiser, M. & Hellerhoff, K. (2013), 'Evaluation of phase-contrast CT of breast tissue at conventional X-ray sources presentation of selected findings', *Zeitschrift für Medizinische Physik* 23(3), 212-221.

Grandl, S., Willner, M., Herzen, J., Sztrókay-Gaul, A., Mayr, D., Auweter, S.,

Hipp, A., Birnbacher, L., Marschner, M., Chabior, M., Reiser, M., Pfeiffer, F., Bamberg, F. & Hellerhoff, K. (2014), 'Visualizing typical features of breast fibroadenomas using phase-contrast CT: an ex-vivo study', *PLoS ONE* 9(5), e97101.

Gromann, L., Beque, D., Scherer, K., Willer, K., Birnbacher, L., Willner, M., Herzen, J., Grandl, S., Hellerhoff, K., Sperl, J., Pfeiffer, F. & Cozzini, C. (2016), 'Low-dose, phase-contrast mammography with high signal-to-noise ratio', *Biomedical Optics Express* 7(2), 381.

Herzen, J., Willner, M., Fingerle, A., Noël, P., Koehler, T., Drecoll, E., Rummeny, E. & Pfeiffer, F. (2014), 'Imaging liver lesions using grating-based phase-contrast computed tomography with bi-lateral filter postprocessing', *PLoS ONE* 9(1), e83369.

Hetterich, H., Fill, S., Herzen, J., Willner, M., Zanette, I., Weitkamp, T., Rack, A., Schüller, U., Sadeghi, M., Brandl, R., Adam-Neumair, S., Reiser, M., Pfeiffer, F., Bamberg, F. & Saam, T. (2013), 'Grating-based X-ray phase-contrast tomography of atherosclerotic plaque at high photon energies', *Zeitschrift für Medizinische Physik* 23(3), 194203.

Hetterich, H., Webber, N., Willner, M., Herzen, J., Birnbacher, L., Hipp, A., Marschner, M., Auweter, S., Habbel, C., Schüller, U., Bamberg, F., Ertl-Wagner, B., Pfeiffer, F. & Saam, T. (2015), 'AHA classification of coronary and carotid atherosclerotic plaques by grating-based phase-contrast computed tomography', *European Radiology* 26, 3223.

Hetterich, H., Willner, M., Fill, S., Herzen, J., Bamberg, F., Hipp, A., Schüller, U., Adam-Neumair, S., Wirth, S., Reiser, M., Pfeiffer, F. & Saam, T. (2014), 'Phase-contrast CT: qualitative and quantitative evaluation of atherosclerotic carotid artery plaque', *Radiology* 271(3), 870-878.

Hetterich, H., Willner, M., Habbel, C., Herzen, J., Hoffmann, V., Fill, S., Hipp, A., Marschner, M., Schüller, U., Auweter, S., Massberg, S., Reiser, M., Pfeiffer, F., Saam, T. & Bamberg, F. (2015), 'X-ray phase-contrast computed tomography of human coronary arteries', *Investigative Radiology* 50(10), 686-694.

Hipp, A., Willner, M., Herzen, J., Auweter, S., Chabior, M., Meiser, J., Achterhold, K., Mohr, J. & Pfeiffer, F. (2014), 'Energy-resolved visibility analysis of grating interferometers operated at polychromatic X-ray sources', *Optics Express* 22(25), 30394.

Lauridsen, T., Willner, M., Bech, M., Pfeiffer, F. & Feidenhans'l, R. (2015), 'Detection of sub-pixel fractures in X-ray dark-field tomography', *Applied Physics A* 121(3), 1243-1250.

Marschner, M., Willner, M., Potdevin, G., Fehringer, A., Noël, P., Pfeiffer, F. & Herzen, J. (2016), 'Helical X-ray phase-contrast computed tomography without phase stepping', *Scientific Reports* 6, 23953.

Marschner, M., Birnbacher, L., Mechlem, K., Noichl, W., Fehringer, A., Willner, M., Scherer, K., Herzen, J., Noël, P. & Pfeiffer, F. (2016), 'Two-shot X-ray dark-field imaging', *Optics Express* 24(23), 27032.

Meiser, J., Willner, M., Schröter, T., Hofmann, A., Rieger, J., Koch, F., Birnbacher, L., Schüttler, M., Kunka, D., Meyer, P., Faisal, A., Amberger, M., Duttenhofer, T., Weber, T., Hipp, A., Ehn, S., Walter, M., Herzen, J., Schulz, J., Pfeiffer, F. & Mohr, J. (2016), 'Increasing the field of view in grating based X-ray phase contrast imaging using stitched gratings', *Journal of X-Ray Science and Technology* 24(3), 379-388.

Mohajerani, P., Hipp, A., Willner, M., Marschner, M., Trajkovic-Arsic, M., Ma, X., Burton, N., Klemm, U., Radrich, K., Ermolayev, V., Tzoumas, S., Siveke, J., Bech, M., Pfeiffer, F. & Ntziachristos, V. (2014), 'FMT-PCCT: hybrid fluorescence molecular tomography X-ray phase-contrast CT imaging of mouse models', *IEEE Transactions on Medical Imaging* 33(7), 1434-1446.

Noël, P., Herzen, J., Fingerle, A., Willner, M., Stockmar, M., Hahn, D., Settles, M., Drecoll, E., Zanette, I., Weitkamp, T., Rummeny, E. & Pfeiffer, F. (2013), 'Evaluation of the potential of phase-contrast computed tomography for improved visualization of cancerous human liver tissue', *Zeitschrift für Medizinische Physik* 23(3), 204-211.

Pfeiffer, F., Herzen, J., Willner, M., Chabior, M., Auweter, S., Reiser, M. & Bamberg, F. (2013), 'Grating-based X-ray phase contrast for biomedical imaging applications', *Zeitschrift für Medizinische Physik* 23(3), 176-185.

Richter, V., Willner, M., Henningsen, J., Birnbacher, L., Marschner, M., Herzen, J., Kimm, M., Noël, P., Rummeny, J., Pfeiffer, F. & Fingerle, A. (2016), 'Ex vivo characterization of pathologic fluids with quantitative phase-contrast computed tomography', *European Journal of Radiology* 86, 99-104.

Saam, T., Herzen, J., Hetterich, H., Fill, S., Willner, M., Stockmar, M., Achterhold, K., Zanette, I., Weitkamp, T., Schüller, U., Auweter, S., Adam-

Neumair, S., Nikolaou, K., Reiser, M., Pfeiffer, F. & Bamberg, F. (2013), 'Translation of atherosclerotic plaque phase-contrast CT imaging from synchrotron radiation to a conventional lab-based X-ray source', *PLoS ONE* 8(9), e73513.

Sarapata, A., Willner, M., Walter, M., Duttenhofer, T., Kaiser, K., Meyer, P., Braun, C., Fingerle, A., Noël, P., Pfeiffer, F. & Herzen, J. (2015), 'Quantitative imaging using high-energy X-ray phase-contrast CT with a 70 kVp polychromatic X-ray spectrum', *Optics Express* 23(1), 523.

Scherer, K., Braig, E., Willer, K., Willner, M., Fingerle, A., Chabior, M., Herzen, J., Eiber, M., Haller, B., Straub, M., Schneider, H., Rummeny, E., Noël, P. & Pfeiffer, F. (2015), 'Non-invasive differentiation of kidney stone types using X-ray dark-field radiography', *Scientific Reports* 5, 9527.

Sztrókay, A., Herzen, J., Auweter, S., Liebhardt, S., Mayr, D., Willner, M., Hahn, D., Zanette, I., Weitkamp, T., Hellerhoff, K., Pfeiffer, F., Reiser, M. & Bamberg, F. (2013), 'Assessment of grating-based X-ray phase-contrast CT for differentiation of invasive ductal carcinoma and ductal carcinoma in situ in an experimental ex vivo set-up', *European Radiology* 23(2), 381-387.

Tapfer, A., Braren, R., Bech, M., Willner, M., Zanette, I., Weitkamp, T., Trajkovic-Arsic, M., Siveke, J., Settles, M., Aichler, M., Walch, A. & Pfeiffer, F. (2013), 'X-ray phase-contrast CT of a pancreatic ductal adenocarcinoma mouse model', *PLoS ONE* 8(3), e58439.

Thomsen, M., Knudsen, E., Willendrup, P., Bech, M., Willner, M., Pfeiffer, F., Poulsen, M., Lefmann, K. & Feidenhans'l, R. (2015), 'Prediction of beam hardening artefacts in computed tomography using Monte Carlo simulations', *Nuclear Instruments and Methods in Physics Research Section B: Beam Interactions with Materials and Atoms* 342, 314-320.

Oral presentations

Performance optimization of an X-ray grating interferometer for biomedical imaging, *Frühjahrstagung der Deutschen Physikalischen Gesellschaft (DPG)*, Dresden, Germany, March 2011.

Quantitative analysis of human soft tissue using grating-based X-ray phase contrast imaging, *1st GSISH Colloquium on Biomedical Imaging*, Garching, Germany, July 15 2011.

Quantitative grating-based X-ray phase-contrast tomography at 82 keV, *Frühjahrstagung der Deutschen Physikalischen Gesellschaft (DPG)*, Berlin, Germany, March 2012.

Issues concerning the realisation of a human clinical phase-contrast CT scanner, *3rd GSISH Colloquium on Biomedical Imaging*, Garching, Germany, April 2012.

Quantitative phase-contrast imaging at 82 keV, *SPIE Optics and Photonics*, San Diego, USA, August 2012.

Improved differentiation of cystic kidney lesions using quantitative grating-based X-ray phase-contrast CT, *Annual Meeting of the Radiological Society of North America (RSNA)*, Chicago, USA, November 2012.

Quantitative material characterization using grating-based phase-contrast X-ray imaging, *European Congress and Exhibition on Advanced Materials and Processes (EUROMAT)*, Sevilla, Spain, September 2013.

Quantitative tissue characterization using grating-based X-ray phase-contrast imaging, *IEEE Medical Imaging Conference*, Seoul, South Korea, November 2013.

Quantitative tissue characterization using grating-based X-ray phase-contrast imaging, *2nd International Workshop on X-ray and Neutron Phase Imaging with Gratings (XNPIG) and 3rd International Symposium on BioMedical Applications of X-ray Phase Contrast Imaging (IMXP)*, Garmisch-Partenkirchen, Germany, January 2014.

Renal stone assessment with X-ray dark-field radiography, *Annual Meeting of the Radiological Society of North America (RSNA)*, Chicago, USA, November 2014.

Renal stone assessment with X-ray dark-field radiography, *4th International Symposium on BioMedical Applications of X-ray Phase Contrast Imaging (IMXP)*, Garmisch-Partenkirchen, Germany, January 2015.

X-ray imaging on the micro scale, *Workshop on X-ray Imaging Applications in Materials Science*, Garching, Germany, Febuary 2016.

Poster presentations

Quantitative analysis of human soft tissue using grating-based X-ray phase contrast, *Annual Meeting of the American Association of Physicists in Medicine (AAPM)*, Vancouver, Canada, July 2011.

Quantitative characterization of human soft tissue in terms of phase-contrast CT Hounsfield units, *1st International Symposium on BioMedical Applications of X-ray Phase Contrast Imaging (IMXP)*, Garmisch-Partenkirchen, Germany, January 2012.

Quantitative grating-based X-ray phase-contrast tomography at 82 keV, *SPIE Medical Imaging*, San Diego, USA, Febuary 2012.

Quantitative determination of phase Hounsfield units, *1st International Workshop on X-ray and Neutron Phase Imaging with Gratings" (XNPIG)*, Tokio, Japan, March 2012.

Quantitative tissue characterization at laboratory X-ray sources, *2nd International Symposium on BioMedical Applications of X-ray Phase Contrast Imaging (IMXP)*, Garmisch-Partenkirchen, Germany, January 2013.

Quantitative X-ray phase-contrast CT at 82 keV, *Taking X-ray Phase-Contrast Imaging into Mainstream Applications, Scientific Discussion Meeting of the Royal Society*, London, UK, Febuary 2013.

The diagnostic value of phase-contrast breast CT: from synchrotron to conventional X-ray sources, *European Congress of Radiology (ECR)*, Vienna, Austria, March 2013.

Biomedical grating-based phase-contrast imaging using synchrotron and conventional X-ray sources, *Workshop on Industrial CT Scanning*, Garching, Germany, October, 2013.

Diagnostic value of grating-based X-ray phase-contrast imaging, *Annual Meeting of the Radiological Society of North America (RSNA)*, Chicago, USA, December 2013.

Subpixel analysis of lipid, protein and water content using quantitative phase-contrast, *International Conference on X-ray Microscopy (XRM)*, Melbourne, Australia, October 2014.

Quantitative three-dimensional tissue imaging of lipid, protein, and water contents via X-ray phase-contrast tomography, *International Conference on Tomography of Materials and Structures (ICTMS)*, Quebec, Canada, June 2015.

Acknowledgments

It was a long, exciting, and joyful journey until the last words of this thesis have been written. I want to express my deepest appreciation to all those who supported me during this time and contributed to the outcome of this work.

First of all, I want to thank Prof. Franz Pfeiffer for giving me the opportunity to do research on this fascinating topic and for his guidance through the years. I joined his group shortly after he had become professor at the *Technische Universität München* and had the privilege to see how he turned his chair into an internationally renowned research institution for X-ray imaging. By that, I have learned far more than the basic scientific skills from him as I got to know many different aspects of science. I am thankful for the trust, the responsibilities, and the freedom that he gave me for the projects I was working on. At the same time, he supported me in various ways. I could always ask him for advice, he enabled me to visit many interesting conferences, and he provided the financial background for all my activities. Thank you very much!

A large number of people have worked at the chair of Prof. Franz Pfeiffer over the years and many of them contributed to this thesis. They helped me to set up the phase-contrast imaging system, performed measurements, gave me scientific advice, wrote algorithms, kept the IT infrastructure alive, proof-read publications and my thesis, evoked new ideas during fruitful discussions, supported me with the administrative work, created a wonderful working atmosphere, and were great companions on conferences. I want to thank all of them, in particular,

- Martin Bech for sharing all his knowledge and experience in grating-based phase-contrast imaging with me.
- Martin Dierolf for his help with setting up the controlling of the setup and for managing the IT infrastructure.
- Klaus Achterhold for designing the X-ray shielding of the hutch and for all the issues concerning radiation safety.
- Hans Maercz, Walter Gutscher, and Jonathan Schock for their work on the X-ray hutch, the X-ray source, and the cooling device.

- my master students Alexander Hipp and Mathias Marschner who did a great job in optimizing the setup and building a software framework for the complete data handling. They performed numerous of measurements and data analysis. It was always easy and fun working with them and I am happy to see that they continued to do research in the field of phase-contrast imaging.

- my bachelor students Manuel Viermetz, Gabriel Fior, and John Henningsen for their enthusiasm and commitment.

- my successor Lorenz Birnbacher for carrying on with all the projects at the imaging setup. Ohne Dich macht Phasenkontrast einfach keinen Sinn.

- Michael Chabior and Pierre Thibault for their scientific advice.

- Nelly de Leiris for always helping me with travel requests and other administrative things.

- Dieter Renker for the generous and cheerful events at his place.

- my former colleagues Astrid Velroyen, Marco Stockmar, Björn Enders, and Arne Tapfer for the friendship that grew over the time. I enjoyed the time with them in the office, in my free time, and on travels after conferences and I am glad that we are still in touch.

- Michael Epple who became a good friend and the companion of the next episode in my working life. Thank you very much for all your patience until I have finished this thesis!

The great majority of the work presented in this thesis relied on various prosperous interdisciplinary collaborations. I want to thank

- my medical supervisor Alexander Fingerle and Peter Noël from the *Department of Diagnostic and Interventional Radiology* at the *Technische Universität München*. They introduced me to the world of radiology, taught me the art of interdisciplinary research, visited the ethics committee several times, and had many ideas for interesting projects that we then realized together. I further want to thank Prof. Ernst Rummeny, the head of the department, for supporting all our activities and for the delicious steaks in Chicago.

- Sigrid Auweter from the *Department of Clinical Radiology* at the *Ludwig-Maximilians-Universität München* who coordinated the clinical projects within the *Munich-Centre for Advanced Photonics* (MAP). I further want to thank Prof. Maximilian Reiser and Fabian Bamberg for establishing the MAP collaboration at their department.

- the team of MAP plaque at the *Department of Clinical Radiology*, especially Holger Hetterich, Tobias Saam, and Sandra Fill. I really enjoyed our cooperation a lot.

- Susanne Grandl, Anikó Sztrókay-Gaul, and Karin Hellerhoff from the *Department of Clinical Radiology* for their support in the breast imaging project.

- Christian Braun from the *Institute of Forensic Medicine* at the *Ludwig-Maximilians-Universität München* for providing various tissue samples.

- Doris Mayr from the *Institute of Pathology* at the *Ludwig-Maximilians-Universität München* for the verification of tissues and the brief but very interesting glimpse of histopathology that she gave me.

- everyone at the *Karlsruhe Institute of Technology* and *microworks GmbH* who contributed to the manufacturing of the optical gratings, in particular, Johannes Kenntner, Jan Meiser, Jürgen Mohr, and Joachim Schulz. Our phase-contrast imaging system would not have achieved its high performance without your efforts and advances. It was always a pleasure to test and characterize new gratings together.

- Irene Zanette, Timm Weitkamp, Alexander Rack, Felix Beckmann, and Georg Schulz for their help and advice at the synchrotron beamlines *ID19* of the *European Synchrotron Radiation Facility* and *W2 (HARWI II)* of the *Deutsches Elektronen-Synchrotron*. I have learned a lot and had much fun during these intense times.

- Katharina Lang and the other coordinators of the former *Graduate School of Information Science in Health*, now *Graduate School for Bioengineering*, for all the networking events, soft-skill courses, and so on that they organized.

- all the guests at our chair who conducted their studies with us at the phase-contrast imaging system, especially Fu Jian from China and the group of Prof. Robert Feidenhans'l from Denmark.

- all the co-authors of the publications and conference abstracts that arose throughout the time. So far, I have acknowledged only a small number of the people that contributed to the different projects. Many more people, especially at the clinics, were involved by providing samples, doing histopathological workups, performing reader studies, sharing their expertise, etc. I want to thank all of them.

- the scientific community of X-ray phase-contrast imaging and related fields for the interesting and informative presentations and conversations at conferences that I attended.

It is hard for me to find words that can express my deep gratitude to Julia Herzen. She was mentoring my thesis and she extensively discussed all our research projects and ideas with me. She managed the collaborations with our clinical partners and she showed me how to survive at synchrotron radiation facilities. She shared her knowledge in X-ray imaging with me and she helped me to develop my scientific skills. She gave me valuable advice and she spent a lot of time with me networking at conferences. But most important, she enriches my life in so many different ways. Danke, dass es Dich gibt!

Finally, I want to thank my family for their love, for their trust and for always being there for me.